Laser-assisted Fabrication of Specialty Optical Fibers and Applications in Nonlinear Optics, Light Amplification, and Sensing

Inaugural Dissertation
of the Faculty of Science
University of Bern

presented by
Pascal Hänzi

Supervisor of the doctoral thesis:

Prof. Dr. Alexander Heidt
Institute of Applied Physics
of the University of Bern

source: https://doi.org/10.48549/5675 | downloaded: 22.12.2024

Laser-assisted Fabrication of Specialty Optical Fibers and Applications in Nonlinear Optics, Light Amplification, and Sensing

Inaugural Dissertation
of the Faculty of Science
University of Bern

presented by

Pascal Hänzi

Supervisor of the doctoral thesis:

Prof. Dr. Alexander Heidt

Institute of Applied Physics
of the University of Bern

Accepted by the Faculty of Science.

Bern, 26.09.2024

The Dean
Prof. Dr. Jean-Louis Reymond

This work is licensed under CC BY 4.0
https://creativecommons.org/licenses/by/4.0/deed.de

Abstract

The demand for specialty optical fibers is ever growing. Requirements range from engineered dispersion to managed nonlinearity to optimized gain profiles. Conventional chemical vapor deposition (CVD) techniques are optimized for kilometer-scale fiber production and are relatively inflexible and cost ineffective for rapid fiber prototyping. A fast turnover rate from design to product is essential for unique doping compositions, such as high amounts of individual rare earths, a mixture of several, or more temperature sensitive dopants such as nanoparticles.

To overcome these limitations, a novel preform fabrication technique based on CO_2 laser vitrification has been developed. The result is two different approaches to doping silica fibers, powder-in-tube laser vitrification (PLV) and liquid-layer laser vitrification (3LV). The PLV enabled the successful incorporation of nanodiamond particles into silica fibers. Measurements show a highly dispersive nonlinearity, while the chromatic dispersion remains largely unchanged, demonstrating the potential for independent nonlinearity and dispersion engineering. 3LV was found to be effective in producing homogeneously doped rare earth fibers, resulting in highly ytterbium-doped fibers with performance comparable to commercial fibers, validating the capability of the new method to produce high quality doped glass material. Leveraging the flexibility of both methods, multiple rare earth doped fibers were developed that exhibit fluorescence emission over a full octave. In addition, the fabrication of an alumina core fiber with a high rare earth concentration was investigated with the possibility of short amplifiers, high thermal loads, and mid-IR operation in mind. Similar fibers doped with terbium were fabricated and tested for Faraday rotation, useful in magnetic field and current sensing applications.

Finally, noise sources in supercontinuum (SC) generation are investigated, leading to the development of a hybrid dispersion fiber that utilizes anomalous dispersion for initial pulse compression and all-normal dispersion for nonlinear pulse broadening. The generated SC exhibits ultra-low noise while spanning more than a full frequency octave. This approach is easily adaptable and can potentially improve the performance and noise characteristics of other photonic systems such as optical frequency combs (OFCs).

Research output list

The following list contains the published material, resulting from four years of experiments and work during my PhD.

Publications in peer-reviewed journals

- Anupamaa Rampur, Dirk-Mathys Spangenberg, Benoît Sierro, **Pascal Hänzi**, Mariusz Klimczak, and Alexander M. Heidt. "Perspective on the next generation of ultra-low noise fiber supercontinuum sources and their emerging applications in spectroscopy, imaging, and ultrafast photonics". In: *Applied Physics Letters* 118.24 (June 2021), p. 240504. DOI: 10.1063/5.0053436

- Benoît Sierro, **Pascal Hänzi**, Dirk Spangenberg, Anupamaa Rampur, and Alexander M. Heidt. "Reducing the noise of fiber supercontinuum sources to its limits by exploiting cascaded soliton and wave breaking nonlinear dynamics". In: *Optica* 9.4 (Apr. 2022), pp. 352–359. DOI: 10.1364/OPTICA.450505

- **Pascal Hänzi**, Benoît Sierro, Zhixin Liu, Valerio Romano, Anupamaa Rampur, and Alexander M. Heidt. "Benefits of cascaded nonlinear dynamics in hybrid fibers for low-noise supercontinuum generation". In: *Opt. Express* 31.7 (Mar. 2023), pp. 11067–11079. DOI: 10.1364/OE.481970

- Grzegorz Stępniewski, **Pascal Hänzi**, Adam Filipkowski, Monika Janik, Mariusz Mrózek, Yuriy Stepanenko, Robert Bogdanowicz, Valerio Romano, Alexander Heidt, Ryszard Buczyński, and Mariusz Klimczak. "Nonlinearity shaping in nanostructured glass-diamond hybrid materials for optical fiber preforms". In: *Carbon* 215 (Sept. 2023), p. 118465. DOI: 10.1016/j.carbon.2023.118465

- Dunia Blaser, **Pascal Hänzi**, Sönke Pilz, Alexander Heidt, and Valerio Romano. "Multimode Ytterbium–Aluminosilicate Core Optical Fibre for Amplification and Laser Applications". In: *Fibers* 11.11 (Nov. 2023), p. 95. DOI: 10.3390/fib11110095

Conference talk

- **Pascal Hänzi**, Benoît Sierro, Dirk Spangenberg, Anupamaa Rampur, and Alexander M. Heidt. "Low Noise Supercontinuum Using Cascaded Soliton and Wave-Breaking Nonlinear Dynamics". In: *Optica Advanced Photonics Congress 2022*. Optica Publishing Group, 2022, SoW5G.2. DOI: 10.1364/SOF.2022.SoW5G.2

Contributions to conferences

- Dirk-Mathys Spangenberg, Benoît Sierro, Anupamaa Rampur, **Pascal Hänzi**, Alexander Hartung, Pawel Mergo, Karol Tarnowski, Tadeusz Martynkien, Mariusz Klimczak, and Alexander M. Heidt. "Noise Fingerprints of Fiber Supercontinuum Sources". In: *2021 Conference on Lasers and Electro-Optics Europe*

and European Quantum Electronics Conference. Optica Publishing Group, 2021, p. cd.5.3

- **Pascal Hänzi**, Benoît Sierro, Dirk Spangenberg, Anupamaa Rampur, and Alexander M. Heidt. "Low Noise Supercontinuum Using Cascaded Soliton and Wave-Breaking Nonlinear Dynamics". In: *Optica Advanced Photonics Congress 2022*. Optica Publishing Group, 2022, SoW5G.2. DOI: 10.1364/SOF.2022.SoW5G.2

- Grzegorz Stępniewski, **Pascal Hänzi**, Tomasz Kardas, Sara Lukasik, Yuriy Stepanenko, Maciej Głowacki, Valerio Romano, Ryszard Buczyński, Robert Bogdanowicz, Alexander M. Heidt, and Mariusz Klimczak. "Shaping the nonlinear response of silica single-mode fibers with nanodiamonds volumetrically integrated in the core". In: *CLEO/Europe 2023*. Optica Publishing Group. Munich, Germany, June 2023, CE–7.4

- Invited talk **Pascal Hänzi**, Grzegorz Stępniewski, Adam Filipkowski, Sara Lukasik, Tomasz Kardas, Yuriy Stepanenko, Maciej Głowacki, Mariusz Mrózek, Adam Wojciechowski, Valerio Romano, Robert Bogdanowicz, Katarzyna Krupa, Ryszard Buczyński, Alexander M. Heidt, and Mariusz Klimczak. "Fabrication of Nanodiamond-Doped Silica Fiber With Highly Dispersive Nonlinearity". In: *Optica Advanced Photonics Congress 2024*. Optica Publishing Group, 2024, SoM1F.3

Papers in preparation

- **Pascal Hänzi**, Dariusz Pysz, Mariusz Mrózek, Robert Bogdanowicz, Ryszard Buczyński, Mariusz Klimczak, Valerio Romano, Alexander Heidt. "Laser-assisted rapid prototyping of silica optical fibers functionalized with nanodiamonds and multiple active rare earth dopants". (In preparation)

- **Pascal Hänzi**, Grzegorz Stępniewski, Adam Filipkowski, Sara Lukasik, Tomasz Kardas, Yuriy Stepanenko, Maciej Głowacki, Mariusz Mrózek, Adam Wojciechowski, Valerio Romano, Robert Bogdanowicz, Katarzyna Krupa, Ryszard Buczyński, Alexander M. Heidt, Mariusz Klimczak. "Nanodiamond-doped silica fiber with highly dispersive nonlinearity". (In preparation)

List of acronyms

ANDi all-normal dispersion

ASE amplified spontaneous emission

CVD chemical vapor deposition

DW dispersive wave

EDX energy-dispersive x-ray spectroscopy

ESA electronic spectrum analyzer

FUT fiber under test

FWHM full width at half maximum

FWM four-wave mixing

GNLSE generalized nonlinear Schrödinger equation

GVD group velocity dispersion

HNLF highly non-linear fiber

MCVD modified chemical vapor deposition

MFD mode field diameter

MFR mode field radius

MI modulation instability

MPR mixed parametric Raman

NA numerical aperture

ND nano diamond

NLSE non-linear Schrodinger equation

OSA optical spectrum analyzer

OFC optical frequency comb

OWB optical wave braking

OCT optical coherence tomography

PBS polarizing beam splitter

PCF photonic crystal fiber

PER	polarization extinction ratio
PM	polarization-maintaining
PMI	polarization modulation instability
PSD	power spectral density
RE	rare earth
RIN	relative intensity noise
RIP	refractive index profile
RMS	root mean square
SBS	stimulated Brillouin scattering
SC	supercontinuum
SE	stimulated emission
SFG	sum frequency generation
SHG	second harmonic generation
SMF	single mode fiber
SOF	specialty optical fibers
SPM	self-phase modulation
SRS	stimulated Raman scattering
STED	stimulated emission depletion
TDP	time-domain ptychography
TEC	thermally expanding core
TEOS	tetraethyl orthosilicate
TIR	total internal reflection
WDM	wavelength-division multiplexer
XMI	cross-phase modulation instability
XPM	cross-phase modulation
ZDW	zero-dispersion wavelength

Contents

Abstract **i**

Research output list **ii**

List of acronyms **iv**

1 Introduction **1**

2 Theory **7**
2.1 Fundamentals of light propagation in a medium 7
2.1.1 Maxwell's equations and basic definitions 7
2.1.2 Guided light 10
2.1.3 Active media 13
2.1.4 Lasers 15
2.1.4.1 Optical frequency combs 16
2.1.5 Nonlinear effects in fibers 17
2.1.5.1 Nonlinear Schrodinger equation 17
2.1.5.2 Self-phase modulation 19
2.1.5.3 Solitons 19
2.1.5.4 Supercontinuum generation 20
2.2 Optical fiber fabrication methods 20

3 Prototyping of novel optical fibers **25**
3.1 Laser-assisted rapid prototyping of doped silica optical fibers 25
3.1.1 Introduction 25
3.1.2 Laser system and vitrification setup 26
3.1.3 Liquid layer laser vitrification (3LV) 28
3.1.4 Powder-in-tube laser vitrification (PLV) 29
3.1.5 Optimization of process parameters 31
3.2 Realized fiber prototypes 32
3.2.1 Yb-doped aluminosilicate fiber 32
3.2.1.1 Production 33
3.2.1.2 Refractive index and dopant concentration 34
3.2.1.3 Absorption and emission characteristics 35
3.2.1.4 Laser experiment 37
3.2.2 Multi rare rarth doped fiber 38

3.2.3 Nanodiamond doping 40
3.2.3.1 Production 40
3.2.3.2 Preform and fiber characterization 42
3.2.3.3 Effect of nanodiamond doping on fiber nonlinearity . . 43
3.2.3.4 Conclusion of nonlinearity experiments 46
3.3 Other prototyping methods 48
3.3.1 Ytterbium-doped aluminium core fiber by direct powder mixing 48
3.3.1.1 Precursor and fiber fabrication 49
3.3.1.2 Geometry, composition and refractive index 49
3.3.1.3 Fluorescence and spectroscopy 50
3.3.1.4 Laser and amplifier 50
3.3.2 Highly terbium doped fibers 51
3.3.2.1 Drawing methods, composition and attenuation 52
3.3.2.2 Faraday rotation 53
3.3.2.3 Measured Verdet constants 55
3.3.2.4 Effective Verdet constant 56
3.4 Conclusion 58

4 Low noise supercontinuum generation using a hybrid fiber approach 61
4.1 Introduction 62
4.2 Noise fingerprints of highly non-linear fibers and contributing mechanisms 64
4.2.1 Noise control by dispersion engineering 65
4.2.2 Noise control by designing fiber geometry and birefringence . . . 67
4.3 Supercontinuum generation by separating nonlinearities in hybrid fibers 70
4.3.1 Hybrid approach using all-normal dispersion highly nonlinear fiber 71
4.3.1.1 Soliton pre-compression 72
4.3.1.2 Experimental setup and RIN measurement 73
4.3.1.3 Hybrid ANDi fiber 75
4.3.1.4 Reduction of relative intensity noise 76
4.3.1.5 Suppression of polarization modulation instability . . . 79
4.3.1.6 Phase stability 81
4.3.2 Extending the hybrid fiber concept to other dispersion regimes . 84
4.3.2.1 Experiment and highly nonlinear fibers 84
4.3.2.2 Performance in different dispersion regimes 87
4.3.3 Discussion 89
4.3.3.1 Spectral bandwidth and flatness 89
4.3.3.2 Noise properties 91
4.4 Conclusion 92

Acknowledgements 115

Declaration of consent 116

Chapter 1

Introduction

Optical fibers produced from silica glass are ubiquitous. They form the backbone of our information infrastructure and transmit data at close to the speed of light across the globe, which they span multiple of thousands of times. They are also integral components in various areas of applications including machining, environmental sensing, medical surgery, and nonlinear optics [1–5]. Unlike telecommunications, where ultra-low loss is the primary requirement, emerging technologies leverage the unique optical, electrical, acoustic, or optoelectronic capabilities of specialty fibers functionalized with passive or active dopant materials such as rare-earth metals, semiconductors, or nanoparticles [6–9].

As the demand for customized specialty fiber grows, standard production methods face challenges. Chemical vapor deposition (CVD) techniques, commonly used to fabricate preforms for drawing silica fibers, are highly effective for cost-efficient large-scale production of high purity silica [10, 11]. However, in many research environments the focus lies on producing short sections of highly customized multi-component fibers with novel dopants and functionalities.

In such situations, CVD methods are often too restrictive in terms of the glass compositions they allow [12], as the RE concentration achievable is limited. Additionally the running cost and the necessary containment and scrubbing of toxic gas emissions can be prohibitive.

Higher rare earth (RE) concentrations in fibers increase the gain, leading to shorter laser cavities and amplifiers, which can reduce dispersion and nonlinearity [13]. Other applications requiring high doping concentrations are fiber optic magnetic field sensors, which utilize the high Verdet constant of rare earth (RE)s, especially Terbium, to determine the magnetic field strength by Faraday rotation[14].

Unfortunately, simply adding more RE ions without adjusting codopants to the glass leads to concentration quenching and reduces performance. A careful adjustment of the glass composition is necessary [15]. Furthermore, a RE's gain bandwidth is limited by its electronic structure. Combining multiple species in one glass and combining their gain windows would multiply the available gain bandwidth, which could be leveraged in several applications ranging from telecommunications to ultra-short pulse amplification.

Since the minimal width of a laser pulse is essentially given by its spectral band-

width, the gain bandwidth limitation is usually overcome by leveraging self-phase modulation (SPM) or Raman scattering, broadening the spectrum. Multi-dopant fibers with ultrabroad gain bandwidth could reduce the need for nonlinear broadening and lessen the design constraints of short-pulsed systems. Some pulsed systems already benefiting from octave-spanning spectra, such as supercontinuum (SC) lasers and optical frequency comb (OFC) sources could also benefit from improved gain bandwidth, as coherent amplification over the full spectrum would otherwise require the parallel use of different amplifiers and subsequent recombination. The consequences are additional challenges in terms of coherent combination and pulse shape, as amplification over the limited range severely changes the pulse. Tuning the shape of the gain spectrum by changing the RE composition adds another degree of freedom.

However, the interaction between several different RE species is fairly complex, as the coupled rate equations include different absorption and emission lines for each component, not to forget the different energy transfer processes present [16, 17]. Some energy transfers are necessary for the efficient pumping of some RE ions by pump absorption in another species and can be heavily influenced by codopants, such as Al in Er:Yb fibers [18, 19]. This means the whole dynamics are depending on many variables and require careful tuning of the glass composition, which is already the case for much simpler systems. This process often requires numerous trial-and-error runs to optimize composition and vitrification conditions.

Key optical material properties for nonlinear optical phenomena are optical nonlinearity and dispersion. Adjusting these parameters is necessary for efficiently utilizing nonlinear effects like soliton formation or SC generation. Equipped with the brightness of a laser and ultra-broad spectral bandwidths, SC sources based on the nonlinear spectral broadening of high intensity laser pulses in dispersion engineered specialty optical fibers are today an indispensable tool in many scientific and industrial processes [20, 21]. However, for many applications in advanced spectroscopy, microscopy, and ultrafast photonics, the noise of current SC sources has become the predominating factor limiting acquisition speed, sensitivity, or resolution. The noise mechanisms involved in SC generation are predominantly given by fiber dispersion [22].

A fibers nonlinearity and dispersion are typically determined by the utilized glass composition and the fiber geometry. Therefore, they cannot be changed independently, severely limiting the possibilities in optimizing a fibers properties for nonlinear purposes. Nanoparticles, on the other hand, seem to possess highly dispersive optical nonlinearity [23], and are therefore promising candidates for tailoring a fibers nonlinearity independently of dispersion, by doping the glass material.

The high vitrification temperature of silica glass near 2000 °C presents an additional challenge for incorporating novel materials, particularly nanoparticles and 2D materials, as this temperature may compromise their integrity, making post-processing procedures necessary [9, 24, 25]. Although this temperature challenge can be mitigated by using soft glasses with lower melting temperatures [26], silica fibers remain highly desirable due to their robustness, mechanical and chemical stability, and broad transmission window.

Therefore, the following challenges were formulated:

- Active fibers
  - High rare earth concentrations
  - Combination of gain bands from different REs
- Sensing fibers
  - High Verdet constant fiber by maximizing terbium concentration
- Nonlinear fibers
  - Nanodiamond doping
  - Low-noise supercontinuum generation

To address these challenges in producing advanced functionalized silica fibers that meet current and future demands, a range of new preform fabrication and drawing techniques have been developed [24, 27], with laser-assisted manufacturing attracting particular attention [28–30]. While lasers have long been an integral part of fiber production, primarily serving as heat source for fiber drawing and post-processing [31–33], recent advancements have harnessed their unique capabilities for producing specialty optical fiber preforms. The small and localized hot zone, rapid processing speeds, and high cooling rates achievable with CO_2 lasers, for example, create an intriguing regime for glass making. These conditions minimize the time for potentially detrimental thermal interactions, such as diffusion, dissociation, and oxidation [34], and have been linked to the suppression of concentration quenching and ion clustering at high rare-earth doping levels [30].

Moreover, additive manufacturing techniques such as laser powder deposition hold promise for future 3D printing of highly customized preform rods [35]. However, the technology is still in the proof-of-concept stage, limiting the range of investigated material systems and currently resulting in relatively high losses and low efficiency for rare-earth doped active laser fibers [29, 35, 36].

Therefore a novel fiber prototyping scheme was investigated, based on the production of fiber preforms by CO_2 laser vitrification. Two variations are presented in 3.1. The first method is using the liquid doping of silica powder with solutions or dispersions containing the dopants. The powder in the cladding-tube is then rapidly vitrified with the CO_2 laser. The method is called Powder-in-tube laser vitrification (PLV).

PLV enabled the worldwide first demonstration of a silica preform and fiber doped with nanodiamond particles, which is particularly remarkable, as the dissociation temperature of nano diamond (ND) near 600 °C differs significantly from the vitrification temperature of silica near 2000 °C. The linear and nonlinear characteristics of this ND-doped preform and fiber are extensively studied in section 3.2.3, as nanoparticles can exhibit significant nonlinearity dispersion [23], potential reaching negative values. The reversal of the sign of the nonlinearity would greatly increase the dispersion-nonlinearity landscape. Nonlinear effects typically reserved for one dispersion regime would be available in the other, for example normal dispersion solitons. With the

tuning of nonlinearity dispersion, solitonic operation could even be extended over the whole spectrum [37].

The results from z-scan (published in [38]) and pulse propagation experiments confirm strong nonlinearity dispersion. Unfortunately, the negative n_2 regime, remains speculative, as the single-mode cutoff of the produced fiber and the available laser sources complicate experiments at shorter wavelengths. However, our experiments proved the possibility of nonlinearity tuning independent of chromatic dispersion by the doping of fibers with nanodiamond particles.

While the PLV seems suitable for nanoparticles, it proved disadvantageous for the homogeneous doping of silica with rare-earths. Therefore, we adapted the liquid layer deposition of silica tubes with doped sol-gel based on tetraethyl orthosilicate (TEOS) [39] to our laser vitrification method, We called this method liquid-layer-laser vitrification (3LV). It is explained in detail in section 3.1.3. To quantify the achievable glass quality, we developed a relatively highly ytterbium-doped alumina-silicate fiber, benchmarked it against a commercial option, by determining spectroscopic properties of both fibers and tested its performance in a laser setup. The results confirm excellent quality of doped silica preforms and fibers fabricable with 3LV. The methods flexibility was then leveraged to combine ytterbium , erbium and thulium in a single fiber, which is able to produce octave-spanning fluorescence, when pumped accordingly. The level of doping concentration using the 3LV is limited by the solubility of the precursors and the sol-gel chemistry. The method is so far also limited to TEOS based sol-gel, although alumina based sol-gel formation is possible [40].

In that regard a wet powder doping of aluminium oxide with ytterbium was conducted, to produce a rare-earth doped all-alumina core multi-mode fiber, aimed at increasing the possible rare earth concentration. Apart from reducing clustering of RE ions, Al_2O_3 allows transmission in the mid-infrared, is robust and has a high melting point. The achievable Al_2O_3 concentration was ultimately limited to 60 at.% by diffusion of SiO_2 from the cladding. Nonetheless, the fiber was able to produce lasing, showing its potential for mid-IR applications. The fiber is presented in section 3.3.1. This work has also been published in Blaser (2023) [41].

Since these methods proved capable of producing high RE concentration optical fibers, highly terbium-doped fibers were developed for Faraday rotation based fiber-optic magnetic field and current measurements, as terbium has a very high Verdet constant. A variety of different fabrication methods were tested and the Verdet constant of the produced fibers measured. The highest doping concentrations could be produced by wet powder doping of fumed silica. These fibers also showed Verdet constants, that were up to 3× higher than silica, although at the cost of higher losses. Fibers produced by the 3LV method showed lower losses, but were unable to produce any response to the applied magnetic field, possibly due to the limited terbium concentration and noncircular core, causing birefringence and suppressing Faraday rotation. In general, repeatability of the Faraday rotation measurements was low, possibly due to variable fiber intrinsic linear birefringence of arbitrary orientation, combined with bending induced birefringence. These terbium-doped fibers are presented in section 3.3.2.

Section 4 examines and discusses noise mechanisms in supercontinuum generation,

highlighting a significant dependence of noise on the fibers birefringence and dispersion landscape. Since the nonlinearity tuning by nanoparticle doping is in its infancy and specially tailored fibers for SC generation do not yet exist, the properties of two commercially available fibers were combined to produce a hybrid-dispersion fiber. The first fiber section is a standard PM1550 fiber, showing anomalous dispersion. Its length is optimized for the optimal compression of the utilized pulsed laser source. This fiber is spliced directly to a nonlinear ANDi fiber, in which an octave-spanning ultra-low-noise supercontinuum with excellent coherence is generated. The concept is easily adaptable to other systems.

Chapter 2

Theory

2.1 Fundamentals of light propagation in a medium

2.1.1 Maxwell's equations and basic definitions

This section begins with Maxwell's equations and outlines the derivations up to the polarization term, which contains a material response to an applied electromagnetic field, where a Taylor approximation usually divides optics into its linear and nonlinear domains. Following the linear optics derivations, the necessary equations for linear propagation in a fiber, such as numerical aperture, fiber modes, dispersion, etc., are obtained. Maxwell's equations form the pillars of electrodynamics and are necessary to describe the propagation of light in any medium, such as optical fibers. By including higher-order polarization terms in the derivation, nonlinear phenomena such as the Kerr effect and self-phase modulation are described. Finally, stimulated emission, lasing, and light amplification are described, including absorption and emission cross sections, which are essential for the characterization of active fibers.
Maxwell's equations describe the behavior of any electromagnetic field or its components, the electric and magnetic fields $\mathbf{E}, \mathbf{B}$.

$$\epsilon_0 \nabla \cdot \mathbf{E} = \rho - \nabla \cdot \mathbf{B}, \tag{2.1}$$

$$\nabla \cdot \mathbf{B} = 0, \tag{2.2}$$

$$\nabla \times \mathbf{E} = -\frac{\partial \mathbf{B}}{\partial t}, \tag{2.3}$$

$$\nabla \times \mathbf{B} = \mu_0 \mathbf{J} + \mu_0 \epsilon_0, \frac{\partial \mathbf{E}}{\partial t}. \tag{2.4}$$

ϵ_0 is the electric permittivity, μ_0 is the vacuum permeability, ρ is the charge density and $\mathbf{P}$ is the induced electric field in a material, also called polarization. For the case of free space ($\rho = J = P = 0$), one arrives at the wave equations with some reformulations that can be found in any textbook, such as [42]

$$\nabla^2 \mathbf{E} - \mu_0 \epsilon_0 \frac{\partial^2 \mathbf{E}}{\partial t^2} = 0, \tag{2.5}$$

$$\nabla^2 \mathbf{B} - \mu_0 \epsilon_0 \frac{\partial^2 \mathbf{B}}{\partial t^2} = 0. \tag{2.6}$$

General solutions to the wave equation for the electric field are given by two waves propagating in opposite directions

$$\mathbf{E}(\mathbf{r},t) = \mathbf{F}(\mathbf{r}-\mathbf{v}t) + \mathbf{G}(\mathbf{r}+\mathbf{v}t), \tag{2.7}$$

where $|v| = c_0 = 1/\sqrt{\mu_0\epsilon_0}$ is the speed of light. Using Fourier transformations, these solutions can be easily decomposed into sinusoids, which are themselves solutions of the form 2.7 and are called plane waves. In one dimension, these waves can be written in the form

$$E(z,t) = E_0 \sin(kz - \omega t + \delta), \tag{2.8}$$

$$Re(\tilde{E}(z,t)) = Re(\tilde{E}_0 \exp(i(kz - \omega t + \delta))), \tag{2.9}$$

where $kc_0 = \omega$ or $kc_0 = 2\pi f$, k is typically called the wave vector and describes the rate of phase change in the direction of propagation. ω and f are the (angular) frequency and δ is an arbitrary phase shift. The second line is the complex field representation, which is often more convenient to work with. When generalizing to propagation in a homogeneous medium, its response to the electric field, called polarization, must be taken into account. It is useful to expand the polarization into a Taylor series with respect to the electric field

$$P = \epsilon_0(\chi^{(1)}E + \chi^{(2)}E^2 + ...), \tag{2.10}$$

where χ is the electrical susceptibility. Considering the first order gives all of linear optics, while the higher order terms are responsible for nonlinearities. In the linear case, the constants can be combined to give the permittivity $\epsilon = \epsilon_0\epsilon_r = \epsilon_0(1+\chi^{(1)})$, where ϵ_r is the relative permittivity. Assuming no free charges, currents or magnetization, and a slowly varying susceptibility, the inhomogeneous wave equation in one dimension is as follows

$$\frac{\partial^2 E}{\partial z^2} - \mu_0\epsilon_0\frac{\partial^2 E}{\partial t^2} = \mu_0\frac{\partial^2 P}{\partial t^2}. \tag{2.11}$$

Considering the linear regime results in the same homogeneous wave equation as above, but with a modified constant.

$$\frac{\partial^2 E}{\partial z^2} - \mu_0\epsilon\frac{\partial^2 E}{\partial t^2} = 0, \tag{2.12}$$

To quantify this change in more intuitive units, we can introduce the so-called complex index of refraction as

$$n'(\omega) \equiv \sqrt{(1+\chi^{(1)})}. \tag{2.13}$$

In general, n' is complex and can be decomposed into its real and imaginary parts as $n' = n + i\kappa$. n is again called the index of refraction and changes with frequency $f = \omega/(2\pi)$ or wavelength $\lambda = c_0/f$, meaning that different wavelengths travel at different speeds, a phenomenon called dispersion. To illustrate the effect of the imaginary part, consider again a plane wave, where the vacuum wave vector is adjusted to the medium $k' = k_0 n' = k_0(n + i\kappa)$.

$$\tilde{E}(z,t) = E_0 exp(i(k_0 n' z - \omega t + \delta), \tag{2.14}$$

$$= E_0 exp(i((k_0(n+i\kappa)z - \omega t + \delta), \tag{2.15}$$

$$= E_0 exp(i(k_0 n z - \omega t + \delta)) exp(-k_0\kappa z). \tag{2.16}$$

The same plane wave is restored by adding an exponential decay. The absorption coefficient is given by $\alpha = \frac{2\pi}{\lambda}\kappa$.
Since physical waves are not just plane waves and are generally a superposition of them, it is necessary to introduce a more complete description [43]. This is especially true for temporally confined fields, also called pulses. Neglecting the spatial dependence, this looks like

$$\tilde{E}(t) = \sqrt{I(t)}exp(-i\phi(t)). \tag{2.17}$$

$I(t)$ is the intensity, so $\sqrt{I(t)}$ describes the strength of the oscillation and $\phi(t)$ describes the speed of the oscillation. $\phi(t)$ can be expanded to

$$\phi(t) = \phi_0 + \phi_1 t + \frac{1}{2}\phi_2 t^2 + ... \tag{2.18}$$

The first term determines the starting point of the oscillation, since it is a constant. The second term is responsible for the main part of the oscillation around the frequency ω_0. The second term is a quantity called chirp and describes how the frequency of a field changes with time in a linear approximation. This can be seen by looking at the instantaneous frequency for a field with the first three terms

$$\omega_{inst}(t) = \omega_0 - \frac{d\phi}{dt} = \phi_2 t. \tag{2.19}$$

We see that the frequency increases linearly with time. When considering propagation through a medium, it is usually easier to treat the problem in the frequency domain. The field in this domain is given by

$$E(\omega) = \int_{\infty}^{\infty} E(t)exp(-i\omega t)dt. \tag{2.20}$$

The field can again be separated into an envelope and a complex phase term

$$E_f(\omega) = \sqrt{S(\omega)}exp(-i\varphi(\omega)). \tag{2.21}$$

The envelope squared $S(\omega)$ is called the spectrum and is exactly what can be measured with a spectrometer. Since different frequencies travel at different velocities, described by the index of refraction, this simply results in an additional phase term as [44]

$$\varphi(z, \omega) = \varphi(0, \omega) + n(\omega)kz. \tag{2.22}$$

This rate of phase change is also called the propagation constant.

$$\beta(\omega) \equiv n(\omega)k. \tag{2.23}$$

The resulting field in time after the medium is recovered using the inverse Fourier transform. Although the refractive indices of most materials are fairly well known, the propagation constant is often given in the form of a Taylor approximation. The first two terms represent a shift in phase and a shift in time, respectively. The first term corresponds to an overall phase shift. The second term results in a linear spectral phase

and thus a constant time shift in the time domain. It is therefore natural to define the group velocity as

$$\frac{1}{v_g} \equiv \frac{d\beta}{d\omega}. \tag{2.24}$$

The next order term

$$\beta_2 = \frac{d^2\beta}{d\omega^2} \tag{2.25}$$

is called the group velocity dispersion (GVD) and indicates how much different frequencies drift apart as they propagate. For $\beta_2 > 0$, the group velocity decreases with frequency, meaning that lower frequencies travel faster than higher ones. In the visible, most materials behave this way, which is also called normal dispersion. The opposite case is called anomalous dispersion, which typically occurs at lower frequencies. Of course, the GVD has a zero crossing where a pulse is least affected by dispersion. For silica, this is the case at $1310nm$. This quantity is often defined in terms of the wavelength λ. It is called the dispersion parameter. Since the change in group velocity over a frequency interval should be the same over the equivalent wavelength interval, we get $\beta_2 \Delta\omega = D\Delta\lambda$, which results in

$$D \equiv -\frac{2\pi c}{\lambda^2}\beta_2 = \beta_2 \frac{\Delta\omega}{\Delta\lambda}. \tag{2.26}$$

Higher order dispersion becomes relevant when the quadratic phase is minimal or when the spectrum is very broad. In this case, the Taylor expansion becomes cumbersome anyway, and it may be easier to consider the full propagation constant.

2.1.2 Guided light

In the next section, we will consider ways to confine light to a small space and guide it in a desired manner.

One might think that a waveguide could be quickly constructed by coating the inside walls of a hollow channel with a reflective material. The light would then bounce off the walls repeatedly and propagate inside the waveguide. However, the Fresnel coefficients show that there is always some loss in this configuration, which would quickly add up over the length of the guide, and the light would be lost after a short distance. Fortunately, when light is guided inside a material with a higher refractive index than its surroundings, light incident at an interface at a certain angle will be completely reflected back into the higher index region, a situation called total internal reflection (TIR). This is illustrated by Snell's law of refraction

$$n_1 sin(\theta_1) = n_2 sin(\theta_2), \tag{2.27}$$

where n_i and θ_i are the index of refraction and the angle of incidence on each side of the interface. The law describes the angle at which light exits an interface between two different materials. In the TIR configuration it does not give real valued angles and no light passes through the interface. In the case of a fiber, light is initially inserted through another interface at an angle of 90°. The maximum insertion angle at

which TIR occurs can be calculated by geometric arguments and gives the very useful definition of the numerical aperture (NA) for optical fibers

$$NA \equiv \sqrt{n_2^2 - n_1^2} = n_0 sin(\theta_{max}), \tag{2.28}$$

where n_2 is the core and n_1 is the cladding index. n_0 describes the refractive index before the fiber facet and can be ignored when the light propagates through air as $n_{air} \approx 1$. The NA effectively describes the light gathering ability of a fiber and can also be defined for other optical systems.

For the above definition, we have assumed that light behaves like a beam, which results in geometrical optics. However, as the waveguide approaches the scale of the wavelength, the wave properties of the light become increasingly important. To solve the problem of light propagating based on TIR inside a fiber, i.e. a cylindrical structure with a core cylinder having a higher refractive index than its surroundings, we consider the wave equation eq.2.12 again, neglecting any losses and switching to the frequency domain. We get

$$\nabla^2 \tilde{E} - n(\omega)^2 \frac{\omega^2}{c_0^2} \tilde{E} = 0. \tag{2.29}$$

The solutions of this Helmholtz equation are then eigenvectors that do not change shape during translation. This means that these fields will travel down a fiber indefinitely in the absence of absorption. These solutions are found by applying an appropriate coordinate system and implying appropriate boundary conditions, such as continuity of the field across an interface and a vanishing field far from the center of the fiber. In the case of the step-index fiber, changing to cylindrical coordinates radius r, angle ϕ and z, a separation of variables and assuming relatively weak guiding $\Delta n << 1$ leads to linearly polarized modes (LP modes). These modes are distinguished by an amount of angular periodicity and radial oscillations, since they are obtained using the ansatz $E(r, \phi) = F(r) exp(il\phi)$. The radial part is given by Bessel functions of different order m and the parameter l takes integer values. The lowest order Bessel is often approximated by a Gaussian. The guided modes have propagation constants in the range $\omega n_1 < \beta < \omega n_2$. They are usually sorted by β and grouped by their parameters. Typically, the lower order modes are concentrated on the axis and have the highest propagation constant. To estimate the number of modes supported by a step-index fiber, it is convenient to define the normalized frequency or V-number as

$$V \equiv \frac{2\pi}{\lambda} a \sqrt{n_2^2 - n_1^2}. \tag{2.30}$$

It turns out that the second mode is supported for a V-number above 2.405, i.e. for any number below that only one mode, the so-called fundamental mode, is supported. For large V-numbers, the number of supported modes can be estimated as $M^2 = V^2/4$, or twice that if both polarization directions are considered. The following figure shows the supported modes of a fiber in sec. 3.2.1 obtained by numerically solving the Helmholtz equation using the measured refractive index profile (RIP) as input.

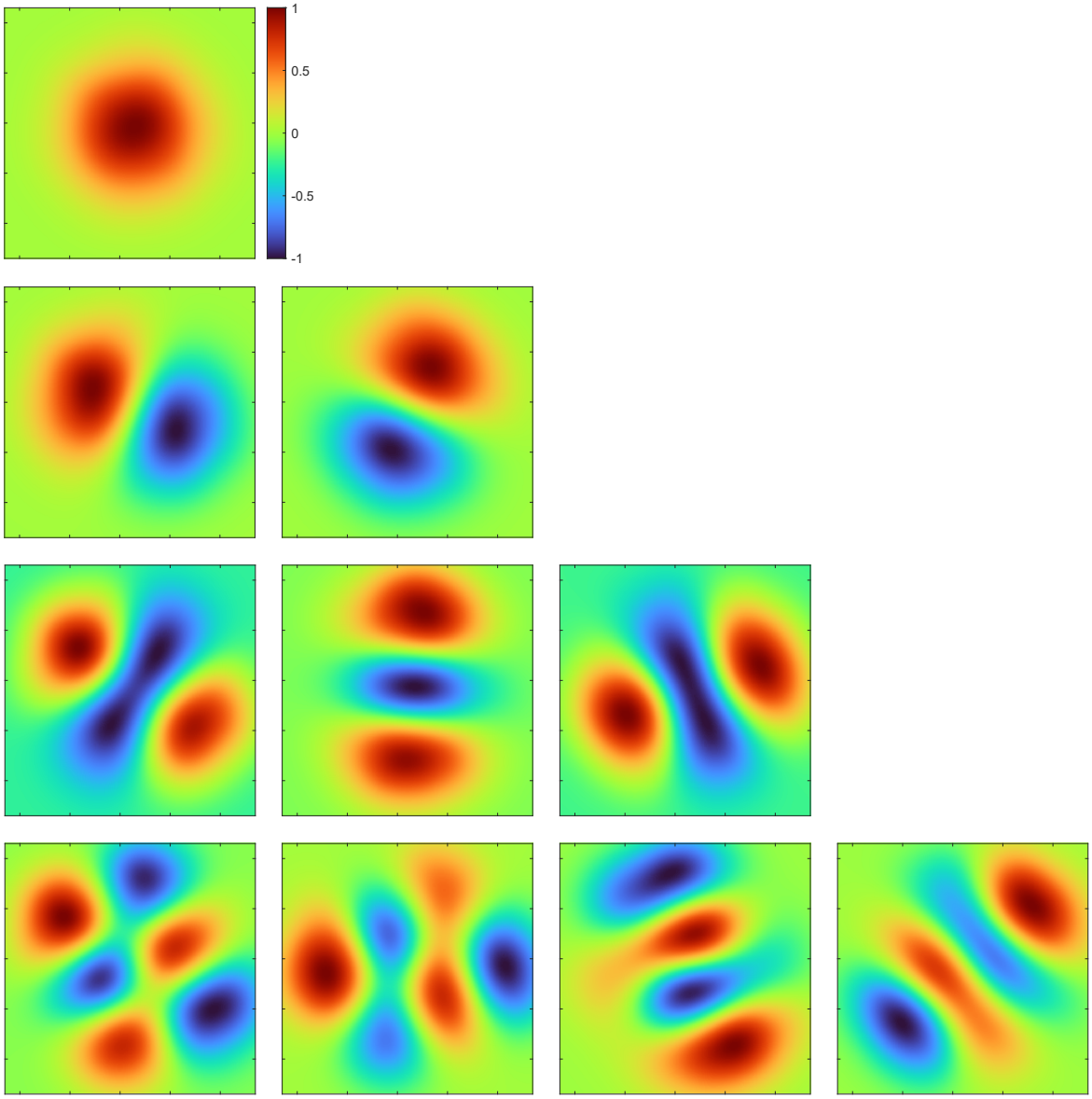

Figure 2.1: The electric fields of the supported modes in the fiber YbDF2 (sec. 3.2.1) at 600 nm, sorted by decreasing group velocity and grouped by complexity. The color map is identical for all plots. Analytical and experimental modes for perfectly circular step-index fibers look considerably different. This fiber has some core ellipticity and a parabolic profile.

Deviations from the step-index profile are beneficial in many applications. It provides additional degrees of freedom when designing fibers for specific purposes. For example, in a multimode fiber used for data transmission, different modes experience different GVDs due to different paths through the fiber. The transmission rate is therefore limited by the modal dispersion. A simple solution is to limit the fiber to single mode guiding, at the expense of the more precise coupling required. However, in a graded refractive index (GRIN) fiber, the index gradually decreases away from the optical axes. The index profile can now be tuned so that the path differences and the effective refractive index largely cancel each other out and the difference in GVD

between modes is minimized. A GRIN profile is typically parameterized as

$$n(r) = \begin{cases} n_1\sqrt{1 - 2\Delta\left(\frac{r}{a}\right)^q} & \text{for } 0 \leq r \leq a \\ n_2 & \text{for } r > a \end{cases} \tag{2.31}$$

where n_1 is the maximum index, n_2 is the cladding index, and Δ is the difference. For $q \to \infty$ this approximates the step index profile. Alternatively, fibers can be designed to specifically negate another fiber's mode dispersion by tuning the parameters of a 'W'-shaped RIP [45] or by optimizing the entire RIP [46]. Other applications of refractive index design include single mode and multimode fibers optimized for top hat beam generation [47, 48], which is advantageous for processing because it reduces the energy in the wings of the beam. In addition, the energy is spread over a larger area, effectively reducing peak intensity and thus nonlinearities. Even square beam shapes have been realized, which prove useful in certain material processing applications [49].

The RIP can also be tailored to transmit optical angular momentum (OAM) light, which often comes in the form of ring-shaped beams[50, 51]. The optimized profiles then take on the donut shape themselves, or result in a GRIN structure.

Typically, the waveguide is realized by changing the glass composition according to the desired RIP. It is also possible to strategically replace some glass with holes. The guiding is then given by a difference in the apparent or effective refractive index [52, 53], eliminating the need for index modifying dopants, thus limiting impurities and scattering, and allowing a very small index step. This has the effect, that single-mode operation is possible over a very broad spectral range, limited only by bend losses within the transparency of silica. Alternatively, the losses of higher order modes can be increased by adjusting the geometry accordingly, or by coupling them into a separate core altogether, where they are rapidly attenuated [54, 55]. The many additional parameters such as hole size, spacing, and arrangement allow shifting the zero dispersion wavelength [56], adjusting the dispersion, or changing the mode field diameter to influence nonlinearities in the fibers [57, 58]. band gap

There are also other control mechanisms that are completely different from TIR. Photonic bandgaps in fibers can be used to confine light, the simplest of which may be the Bragg fiber[59], in which a periodic Bragg reflector-like structure is circularly arranged around a hollow core. These fibers can also have much more sophisticated structures, resulting in complex honeycomb gratings with and without core [60]. The hollow core allows the fibers to be guided through air, greatly reducing dispersion, nonlinearity, and greatly improving damage threshold [61]. It is also possible to introduce liquids into the core [62]. Another guiding mechanism relies on a non-resonant structure that prevents the coupling of light out of the core region [63]. Common to all fiber geometries with holes are the high requirements for pressure stability and tuning during fiber drawing to maintain hole and tube dimensions and structure.

2.1.3 Active media

A material can not only transmit light, it can also subtract or add energy to a field in the form of a photon when the wavelength of the light matches the energy difference

between different energy levels of an electron in a molecule. The electron in this excited state can lose its energy in several ways: it can emit acoustic vibrations (phonons), it can transfer energy to other electrons, or it can emit a photon of random phase and propagation direction. If a photon is already present, it can force the emission of an identical photon of the same energy, phase, and direction. The classical analog would be a forced oscillator assuming the frequency and phase of the external force. These processes are called spontaneous and stimulated emission stimulated emission (SE).

The coherent reproduction of photons by SE is the basis of most lasers and amplifiers. Spontaneous emission can also induce or seed stimulated emission, which is detrimental for laser purposes and is called amplified spontaneous emission (ASE). Nevertheless, pure ASE sources have certain advantages, and high-power and narrow-band systems exist [64]. An ensemble of excited electrons will spontaneously fall back to its ground state at a rate given by the fluorescence lifetime τ or the decay rate $\gamma = 1/\tau$.

$$N_2(t) = N_2(0)e^{-t/\tau}, \tag{2.32}$$

where N_2 is the number of electrons in the excited state. If there are multiple decay paths, the decay rates add up and the lifetime is reduced. The energy differences between levels do not form sharp lines. They are broadened by several mechanisms. First, the states have a natural linewidth given by the energy spread due to the Heisenberg uncertainty.

Second, interactions with lattice phonons add their own contribution, which is strongly temperature dependent. These effects are summarized under the term homogeneous broadening, since they affect each ion equally. Inhomogeneous broadening affects each ion differently. In a lattice, it is the randomly varying local electric field that leads to Stark splitting of sublevels and broadening of the spectral line [65].

The probability of emission or absorption can be given in terms of a cross section. This quantity is given in units of area and indicates how large a fully absorbing or emitting surface would be at the same transition rate. The emission cross section σ_{em} is generally related to the fluorescence lifetime by the Füchtbauer-Ladenburg (FL) relation [66]

$$\frac{1}{\tau} = \frac{8\pi n^2}{c^2} \int f^2 \sigma_{em}(f) df. \tag{2.33}$$

This formula is often used in approximate versions that allow a direct calculation of the emission cross section from the fluorescence line shape and the lifetime [67]. A consequence of the FL relation is

$$g_1 \int f^2 \sigma_{abs} df = g_2 \int f^2 \sigma_{em} df, \tag{2.34}$$

where $g_{1,2}$ are the degeneracies of the lower and upper levels involved, relates σ_{em} to the absorption cross section σ_{abs}, and allows calibration of the peak of one cross section by the other. Alternatively, the McCumber formula provides a more general relationship that allows the calculation of an unknown cross section from a corresponding known cross section. However, the exact energy levels of all states involved must be known [68]. The total rate of photon emission or absorption, called the gain or attenuation

coefficient (depending on the sign), is given by

$$g(z,\lambda) = N_1(z)\sigma_{abs}(\lambda) - N_2(z)\sigma_{em}(\lambda), , \tag{2.35}$$

where $N_{1,2}$ is the number of electrons in each level. If we assume a co-propagating pump of wavelength λ_p to the signal in a fiber of length l, we can replace the population numbers by the absorbed pump power P_a and get the total gain G as

$$G(l,\lambda) = \frac{\phi_p(\sigma_{abs}(\lambda) + \sigma_{em}(\lambda)\tau\lambda_p}{Ahc} - N\sigma_{abs}(\lambda)l, \tag{2.36}$$

where A is the area in which the light is contained, h is Planck's constant, and $N = N_1 + N_2$ [69]. The solution to this problem is usually obtained using the so-called rate equations, which are a set of coupled equations including all the different decay or energy transfer paths, usually including many different energy levels [70]. However, in this simple case, the absorbed pump power P_p along a length of fiber z can be obtained by solving

$$ln\left(\frac{P_p(z)}{P_p(0)}\right) + \frac{P_p(z) - P_p(0)}{P_{sat}} = -N\sigma_{abs}(\lambda_p)z. \tag{2.37}$$

P_{sat} is the power at which the spontaneous emission is half its maximum value in saturation [71]. This fact gives another way to relate the cross sections, as given by

$$P_{sat} = \frac{hcA}{(\sigma_{abs}(\lambda_p) + \sigma_{em}(\lambda_p))\tau\lambda_p\phi_p}. \tag{2.38}$$

ϕ_p describes the quantum efficiency of the pumping process.

2.1.4 Lasers

As we have just seen, it is possible to amplify light using a material with a suitable energy level structure. In fiber lasers, rare earth ions or lanthanides are typically used. They provide a useful energy structure that allows laser applications from the UV to the mid-infrared [72]. When we enclose a gain medium between two reflective surfaces, we form a linear laser cavity. One surface is chosen to be slightly transmissive to allow light to be coupled out. Evaluating the stability of a free-space cavity usually involves a ray-matrix calculation. For fiber lasers, however, this is not necessary because the fiber modes remain largely unchanged during propagation. Longitudinal modes, light traveling back and forth supported by the cavity, require that they have the same phase after a complete round trip. These conditions can be expressed as

$$\frac{2Lnf}{c} = m, \tag{2.39}$$

where m is an integer. This is equivalent to assuming a standing wave in the cavity. The allowed frequencies are given by

$$f_m = m\frac{c}{2Ln}, \tag{2.40}$$

and their frequency spacing is $\delta f = c/(2Ln)$. The modes supported by the laser will be those with sufficient gain. By appropriately designing the cavity, it is possible to achieve single wavelength operation. With multiple supported laser modes, there will naturally be some mode competition and not all modes will be present. In some cases, the cavity will be very susceptible to disturbances that easily change the supported modes.

The power at which the gain exceeds unity is called the threshold power P_{th}. Above this value, the output power is typically a linear function of the pump power until saturation effects occur. In the linear regime, the output power P_{out} is given by

$$P_{out} = a(P_p - P_{th}), \tag{2.41}$$

where a is called the slope efficiency, which basically describes how well additional pump light is converted into laser light [68]. A laser of this type produces a continuous wave (CW) output.

It is also possible to confine the energy into smaller time intervals and form pulses with high peak power, exceeding the CW value by many orders of magnitude. One technique is to switch the cavity losses, called Q-switching. The cavity is pumped, but high losses prevent feedback. When the cavity is switched to a low-loss state, light is built up from SE and all the stored energy is released in the form of laser pulses down to the nanosecond range with powers as high as kilowatts.

To produce shorter pulses with higher peak power, mode locking is required. These pulses are only possible if all modes of the cavity are positively interfering. This can be achieved by using saturable absorbers that reduce their losses at high powers. These saturable absorbers can be realized by using a material intrinsic saturable loss, as in thulium-doped fibers [73] or graphene elements [74]. Artificially, the same effect can be achieved by using intensity dependent nonlinearities, such as a Kerr lens combined with an aperture [75] or the nonlinear polarization rotation in nonlinear optical loop mirrors (NOLM) [76], to name a few.

2.1.4.1 Optical frequency combs

Interestingly, a stable repetition frequency pulse train is essentially a Dirac comb. This function returns another Dirac comb when Fourier transformed. This means that the spectrum will consist of individual narrow spectral comb lines. Deviations from the perfect comb are caused by noise, be it electronic or thermal in nature, or caused by vibrations or intracavity dynamics. Elimination of these noise contributions is critical for efficient use of the individual comb lines. It should be noted, however, that the continuity of the spectrum observed in typical mode-locked lasers is given by the limited resolution of spectrometers. Once the source is sufficiently stabilized, the frequency of each comb line is given by

$$f_m = f_{CEO} + m f_{rep}, \tag{2.42}$$

with m being an integer, f_{rep} being the lasers repetition frequency. f_{CEO} is given by changes in the offset phase between the pulse envelope and the carrier oscillation. Both frequencies must be stabilized, typically using electronically controlled feedback loops with appropriate feedback mechanisms. Stabilization of the repetition rate is achieved

relatively easily by stretching the laser cavity. The f_{CEO} is more difficult to stabilize, since the appropriate feedback mechanisms are more complicated, and determining this frequency as an input to the loop is not easy at all. One solution is to make the comb self-referencing, i.e. the long wavelength part of the pulse is frequency doubled and interferes with the short wavelength side. This requires a spectral bandwidth of more than one octave. The interference creates a beat note at f_{CEO}. Since this frequency is typically in the microwave range, it can be easily measured from the interference using a photodiode. More background and a full description of these sources can be found in Keller (2022) [77].

A continuation of this concept are the dual comb laser sources, where two combs are generated side by side in the same laser cavity. Therefore, they share the same noise and the stabilization of f_{CEO} becomes obsolete if the interference of the two combs is the only interest [78]. This interference is again easily determined in the microwave domain and contains the information of the comb spectra. This makes these sources immensely useful in spectroscopy, atomic clocks or laser ranging [79–81].

2.1.5 Nonlinear effects in fibers

2.1.5.1 Nonlinear Schrodinger equation

As the light intensity increases, a material may react in an increasingly nonlinear fashion, and higher terms of the polarization (eq. 2.10) of the medium become relevant. The following section motivates the non-linear Schrodinger equation (NLSE) as the defining differential equation for nonlinear pulse propagation in fibers. We will follow the derivation in [82] and mention important steps. As a reminder, we rewrite the polarization with the relevant terms

$$P = \epsilon_0(\chi^{(1)}E + \chi^{(2)}E^2 + \chi^{(3)}E^3...) \tag{2.43}$$

In general, $\chi^{(i)}$ is a tensor of rank $j+1$. The first nonlinear term $\chi^{(2)}$ is responsible for second harmonic generation (SHG) and sum frequency generation (SFG). These effects can be interpreted as the combination of two photons into a new photon of combined energy. These processes typically require some sort of phase matching between the wavelengths involved, which is easily achieved in free space using birefringent crystals. In silica fibers, however, this is not feasible. Furthermore, $\chi^{(2)}$ is very weak in silica, as it vanishes in materials with inversion symmetry. $\chi^{(3)}$ leads to nonlinear refraction or the Kerr effect, four-wave mixing, and third-harmonic generation. We will focus on the Kerr effect because it is a very useful mechanism for broadening pulsed light in fibers. By neglecting time-delayed responses of the material (Raman), as well as third-harmonic generation (which would require phase matching), we get

$$P_{NL}(r,t) \approx \epsilon_0\epsilon_{NL}E(r,t), \tag{2.44}$$

$$\epsilon_{NL} = \frac{3}{4}\chi^{(3)}_{xxxx}|E(r,t)|^2. \tag{2.45}$$

eq. 2.45 and treating P_{NL} as a perturbation leads to modified expressions for n and α

$$\tilde{n} = n + n_2|E|^2, \tag{2.46}$$

$$n_2 = \frac{3}{8n} Re(\chi^{(3)}_{xxxx}), \tag{2.47}$$

$$\tilde{\alpha} = \alpha + \alpha_2|E|^2, \tag{2.48}$$

$$\alpha_2 = \frac{3\pi}{2n\lambda} Im(\chi^{(3)}_{xxxx}). \tag{2.49}$$

α_2 is the coefficient for two-photon absorption, which is of little importance in silica. To solve the Helmholtz equation (eq. 2.29) the following approach is chosen

$$\tilde{E}(r, \omega - \omega_0) = F(x, y)\tilde{A}(z, \omega - \omega_0)exp(i\beta_0 z). \tag{2.50}$$

Assuming a slowly varying envelope, two equations are obtained by collecting similar terms

$$\frac{\partial^2 F}{\partial x^2} + \frac{\partial^2 F}{\partial y^2} + \left[\epsilon(\omega)k_0^2 - \tilde{\beta}^2\right] F = 0 \tag{2.51}$$

$$2i\beta_0 \frac{\partial \tilde{A}}{\partial z} + \left(\tilde{\beta}^2 - \beta_0^2\right) \tilde{A} = 0 \tag{2.52}$$

A perturbation treatment with

$$\epsilon \approx n^2 + 2n\Delta n, \tag{2.53}$$

$$\Delta n = n_2|E|^2 + \frac{i\tilde{\alpha}}{2k_0}, \tag{2.54}$$

gives the same fiber modes as discussed in the linear case (see sec. 2.1.2.) with an additional wavenumber term corresponding to the averaged $k_0\Delta n$ integrated over the modal distribution.

$$\Delta\beta = k_0 \frac{\int_{-\infty}^{\infty}\int_{-\infty}^{\infty} \Delta n|F(x,y)|^2\, dx\, dy}{\int_{-\infty}^{\infty}\int_{-\infty}^{\infty} |F(x,y)|^2\, dx\, dy}. \tag{2.55}$$

We can do a Taylor approximation for the wavenumber in eq.2.53 and go back to the time domain. Using $F\{(\omega - \omega_0)^m A(\omega)\} = (i\partial/\partial t)^m A(t)$ and evaluating $\Delta\beta$ with eq.2.55 we get the nonlinear Schrodinger equation

$$\frac{\partial A}{\partial z} + \underbrace{\sum_m i^m \beta_m \frac{\partial^m A}{\partial t^m}}_{dispersion\ terms} + \underbrace{\frac{\alpha}{2} A}_{linear\ loss} = \underbrace{i\gamma|A|^2 A}_{nonlinear\ term}, \tag{2.56}$$

$$\gamma = \frac{n_2\omega_0}{cA_{eff}}. \tag{2.57}$$

A_{eff} is calculated by integration over the mode profile as

$$A_{\text{eff}} = \frac{\left(\int_{-\infty}^{\infty}\int_{-\infty}^{\infty} |F(x,y)|^2\, dx\, dy\right)^2}{\int_{-\infty}^{\infty}\int_{-\infty}^{\infty} |F(x,y)|^4\, dx\, dy}. \tag{2.58}$$

We see that the nonlinearity increases with smaller mode area, a fact that is often used to increase nonlinear effects by reducing the core size of a fiber.

2.1.5.2 Self-phase modulation

Nonlinearities in pulse propagation in a fiber can cause spectral broadening of a laser pulse. This can be illustrated by the case of self-phase modulation. We switch to a comoving time frame

$$T = t - z/v_g, \tag{2.59}$$

and use an approximation

$$A(z,\tau) = \sqrt{P_0}\exp\left(-\frac{\alpha z}{2}\right)U(z,\tau), \tag{2.60}$$

to study the NLSE in the case of low dispersion. The equation reduces to

$$\frac{\partial U}{\partial z} = ie^{-\alpha z}\frac{1}{L_{\mathrm{NL}}}|U|^2 U \tag{2.61}$$

with the nonlinear length defined as

$$L_{NL} = \frac{1}{\gamma P_0}. \tag{2.62}$$

By substituting $U = Vexp(i\phi)$ eq.2.61 is solved as

$$\phi(L,T) = |U(0,T)|^2\frac{L_{eff}}{L_{NL}}, \tag{2.63}$$

$$L_{eff} = \frac{1 - exp(-\alpha L)}{\alpha}. \tag{2.64}$$

The effect on the spectrum becomes clear when evaluating the instantaneous frequency eq. 2.19

$$-\frac{\partial\phi}{\partial T} = -\frac{L_{eff}}{L_{NL}}\frac{\partial}{\partial T}|U(0,T)|^2. \tag{2.65}$$

We see that the instantaneous frequency changes along the pulse according to its shape. Since pulses are limited in time, they have a rising edge first, so there is a red shift in the front. The same argument gives a blue shift in the trailing edge. When combining different laser pulses in a nonlinear fiber, cross-phase modulation (XPM) occurs. They change their phase similar to SPM. Another important consequence of the Kerr effect, especially for anomalous dispersion ($\beta_2 < 0$) and for longer pulses or quasi-CW and CW lasers, is the exponential amplification of field disturbances. This source of noise is called modulation instability (MI).

2.1.5.3 Solitons

Under anomalous dispersion, the NLSE gives rise to stable solutions called solitons. They can be interpreted as an effect of SPM and dispersion balancing each other. Interestingly, the same soliton behavior can be observed as a dip in a CW background (dark solitons). The fundamental soliton is defined by the soliton number N.

$$N^2 = \frac{L_D}{L_{NL}} = \frac{\gamma P_0 T_0^2}{|\beta_2|} = 1, \tag{2.66}$$

with $L_D = T_0^2/|\beta_2|$. The fundamental soliton for given fiber parameters is defined only by its amplitude η and is given by

$$u(z', \tau) = \eta sech(\eta\tau) exp\left(i\frac{\eta^2 z'}{2}\right). \tag{2.67}$$

z' and τ are the coordinates defined by

$$z' = \frac{z}{L_D}, \tag{2.68}$$

$$\tau = \frac{t - \beta_1 z}{T_0}. \tag{2.69}$$

We see that its width is given by the inverse of the amplitude. This is significant because a soliton spreads out as it loses energy to absorption. There are also higher order solitons for integer values of N. These pulses oscillate between states of positive chirp and high peak power. During soliton formation, excess energy is emitted as a dispersive wave, which can cause interference with the soliton.

2.1.5.4 Supercontinuum generation

The use of nonlinear effects to broaden the spectrum of a pulse leads to spectral bandwidths that greatly exceed the limit otherwise given by amplifying materials, sometimes exceeding several octaves [83]. The broader spectrum is useful in several ways. The increased bandwidth supports temporally much shorter pulses than the initial pulse. When SPM is the main nonlinearity, it can produce almost purely linearly chirped broadened pulses. These pulses are then easily compressed using materials with compensating dispersion and the right length or an external pulse compressor [84]. When the pulse spectrum is considered broad, the source is commonly called a supercontinuum. This large spectral expansion is necessary for many applications, such as the self-referencing of frequency combs. Efficient supercontinuum generation requires specially designed fibers. These typically have adapted glass materials and smaller cores for higher field intensities. A comprehensive treatment is given later in this text in chapter 4.

2.2 Optical fiber fabrication methods

The typical path to an optical fiber consists of a two-step process in which a macroscopic version of the fiber is created, with the various regions such as the core and cladding already shaped and made of the correct materials. The preform is then reduced to the desired fiber size by the drawing step. A standard drawing tower is shown in fig. 2.2.

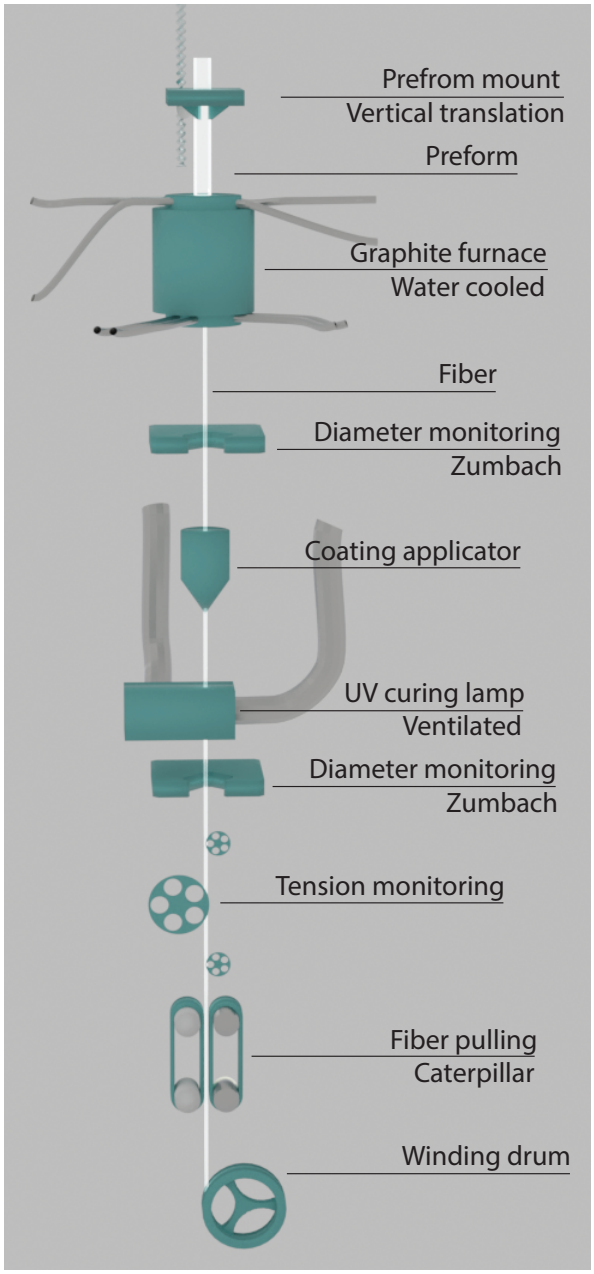

Figure 2.2: Drawing tower in operation at the Swiss Innovation Park in Biel

A drop is formed by heating the bottom of a preform with a suitable heat source (graphite resistance furnace, induction furnace) hot enough to soften or melt all the different glass compositions present. Alternatives such as CO and CO_2 lasers have also been used [31, 33]. The droplet falls under its own weight or is pulled down. On its way down, the droplet is cut off and the attached tail is passed through the various stations necessary for a successful drawing process, such as a laser diameter monitor, a coating applicator, and a UV curing oven to apply an often necessary additional layer to the fiber for protection and optical properties. In addition, a strain gauge can monitor the forces involved in drawing the fiber, and a second diameter measurement stage is essential for accurate control of the fiber geometry. The fiber is then placed in

an adjustable fiber pulling mechanism and finally wound onto a rotating drum.

By adjusting the balance between the rate at which the preform is fed into the furnace and the rate at which the fiber is drawn into the bottom, one can control the resulting fiber thickness, the time the fiber is exposed to the hot zone of the furnace, and the rate at which it is exposed to the cooler outside air.

Leaving glass fibers uncoated and exposed can result in crack propagation due to surface defects, which can be accelerated by simple mechanical stress or by atmospheric moisture and other contaminants absorbed into the glass, causing stress and corrosion[85]. This can be easily observed in an exposed fiber left in a coil as it will likely break into multiple pieces over time. However, choosing the right coating is critical to achieving the desired optical behavior, as a high index coating will cause all light in the cladding to be emitted, while a low index coating will allow light to be guided in the cladding.

An alternative to the standard fiber drawing method is the double-crucible technique [86, 87], in which the cladding and core materials are melted separately and forced through a nozzle that places the cladding material around the core material. By adding multiple core crucibles, it is even possible to draw entire fiber bundles at once [88].

Certain optical materials, such as plastics or soft glasses such as tellurite [89, 90], can be extruded directly through custom dies with some heating to form even complex microstructured optical fiber preforms. In the case of polymer-based optical fibers, they have even been extruded directly to fiber size, skipping the preform [91, 92]. Although plastic optical fibers have a wide range of applications, their use is severely limited by high attenuation and low optical damage threshold [93].

Telecom fibers typically require very high purity and very low losses, which can be as low as $0.14\,\mathrm{dB\,km^{-1}}$ at $1550\,\mathrm{nm}$ [94]. The best methods in this regard are based on some form of vapor deposition, as it is inherently contamination free. Most variations of vapor deposition pass precursors in vapor form such as $SiCl_4$ and O_2 and dopants in the form of $GeCl_4$ or BCl_3 through a glass capillary. These gases are converted to their oxide forms using either a torch or a microwave cavity plasma. These oxides deposit on the heated walls as thin layers or aggregate in the air to form soot [95–99]. Other dopants, including active rare earth ions such as erbium, ytterbium, etc., can be incorporated either in the gas phase in the same process [100], as precursors can generate some vapor pressure when heated, or by soaking the very porous carbon in a solution containing the dissolved precursors. This process is followed by drying and sintering of the soaked layer [101–103].

The main advantage of solution doping is the ability to achieve higher doping concentrations compared to vapor deposition at the cost of purity. Because these vapor deposition techniques rely heavily on gaseous forms of chlorine-containing molecules and even use chlorine gas for drying and purification, they place high demands on safety and air filtration systems.

An elegant way to fabricate arbitrary fiber geometries, RIPs, and dopant distributions is the stack-and-draw technique for microstructured optics. Fiber preforms are created by strategically arranging glass rods, primarily soft glass, of different compositions. This process has to be done manually. By downscaling the drawing process, the

rods are reduced to subwavelength size so that the propagating light experiences an effective glass composition, i.e., smooth. In addition, the glass rods are mixed to some degree due to diffusion during fiber drawing. This approach requires careful planning of rod placement with simulation and calibration [104, 105]. Stacking of glass rods and tubes is also used in the preparation of preforms for photonic crystal fiber (PCF)s, where precise alignment of the glass elements is critical [106].

Alternatively, the structure can be machined into a glass rod [107]. 3D printing like techniques also exist for plastic [108] and soft glass fiber preforms. The high melting point of silica poses a challenge for extrusion of heated material through a nozzle, so a laser powder deposition technique has recently been established that allows preform production within a few hours [29, 30, 36]. An overview of different additive processes with different optical materials can be found in [109].

One approach suitable for drawing powder mixtures in tubes is the molten core technique. It is based on a melting temperature of the core that is lower than the temperature required to draw the sheath. Fibers with high aluminium content and inscribed Bragg gratings for high-temperature applications have been developed [110]. The molten phase of the core also allows the growth of crystals, semiconductors such as silicon. In this case, silicon carbide is added to the silicon in the core, which reacts with oxygen released from the silica cladding during drawing [111]. A review of molten core fibers can be found in [110].

Other fiber fabrication techniques include the powder-in-tube technique or sol-gel based glasses. These methods have been adapted in recent years at the University of Bern and the BFH in the form of sol-gel based granulated oxide powders that have been drawn into fibers directly from the powder, or with prior flame vitrification [112–114].

In this paper we will present our own version of the sol-gel based fiber fabrication process, where we coat the inside of a capillary with the sol-gel and vitrify it directly under an oxygen atmosphere using a CO_2 laser. More about this method in the next chapter 3.1.

Chapter 3

Prototyping of novel optical fibers

3.1 Laser-assisted rapid prototyping of doped silica optical fibers

The following section is based on two papers in preparation for publication:

Pascal Hänzi, Dariusz Pysz, Mariusz Mrózek, Robert Bogdanowicz, Ryszard Buczyński, Mariusz Klimczak, Valerio Romano, Alexander Heidt. "Laser-assisted rapid prototyping of silica optical fibers functionalized with nanodiamonds and multiple active rare earth dopants".

Pascal Hänzi, Grzegorz Stępniewski, Adam Filipkowski, Sara Lukasik, Tomasz Kardas, Yuriy Stepanenko, Maciej Głowacki, Mariusz Mrózek, Adam Wojciechowski, Valerio Romano, Robert Bogdanowicz, Katarzyna Krupa, Ryszard Buczyński, Alexander M. Heidt, Mariusz Klimczak. "Nanodiamond-doped silica fiber with highly dispersive nonlinearity".

3.1.1 Introduction

This work explores the rapid prototyping of functionalized silica fiber preforms by combining the unique advantages of laser-assisted fabrication with variations of the established powder-in-tube and sol-gel dip-coating processes. These preform fabrication techniques have been implemented in various forms [39, 115–118] and are recognized as cost-effective and straightforward methods for obtaining silica glasses doped with a wide range of functional ingredients at high concentrations and uniformity [114, 119–121].

Here, their implementation using laser-assisted preform fabrication is discussed in detail (section 3.1), and the production of high quality silica fibers with three different functionalizations is described (section 3.2). This manuscript reports the achievement of several important milestones:

(i) high glass quality, exemplified by an Ytterbium – doped active laser fiber with emission characteristics comparable to commercial fibers produced by CVD/solution doping techniques;
(ii) high flexibility, demonstrated by the fabrication of fibers with fluorescence bandwidths exceeding one octave doped with multiple active rare earth ions;
(iii) new functionalities, as demonstrated by the first successful direct doping of silica fibers with highly temperature-sensitive nitrogen-vacancy (NV) fluorescent nanodiamonds with dissociation temperatures near 600°C. These studies demonstrate that laser-assisted preform fabrication is a promising route for rapid prototyping of high quality fibers with novel core compositions. In particular, these methods enable the direct doping of silica fibers with temperature-sensitive nanomaterials, a feat not previously achieved with other fabrication technologies.

Our work shows a strong influence of these particles on the optical nonlinearities. Therefore, nanodiamond doped preform slices were fabricated and their n_2 values were determined using a Z-scan setup, showing a significant reduction of n_2 at 1030 nm. The complete work on the preform is published in Stepniewski (2023) [38]. The resulting fiber was studied and its nonlinearity evaluated using nonlinear pulse propagation at different wavelengths and comparing the measured spectra with simulations. The results show a strong nonlinearity dispersion with an increase of n_2 around 1550 nm and a decrease at 1050 nm compared to a pure silica core single mode fiber.

3.1.2 Laser system and vitrification setup

The setup is for the laser vitrification experiments is sketched in fig. 3.1 (a). A multi-kW continuous wave CO_2 laser system is used, although only a fraction of its power is required for preform fabrication. The laser emits a circular flat-top beam with a diameter of approximately 20 mm. Beam shaping techniques are used to adjust the dimensions and shape of the hot zone. Since we have plenty of laser power available, we transform the originally circular laser beam into a nearly rectangular shape by simply passing it through an aperture. This results in a hot zone with a sharp vertical transition between heated and unheated areas, measuring approximately 9 mm in height and 20 mm in width. Further shaping of the hot zone can be easily achieved by using different apertures and lenses as needed.

Since we typically use silica tubes with an outer diameter of 5 mm or less to make our preforms, a significant portion of the laser beam will pass around the tube. To capture this light and ensure uniform heat distribution across the cross section of the tube, we use a retroreflecting cylindrical mirror that redirects the light to the back of the tube. Thicker preforms could be produced by splitting the laser beam into several equal parts and directing them at the tube from different directions [33].

Simulations of the laser heating of the preform show a relatively homogeneous temperature distribution in the x-y plane, considering that the preform is illuminated from only two sides. The simulations show a static picture of the process, so axial rotation is neglected. The actual temperature distribution with rotation will show more rotational symmetry and thus a smoother temperature distribution. Looking at the edges of the heated zone, as in the x-z plane (fig. 3.1 (c) and (d)), we see a localization

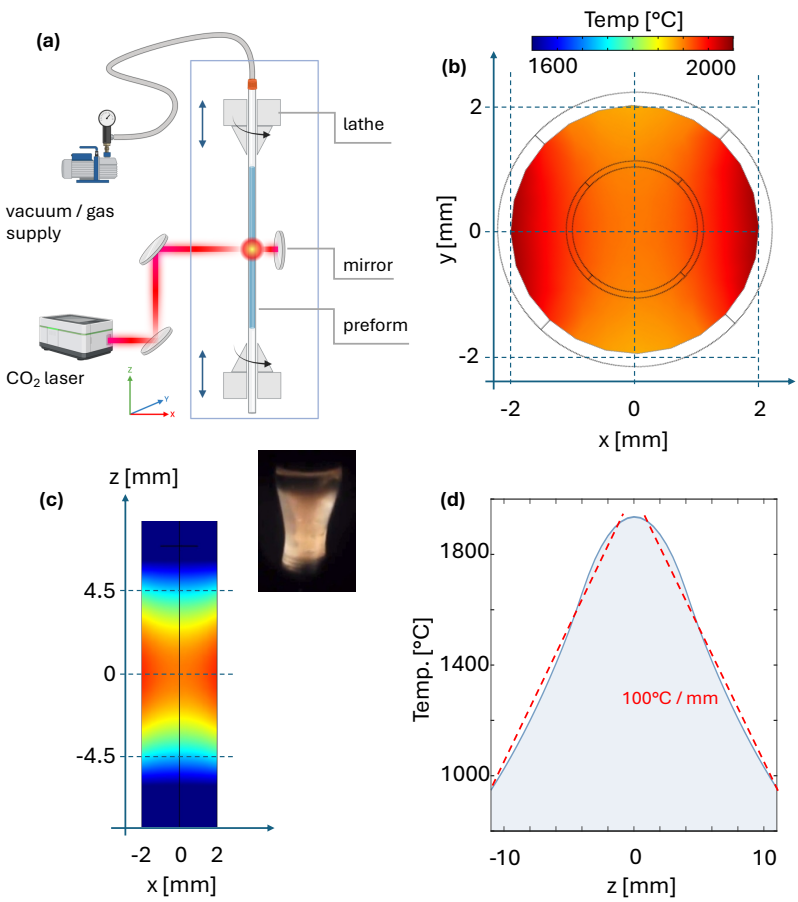

Figure 3.1: (a) Schematic of the laser-assisted vitrification setup. (b)-(d) Simulated temperature distribution in a 4 mm pure silica preform under bidirectional CO_2 laser irradiation along the x-axis. The maximum surface temperature is set to 2000 °C, preform rotation is not considered. (b) Horizontal cross section at $z = 0$. (c) Vertical cross section at $y = 0$. The inset shows a photograph of the hot zone observed in the experiments. (d) Vertical temperature distribution at the preform core ($x = y = 0$). A temperature gradient of 100 °C mm^{-1} is indicated by the red dashed lines.

of the temperature in the middle with a strong gradient of 100 °C mm^{-1}, which means that the heating is strongly confined to a few millimeters. Localized treatment of the material can be achieved and process parameters can be quickly adjusted without the need to re-establish temperature equilibrium, as a region of the preform is quickly moved through the short heating zone.

A custom-built, computer-controlled vitrification lathe is used to rotate and translate the silica tube vertically along the beam. Critical vitrification parameters such as laser power, rotation speed, and translation speed are carefully controlled depending on the preform fabrication method and doping materials used. Gas flow or vacuum can be applied to the preform tube as required. The lathe can produce preforms up to 23 cm in length. The preforms are then drawn into fibers using a standard drawing tower, resulting in fiber lengths of several hundred meters for a 4 mm diameter preform drawn

into a 125 µm diameter fiber. This length is sufficient for research and development of new fiber compositions and functionalities.

3.1.3 Liquid layer laser vitrification (3LV)

3LV is a variation of the sol-gel dip-coating process [115], and it is found to be particularly useful for rapid prototyping of high-quality rare-earth doped fiber preforms for laser and amplifier applications. The basic concept of preform fabrication using 3LV is illustrated in fig. 3.2.

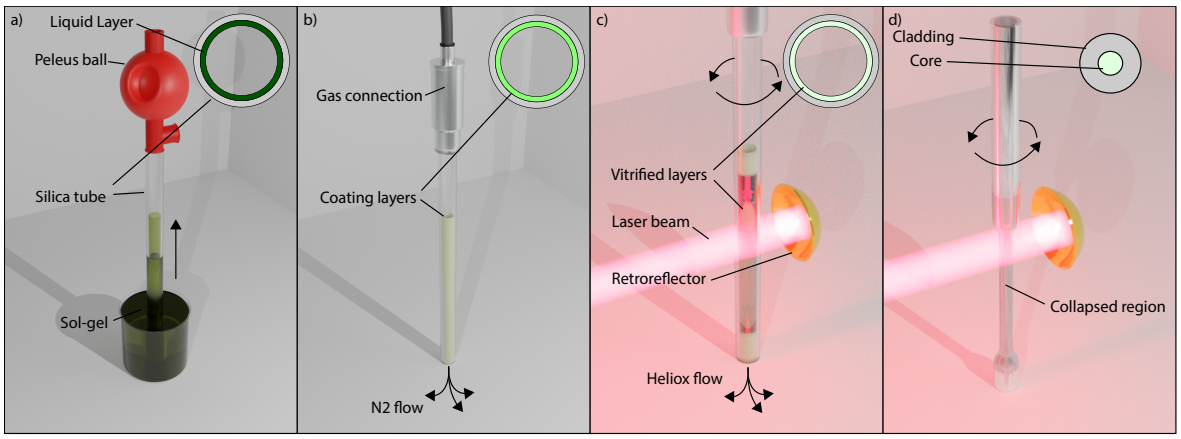

Figure 3.2: Schematic of the 3LV process for the production of doped silica fiber preforms. a) Internal dip coating of a silica glass tube with a thin sol layer containing the dopant precursors. b) Drying under nitrogen atmosphere. c) Laser vitrification of individual layers with Heliox flow. d) Collapse of the silica glass tube. The insets show the cross section of the preform at each step.

The doped silica core material is formed by sequential deposition and CO_2 laser vitrification of multiple thin sol layers inside a fused silica tube. After collapsing the tube, the vitrified layers form the core of the preform, while the fused silica tube serves as the cladding. This entire process, including layer deposition, vitrification, and preform collapse, can be performed in the laser vitrification machine described in section 3.1.2 without the need to move the preform between steps.

The sol is prepared by mixing tetraethyl orthosilicate (TEOS) with an ethanol solution of dopants in chloride form at room temperature. A wide variety of functional dopants can be incorporated into the core at high concentrations while maintaining uniformity at the molecular level. Doping with an ethanol suspension of nanoparticles is also possible. The viscosity of the sol, and thus the thickness of each deposited layer, is adjusted by adding a small amount of distilled water and a few drops of hydrochloric acid. The mixture is stirred overnight to ensure uniform dispersion of the SiO_2 precursors and dopants in the liquid phase, resulting in the growth of a homogeneously doped sol-gel matrix.

While the exact process parameters depend on the individual thermodynamic properties of the dopant materials, we provide details on the fabrication of rare earth doped fiber preforms discussed in sections 3.2.1 and 3.2.2 as a representative example.

A thin layer of the sol is applied to the inner surface of a fused silica tube (4 mm mm outer diameter, 1 mm mm wall thickness) by creating a weak vacuum to draw the liquid into the tube and then rapidly releasing it, repeating this process twice. The layer is dried for 10 minutes under a steady flow of nitrogen (0.3 L/min) to form a xerogel on the inner wall of the tube. Each layer is then vitrified by setting the CO_2 laser power to 600 W (measured before the beam shaping aperture) while the lathe rotates and translates the tube vertically along the beam at a rate of 12 rpm and 3.6 cm/min, respectively. As a result, each section of the preform is exposed to the hot zone for only 15 seconds and then rapidly cooled. This speed contributes to the formation of high-quality, crack-free, transparent glass and allows for the incorporation of temperature-sensitive materials into the fused silica matrix.

A heliox flow (0.5 L/min) provides oxygen for calcination and removal of organic impurities during vitrification, while exhausting the resulting fumes. The thickness of each layer can be controlled by the viscosity of the sol and is typically on the order of a few microns. This value is thin enough to ensure crack-free layer deposition, effective impurity removal, and gas escape during the vitrification process due to the high surface to volume ratio, yet thick enough to minimize the number of layers required to build the core material. Based on our experience and depending on the sol viscosity, 1-3 layers are sufficient to build up enough core material for a single mode fiber core. Since each layer takes only 25 minutes to apply, the entire preform can be fabricated within a few hours.

Finally, the tube is collapsed by reducing the laser power to 500 W and using a slower translation speed of 1.44 cm/min and 40 rpm, without applying gas flow or vacuum. This step is very sensitive to pressure differences, which can cause deformations in the preform. Therefore, it is best to leave both ends of the tube open to achieve symmetrical collapse. The resulting fiber can be drawn directly from the preform without the need for additional cladding tubes.

3.1.4 Powder-in-tube laser vitrification (PLV)

PLV is derived from the powder-in-tube process, which has been explored in various forms to exploit its advantages, such as the ability to fabricate arbitrary shapes and to produce thick preforms with high dopant uniformity, capabilities that are difficult to achieve with chemical vapor deposition (CVD) methods.

Here, the method is easily adapted for rapid prototyping of fiber preforms using laser vitrification. The PLV process is found to be particularly useful for the integration of nanoparticles into a pure silica fiber core. Section 3.2.3 discusses the fabrication of a nanodiamond-doped silica fiber as an example. While it is also possible to incorporate active rare earth elements using this method, as demonstrated with a multidoped fiber in section 3.2.2, we observed a strong tendency for microbubble formation during vitrification, clustering, and inhomogeneous doping distributions, resulting in high scattering losses and unsatisfactory glass quality.

Based on our experience, the 3LV process is more suitable for producing high quality, bubble-free preforms doped with active rare earth elements. Unlike the 3LV process, which involves the sequential vitrification of multiple thin layers, the PLV approach is

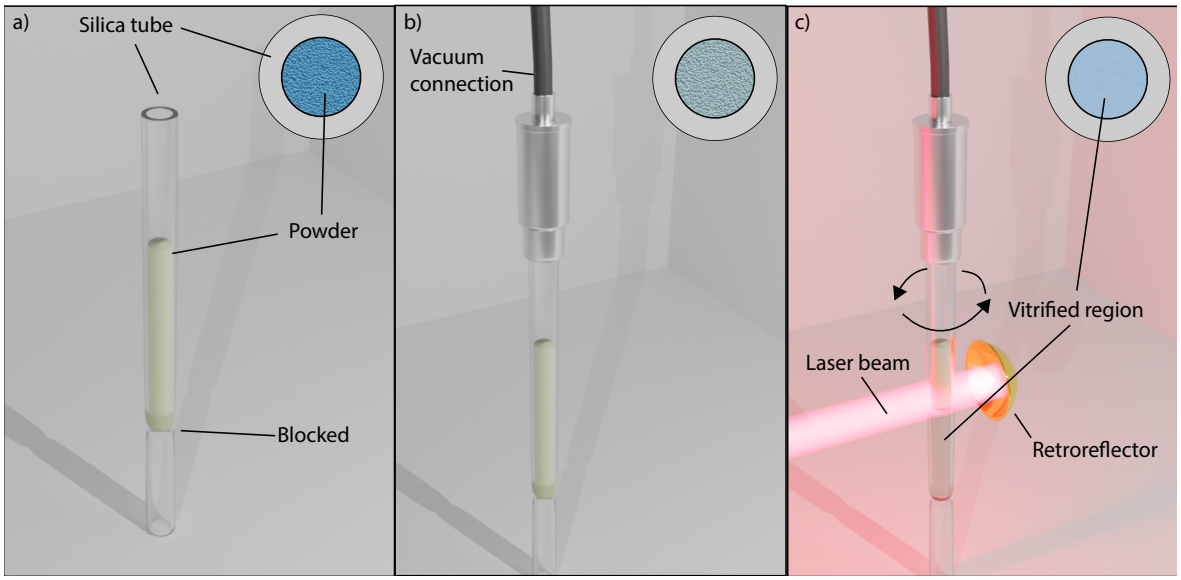

Figure 3.3: Illustration of the PLV process for the production of doped silica fiber preforms. a) Filling of a quartz tube with powder containing the doped core material. b) Evacuation and preheating. c) Laser vitrification of the preform. The insets show the cross section of the preform at each step.

essentially a one-step vitrification process, as schematically summarized in fig. 3.3.

The doped silica core material is prepared in powder form and filled into a fused silica tube that has been collapsed at its bottom end, forming a column of powder that fills the entire central cavity of the tube. The tube is connected to a vacuum system and may undergo a preheating process to remove impurities from the powder manufacturing process. The powder is then vitrified with a single pass of a CO_2 laser, completing the production of the core rod. To prepare the doped core material, granulated silica powder and the desired nanoparticle dopants are suspended in ethanol, combined, and stirred continuously while the ethanol evaporates under constant heating at 80 °C. Dopants for refractive index adjustment, such as aluminium or active rare earth elements, may be added to the suspension in the form of their chloride salts. Mixing in liquid suspension aims to achieve a homogeneously doped silica powder, where the dopants are adsorbed onto the pores at the surface of the silica granulate.

Thus, unlike the 3LV process, which achieves a homogeneous doping distribution down to the molecular level, the PLV process retains a degree of inhomogeneity at the scale of a single granulate particle, see fig. 3.4 for an example. The resulting dried powder is filled into a fused silica tube (typically 4 mm diameter, 1 mm wall thickness, 20 cm height of powder column) and preheated overnight under vacuum at temperatures between $300 - 800\,°C$, depending on the dopant chosen. Heating can be done using either a tube furnace or low power scanning laser irradiation to remove any residual moisture and organic impurities from the powder production process. Preheating is completed when the vacuum pressure drops to about 3×10^{-3} bar, close to the final pressure achievable with the vacuum pump, indicating no further outgassing from the powder. Without interrupting the vacuum, the tube containing the doped powder is vitrified using the laser vitrification setup described in section 3.1.2. The

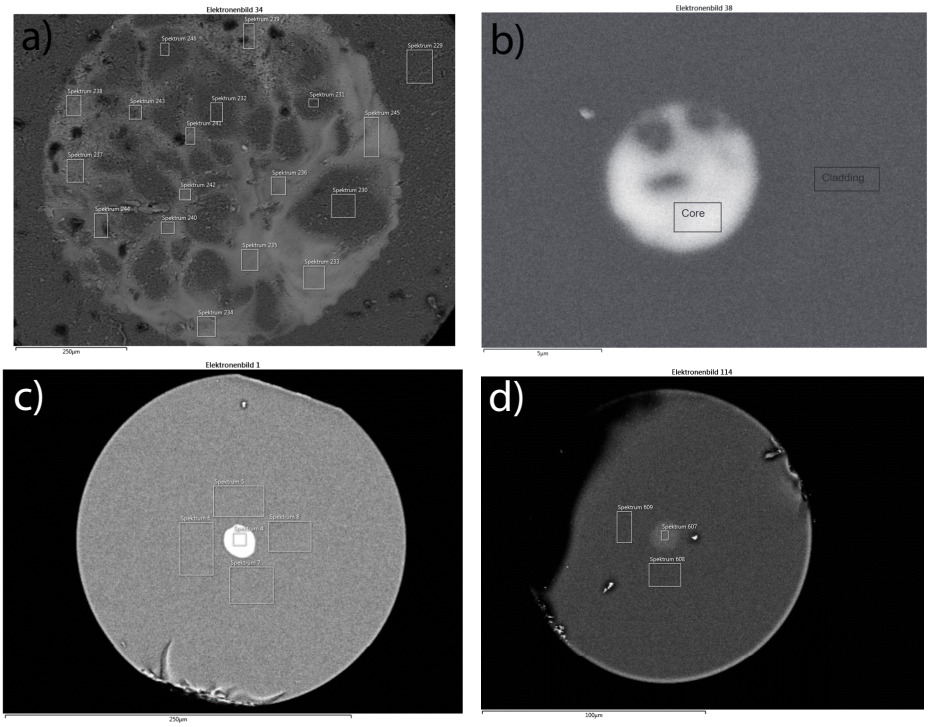

Figure 3.4: EDX images showing the influence of grain size in wet powder doping. a) Inhomogeneous doping distribution in a droplet of Al/Tb-doped silica powder with grain size 200 µm. (b) Fiber from the same powder after drawing. The inhomogeneities are smeared out and reduced to µm scale by drawing the fiber. (c) Al/Tb doped fiber using fumed silica powder. (d) 3LV based Yb doped fiber for comparison. The terbium doped fibers are shown in sec. 3.3.2. The ytterbium doped fiber is shown in sec. 3.2.1

vertical translation speed of the lathe is set to a few mm/s, much slower than in the 3LV method, to allow any vapors emitted during the powder melting and vitrification process to escape upward through the dense powder column and to avoid the formation of gas bubbles in the vitrified rod.

Since the PLV process produces preforms with a relatively large core diameter, jacketing of the core rod with cladding tubes is necessary for drawing single mode fibers.

3.1.5 Optimization of process parameters

When investigating novel doping materials, the thermodynamic properties of the resulting core material, its behavior during melting and subsequent cooling, and the optimal vitrification parameters are often unknown a priori. Laser vitrification provides a simple solution to this problem.

The small hot zone allows frequent variation of critical process parameters, such as laser power and tube feed speed, during the vitrification of a single preform. When using the PLV method, it is also possible to test multiple glass compositions in a single vitrification run by vertically stacking powders of different compositions in the same preform.

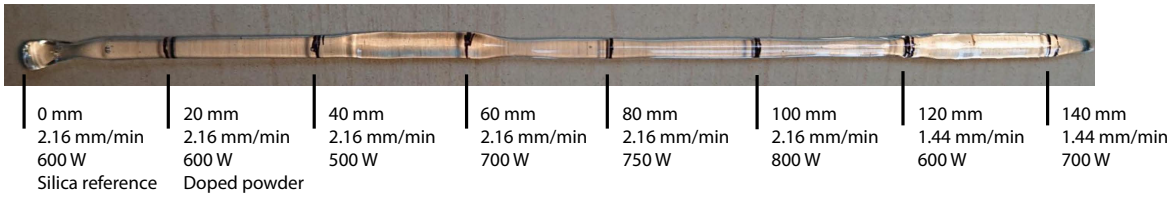

Figure 3.5: Example of a test preform used to optimize process parameters. The individual sections correspond to different process parameters. In this case the involved paramters are speed and power while the angular velocity was fixed.

An example of such a PLV test preform is shown in fig. 3.5. In this case, pure silica powder was used in the first 20 mm of the preform as a reference to start the vitrification process, followed by approximately 130 mm of doped silica powder containing a mixture of rare earths and aluminium at the percentage level.

The preform is divided into sections of approximately 20 mm, each of which is vitrified with a different set of parameters. By evaluating these different sections, e.g. by checking for visual defects or assessing the fluorescence lifetime of active dopants, it becomes easy to identify the optimal process parameters.

3.2 Realized fiber prototypes

In this section, we examine three different functionalizations of silica fibers fabricated by the 3LV and PLV methods. First, we present a Yb^{3+} / Al^{3+} codoped silica fiber designed as an active gain medium in a 1 µm fiber laser, and compare its absorption and emission characteristics with a commercial fiber fabricated using conventional CVD / solution doping techniques. Second, we demonstrate the versatility of our laser-assisted preform fabrication approach by introducing fibers doped with multiple active rare-earth ions, achieving fluorescence bandwidths exceeding one octave. Third, we describe the functionalization of a silica preform and fiber with nitrogen-vacancy (NV) fluorescent nanodiamonds and propose this as a novel approach for controlling the nonlinear refractive index of silica fibers.

3.2.1 Yb-doped aluminosilicate fiber

Ytterbium has attracted much research attention as a favorable rare earth ion for glass doping and active fiber development due to its useful laser transition around 1 µm, simple electronic structure, and high gain efficiency. Ytterbium-doped fibers are well established and widely used in various laser and amplifier applications, be it high power, narrow linewidth, or mode-locked [122–125].

These fibers are also used for fiber optic sensors or pumping Er in Er:Yb codoped fibers [126, 127]. Their widespread use means that Yb-doped fibers are very well characterized and readily available, making them an ideal testing ground for comparing the 3LV fiber with commercially available state-of-the-art products. Aluminium is added to the glass to ensure Yb solubility in the silica matrix.

3.2.1.1 Production

The preform is fabricated using the 3LV process described in section 3.1.3, using a fused silica tube of 4 mm outer diameter and 1 mm wall thickness, and applying five deposited layers. The target final ratio of relevant dopant ions in the SiO_2 matrix was 1 at.% Yb^{3+} and 10 at.% Al^{3+}.

Since the precursors contain only one relevant atom per precursor molecule, the desired ratio is quickly translated into the necessary recipe for about $50mL$ of sol, which is given in the table 3.1.

Atom	Target ratio (at.%)	Chemical	Molar ratio (mol.%)	Mass (g)
Yb	1	$YbCl_3 \cdot 6H_20$	0.1013	0.2894
Al	10	$AlCl_3 \cdot 6H_20$	1.0130	1.8054
Si	89	TEOS	9.0156	13.8187
-	-	Ethanol	78.70796	26.6782
-	-	HCl	0.0286	0.0078
-	-	H_2O	11.1336	1.4787

Table 3.1: Recipe for the YbDF2 fiber

To prepare 50 mL of sol, 0.29 g of $YbCl_3 \cdot {}_6H_2O$ (99.998 %, Sigma-Aldrich) and 1.8 g of $AlCl_3 \cdot {}_6H_2O$ (99.998 %, Sigma-Aldrich) were dissolved in 33.8 mL of absolute ethanol (EMSURE, Sigma-Aldrich). When the salts were completely dissolved, 14.7 mL of TEOS (for synthesis, 99 %, Sigma-Aldrich) was added. The viscosity of the sol, and thus the thickness of each deposited layer, was adjusted by adding small amounts of distilled water (1.48 mL) and hydrochloric acid (7 µL, 37 wt.%, Dr. Grogg Chemie AG).

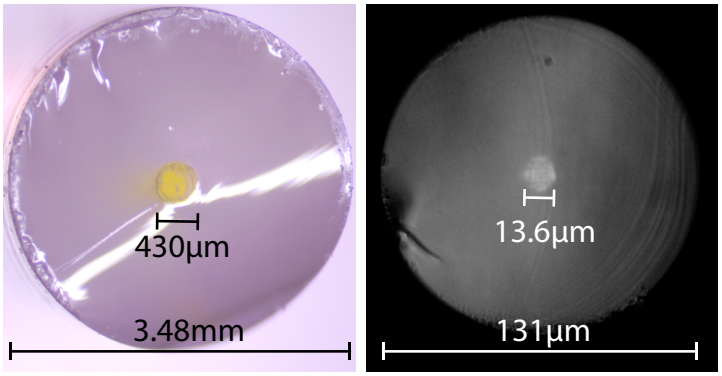

(a) Preform front view (b) Fiber front view

Figure 3.6: Pictures of the Yb-doped preform and fiber, core illuminated with white light

The cross section of the resulting collapsed preform is shown in fig. 3.6a. Based on its dimensions and using the principle of conservation of mass, we estimate the thickness of each deposited layer before collapse to be 9.4 µm.

The preform image shows a yellow coloration of the core. It is typically associated with Yb^{2+} species in the glass. It has been shown to form under reducing conditions during preform production. The concentration correlates with higher Al ratios,

adds absorption in the UV, reduces fluorescence lifetime and increases photodarkening. Codoping with phosphorus could reduce the amount of Yb^{2+} [15, 128, 129].

The preform was then drawn in a standard drawing tower to a fiber diameter of 130 µm. A commercial high index acrylate coating was applied to increase mechanical stability. A microscopic image of the cleaved front facet of the final fiber, designated YbDF2, is shown in fig. 3.6b, confirming good concentricity.

3.2.1.2 Refractive index and dopant concentration

The concentration of dopants in the fabricated fiber core was determined using energy-dispersive x-ray spectroscopy (EDX), revealing a composition of 0.44 at.% Yb and 8.1 at.% Al, referenced to Si. This corresponds to a Yb ion number density of about $1.23 \times 10^{20}\,\mathrm{cm}^3$. Therefore, compared to the chemical composition of the sol, the Yb doping concentration in the core of the final fiber has decreased to about half of its initial value. Diffusion and evaporation of dopants depend on the preform feed rate and drawing speed, as well as on the preform collapse parameters [130, 131].

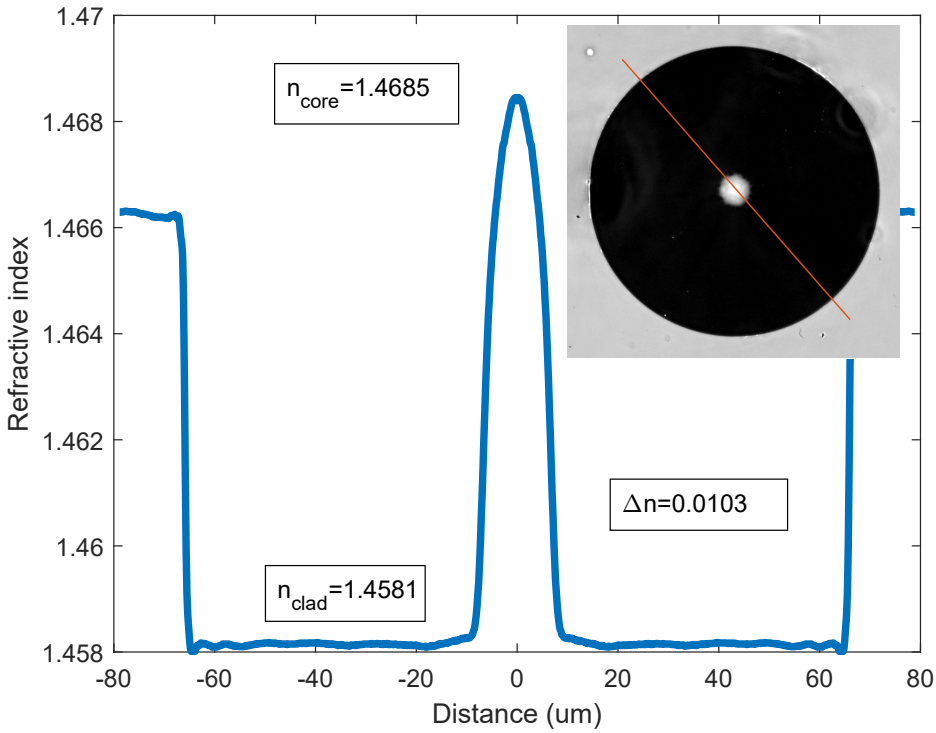

Figure 3.7: Refractive index profile of YbDF2. Measured with nPA-600 refractive index profiler, Arden Photonics

The RIP of the fabricated fiber was measured with a commercial index profiler (Arden Photonics, UK, nPA-600) and is shown in fig. 3.7. Diffusion effects contribute to the formation of a refractive index profile with a parabolic shape near the center of the core. A similar refractive index profile shape was observed in a commercial Yb-doped fiber used as a reference, indicating that this phenomenon is inherent to the high temperature drawing process of silica fibers rather than specific to a particular

preform manufacturing method. The core exhibits a maximum index step of $\Delta n = 0.0103$, corresponding to a numerical aperture of NA= 0.174. An additivity rule in [15] suggests almost identical values of $\Delta n = 0.0108$ and thus NA= 0.178, based on the relative distribution of the dopants. The core diameter, defined at the 5 % height of the maximum index step, measures about 17.3 µm.

Using a numerical mode solver with the measured refractive index profile, ten guided mode solutions were identified. The calculated mode field diameter of the fundamental mode at 1030 µm is approximately 8.4 µm, which is less than the measured value of 10.3 µm obtained from the divergence angle when the fiber is forced into single-mode operation with a tight mandrel wrap. Note that achieving single mode guidance in the fiber was not a goal of this study. Since the RIP deviates significantly from a step index profile, the fundamental mode also deviates from a Gaussian profile, so deviations are expected.

3.2.1.3 Absorption and emission characteristics

The fabricated fiber was subjected to a series of optical characterization measurements to evaluate its absorption and emission properties, and its performance was compared to a state-of-the-art commercial Yb-doped fiber. As a reference, we chose the Coherent YSF-HI-HP [132], since it is a widely used single-clad fiber for laser and amplifier systems with relatively high doping concentration. Using EDX, we determined a Yb doping level of about 0.17 at.% for the Coherent YSF, which is about one third of the doping level of our in-house fabricated YbDF2 fiber.

Fig. 3.8(a) shows the measured absorption spectra of both fibers. To accurately resolve the strong absorption peak around 976 nm, we used the fiber pinhole technique as described in [133]. In this method, a short piece (about 1 cm) of the fiber under test (FUT) is spliced between two PM980 fibers. These passive fibers act as pinhole fibers, ensuring that light is only coupled into and out of the fiber core. The shape of the absorption spectrum is then easily obtained by comparing the white light transmission spectra recorded with the FUT and the pinhole fibers alone. The absolute values were calibrated using a single wavelength cut-back measurement at 895 nm, where the lower absorption allows longer cut-backs and more accurate measurements.

For the YSF reference fiber, peak absorption values of 80 dB m^{-1} at 915 nm and 247 dB m^{-1} at 976 nm are determined, in excellent agreement with the manufacturer's specifications. The YbDF2 fiber exhibits significantly higher absorption, with peak values of 208 dB m^{-1} at 915 nm and 925 dB m^{-1} at 976 nm, reflecting its higher doping concentration.

Fluorescence properties were evaluated by exciting a short length of the FUT directly spliced to a single-mode 976 nm laser diode and measuring the fluorescence signal perpendicular to the fiber immediately after the splice to minimize reabsorption effects along the fiber path (Schwuchow et al., 2014 [133]). Fluorescence lifetime measurements (fig. 3.8 (b)) revealed nearly identical lifetimes of 820 µs for YbDF2 and 830 µs for YSF. This result indicates that despite the significantly higher doping concentration in YbDF2, the Yb ions are correctly embedded in the Si glass matrix without significant clustering, and the influence of possible Yb^{2+} ions is also minimal.

Finally, absorption and emission cross sections were calculated from the measured

attenuation and fluorescence characteristics, the Yb ion densities determined by EDX, and the measured refractive index profiles of both fibers [122]. The cross sections reflect the efficiency of the absorption and emission processes at the level of individual ions, independent of the geometrical design of the fiber and the doping concentration, and are therefore effective indicators of the quality of the doped glass material.

Fig. 3.8 (c) compares the results for YbDF2 and YSF fibers. We observe different performances of the fibers at the two primary absorption peaks. The YSF fiber shows a higher cross section at 915 nm, while our YbDF2 fiber shows a more pronounced peak at 976 nm. These variations can be attributed to differences in glass composition, such as the presence of additional phosphor co-doping in the YSF fiber, as indicated by our EDX measurements. Uncertainties in absorption measurements at high doping concentrations may also contribute to this result. In contrast, the important emission cross sections at and above 1030 nm are nearly identical for both fibers.

This result highlights that fibers fabricated using our laser-assisted rapid prototyping approach have emission characteristics comparable to those of commercial fibers fabricated using conventional CVD and solution doping techniques.

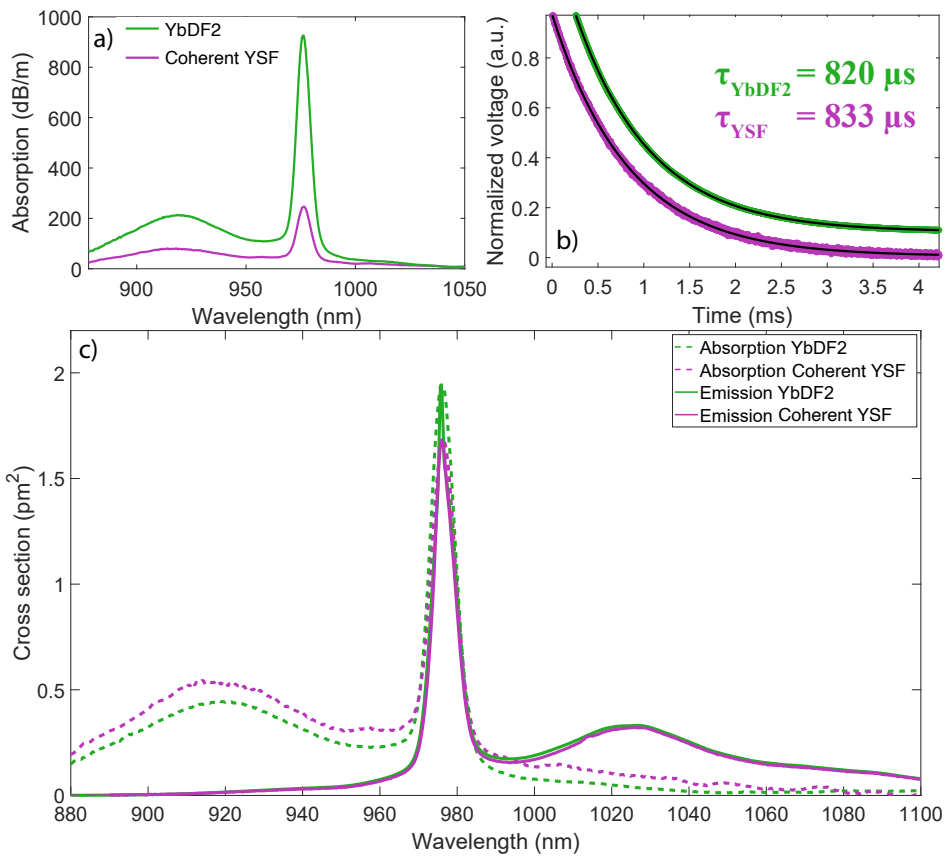

Figure 3.8: Fiber properties essential for laser applications compared to a commercial fiber. (a) Fluorescence lifetime pumped at 976 nm. (b) Absorption. (c) Absorption and emission cross sections. Absorption and emission peaks at 976 nm are assumed to be equal [122].

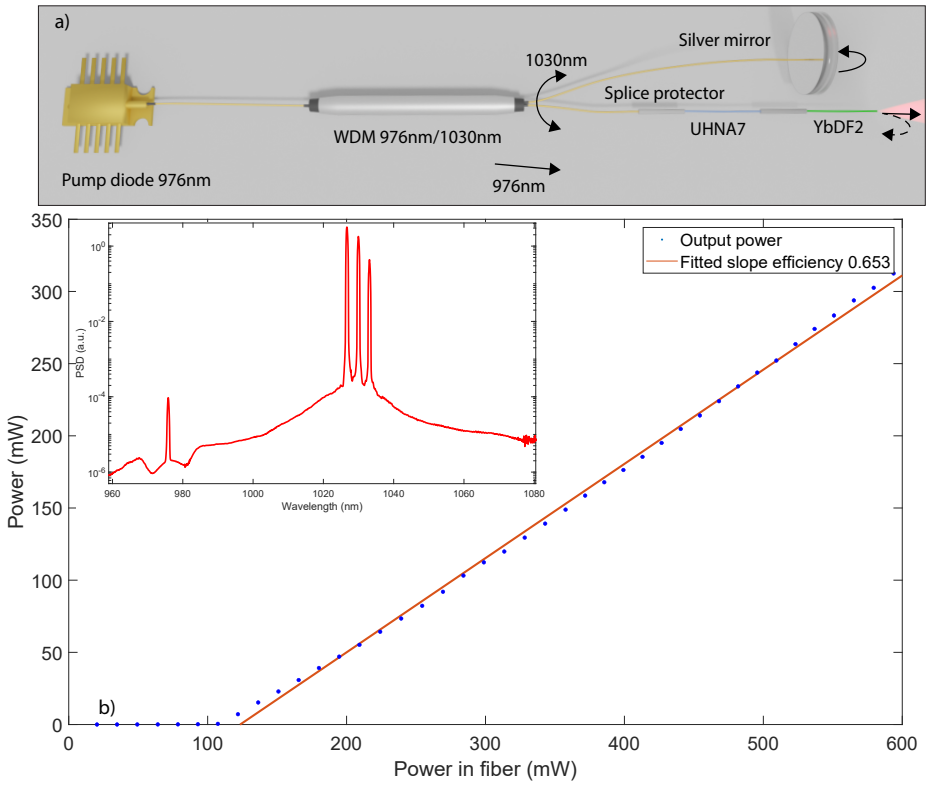

Figure 3.9: (a) Fiber optic setup for testing the gain capabilities of YbDF2, consisting of a pump diode, a WDM, a piece of UHNA7, and the YbDF2 fiber. The cavity is formed between the silver mirror and the output facet of the fiber. (b) Output power and slope efficiency of 66 %. The inset shows multiple laser lines appearing around the gain maximum of 1030 nm.

3.2.1.4 Laser experiment

To evaluate the CW lasing performance of the YbDF2 fiber, we constructed the Fabry-Perot test resonator shown in fig. 3.9(a). A single mode pigtailed pump diode operating at 976 nm and a 19 cm length of YbDF2 fiber were spliced to the pump and common port of a wavelength-division multiplexer (WDM), respectively. To minimize splice loss between the single-mode WDM pigtail and the multi-mode YbDF2 fiber, a mode field adapter consisting of a short segment of ultra-high numerical aperture fiber (UHNA7, Nufern) was used. By fine-tuning the arc time during splicing, the thermal expansion of the germanium-doped UHNA7 core can be controlled, reducing the total transmission loss to 10 % from an initial loss of over 30 %. The resonator is formed by a 100 % reflective silver mirror coupled to the signal port of the WDM and the cleaved end facet of the YbDF2 fiber, resulting in a Fresnel reflectivity of about 4 %.

Figure 3.9 (b) shows the lasing characteristics of the YbDF2 fiber in an output power range up to 310 mW, limited by the pump power. The slope efficiency with respect to the absorbed pump power was determined to be about 66 %, which is an excellent value considering the mode mismatch and excess loss in the cavity. Optimizing the geometrical dimensions of the active fiber for single mode guiding and reducing the splice loss with standard passive components should result in efficiencies well above

70 %, which is in the same range as could be obtained with commercial Yb-doped silica fibers. As expected for a free-running laser, a multi-peak emission spectrum was recorded near the gain maximum of 1030 nm, as shown in the inset of fig. 3.9 (b).

3.2.2 Multi rare rarth doped fiber

To demonstrate the flexibility of our laser-assisted rapid prototyping process, we fabricated fibers with more than an octave of near-infrared fluorescence bandwidth by doping with multiple active rare earth ions. These fibers are potentially useful as ultra-broadband superluminescent light sources, combining the high spatial coherence of single-mode fibers with very low temporal coherence resulting from the large emission bandwidth [134]. This unique combination of low temporal and high spatial coherence is particularly advantageous for applications in optical coherence tomography, device characterization, and optical sensing [135].

In addition, multi-dopant fibers offer a promising solution for overcoming the gain bandwidth limitations inherent in fiber amplifiers that rely on a single active dopant. By incorporating multiple dopants with adjacent gain bands, these fibers can potentially expand the useful transmission bandwidth of telecommunication networks [136]. In addition, they could open up new possibilities in the amplification of few-cycle pulses, which are essential for various advanced applications in ultrafast optics and high-precision measurements [137].

For this demonstration, we fabricated two multi-doped fibers, one using the 3LV process and the other using the PLV process, designated MD-3LV and MD-PLV, respectively. The dopant compositions were chosen to combine several active rare earth elements with near-infrared emission bandwidths:

Ytterbium (Yb; $1.0 - 1.1$ µm), Neodymium (Nd; $0.9 - 1.03$ µm, $1.03 - 1.1$ µm, and $1.32 - 1.35$ µm), Bismuth (Bi; $1.1 - 1.5$ µm), Erbium (Er; $1.5 - 1.6$ µm), Thulium (Tm; $1.45 - 1.53$ µm and $1.7 - 2.1$ µm), and Holmium (Ho; 2.1 µm). The solubility of the ions in the fused silica matrix was ensured by co-doping with alumina. The detailed composition of both fiber cores is given in the table 3.2.

Element	MD-3LV	MD-PLV
Yb (at.%)	0.19	0.06
Er (at.%)	0.13	0.06
Tm (at.%)	0.26	0.06
Ho (at.%)	-	0.06
Nd (at.%)	-	0.06
Bi (at.%)	-	1.20
Al (at.%)	5.03	3.00

Table 3.2: Element concentrations in at.% for MD-3LV and MD-PLV samples.

Fluorescence spectra recorded in transmission at the end of the fiber samples are shown in fig. 3.10. Both fiber samples exhibit more than an octave of fluorescence bandwidth at a single pump wavelength, but there are important differences due to the core glass compositions.

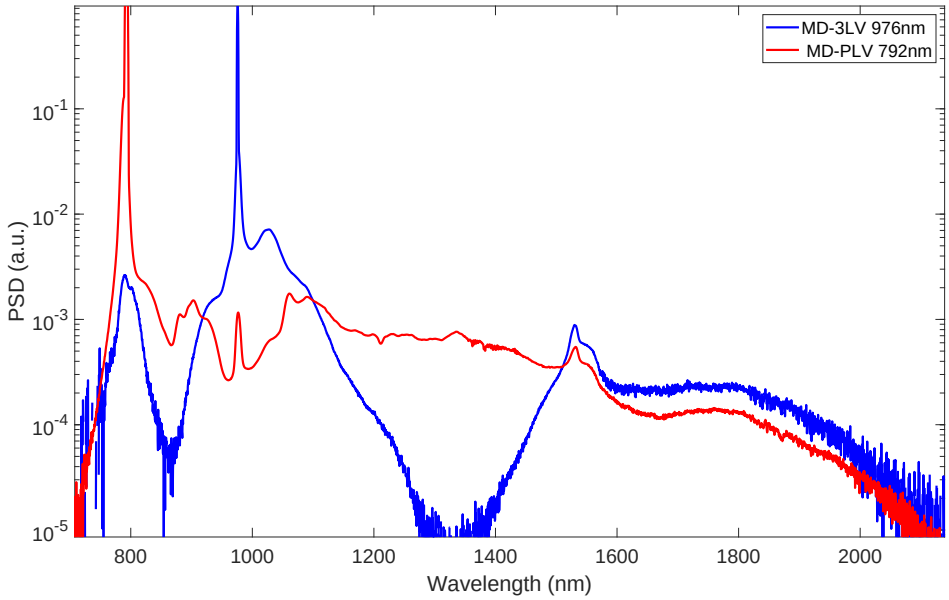

Figure 3.10: Broadband emission from the multi-dopant fiber fabricated by the 3LV and PLV methods. Blue shows the fluorescence of the 3LV fiber containing Yb, Er, and Tm. It is pumped at 976 nm. Red is the fluorescence of the PLV fiber. It also contains Ho, Nd and Bi. The latter two fill the hole around 1.3 µm when pumped at 792 nm.

The MD-3LV fiber was pumped with a 976 nm laser diode, ensuring that most of the pump light is absorbed by the Yb ions, which then transfer energy to Er and Tm ions by a mechanism similar to that in Er-Yb codoped fibers [138]. Three distinct emission bands are observed centered at 1.03 µm, 1.53 µm, and 1.9 µm, corresponding to Yb, Er, and Tm ions, respectively. A gap in the spectrum is observed around 1.3 µm, where none of the dopants show fluorescence emission.

Pumping with a 792 nm laser diode is more appropriate for the composition of the MD-PLV fiber, resulting in a relatively smooth and continuous fluorescence spectrum spanning $900 - 2100$ nm. The gap around 1.3 µm observed in the MD-3LV fiber is closed by the addition of Nd and Bi, which have strong emission bands in this region.

Due to the complexity of the nuclear composition, the exact excitation mechanism for all dopants is unknown. The 792 nm pump light can be directly absorbed by Nd, Bi, and Tm ions, bringing them into their excited states. From there, energy transfer, emission, and reabsorption processes are likely to occur, resulting in the simultaneous excitation of all active dopants and the formation of the continuous fluorescence spectrum.

These proof-of-concept experiments demonstrate the possibility of obtaining broadband emission from a single silica fiber doped with multiple rare earth dopants. It is clear that the core composition, the balance of doping concentrations, and the pumping scheme are key factors influencing the shape of the emitted spectrum and the efficiency of the excitation processes. It will be necessary to fabricate a series of fibers with variations in these parameters in order to understand the complex interactions between the dopants and to obtain a fiber suitable for broadband light amplification. The laser-assisted rapid prototyping techniques presented in this manuscript are well suited for

this purpose.

3.2.3 Nanodiamond doping

Control of nonlinear processes is important for a wide range of applications, including telecommunications, ultrafast photonics, and biophotonic imaging [21]. The dominant optical nonlinearities in silica fibers are induced by the nonlinear Kerr effect, which describes an intensity-dependent refractive index, $n(I) = n_0 + n_2 I$, where n_0 and n_2 represent the linear and nonlinear refractive indices, respectively [44].

Traditionally, n_2 was considered a nearly constant material property. Changing its magnitude typically required changing the host material, which often leads to handling and system integration challenges [139].Nanoparticle doping is a promising approach to control n_2 by introducing small amounts of highly nonlinear dopant materials while retaining silica as the host [9, 140]. Nanodiamonds in particular are of interest because they can exhibit a negative n_2 value [141, 142], which could potentially reduce or even neutralize the positive Kerr nonlinearity of silica glass.

However, the low dissociation temperature of nanodiamonds, around 600 °C, has prevented the development of ND-doped silica fibers, limiting previous studies to soft glass materials with lower melting points, such as tellurite and silicate glasses [26, 143, 144]. The high optical attenuation and significantly greater nonlinearity of these glass materials compared to silica have previously prevented the observation of any effect of ND doping on the n_2 value of the resulting fiber.

Here, we demonstrate that the unique features of laser-assisted preform fabrication enable the production of ND-doped silica fibers despite the high processing temperatures. A reduction in the n_2 value is observed in the ND-doped preform core, and the attenuation of the fabricated fibers is shown to be sufficiently low to allow nonlinear characterization experiments.

3.2.3.1 Production

The preform for the ND-doped silica fiber was fabricated using the PLV process described in section 3.1.4. Fluorescent nanodiamond particles (NDNV140nmHi, Adamas Nanotechnologies, USA) with an average diameter of 180 nm and containing negatively charged nitrogen-vacancy (NV) color centers were selected to facilitate the identification of nanodiamonds in the fabricated preforms. Granulated silica powder and nanodiamonds at a concentration of 10 µg per 1 g of silica (10 ppm) were suspended in ethanol. This mixture was stirred continuously while the ethanol was evaporated under constant heating at 80 °C.

The resulting dried powder was then filled into a silica tube (4 mm outer diameter, 1 mm wall thickness) and, after preheating to a maximum temperature of 600 °C, the vitrification process parameters were optimized using the procedure described in section 3.1.5. Compared to the vitrification of a pure silica preform of the same dimensions, we found that a significant reduction in laser power by nearly 50 % to 350 W and a relatively fast translation speed of 1.44 mm/min were necessary to obtain preforms

without visible defects. We attribute this to the high thermal conductivity of nanodiamonds and the associated changes in the thermodynamic properties of the silica/ND hybrid core material.

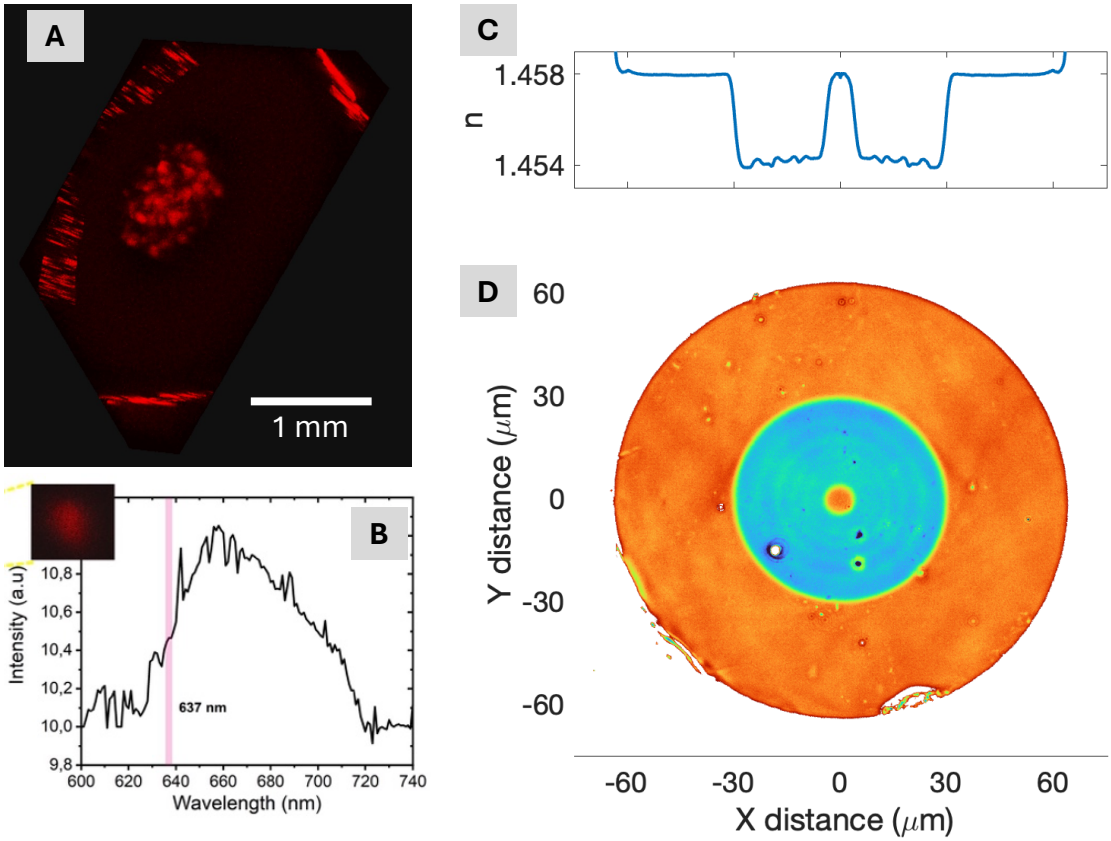

Figure 3.11: (a) Confocal microscopy of a piece of preform polished to a disk. Emission from the nanoparticles is visible in the core. (b) Emission spectrum of the particles in the preform. Pumped at 532 nm. (c) RIP profile (Arden Photonics) (d) RIP image showing the fiber structure

.

3.2.3.2 Preform and fiber characterization

The survival of nanodiamonds in the preform was confirmed using confocal microscopy on a polished 2 mm thick slice cut from the preform. Fluorescence from the NV color centers with its characteristic spectral shape was observed in the core region under 532 nm laser excitation, as shown in fig. 3.11(a)+(b). The reduced laser power, small hot zone, and limited heat exposure time are likely factors that contribute to a significant fraction of nanodiamonds surviving the preform fabrication process despite the high temperature environment required for silica vitrification.

Further characterization of the nonlinearity of the fabricated preform using the z-scan technique (see fig. 3.12) revealed a 20 % reduction in the magnitude of n_2 compared to a pure silica reference sample fabricated using the same technique. The value of n_2 decreased from $n_2 = 2.3 \times 10^{-20}\,\mathrm{m^2/W}$ for the pure silica preform to $n_2 = 1.8 \times 10^{-20}\,\mathrm{m^2/W}$ for the ND doped preform, measured at 1030 nm. The different absorption values measured indicate different doping concentrations, which correlate with decreasing n_2 values. Full details are published in Stepniewski et al. 2023 [38].

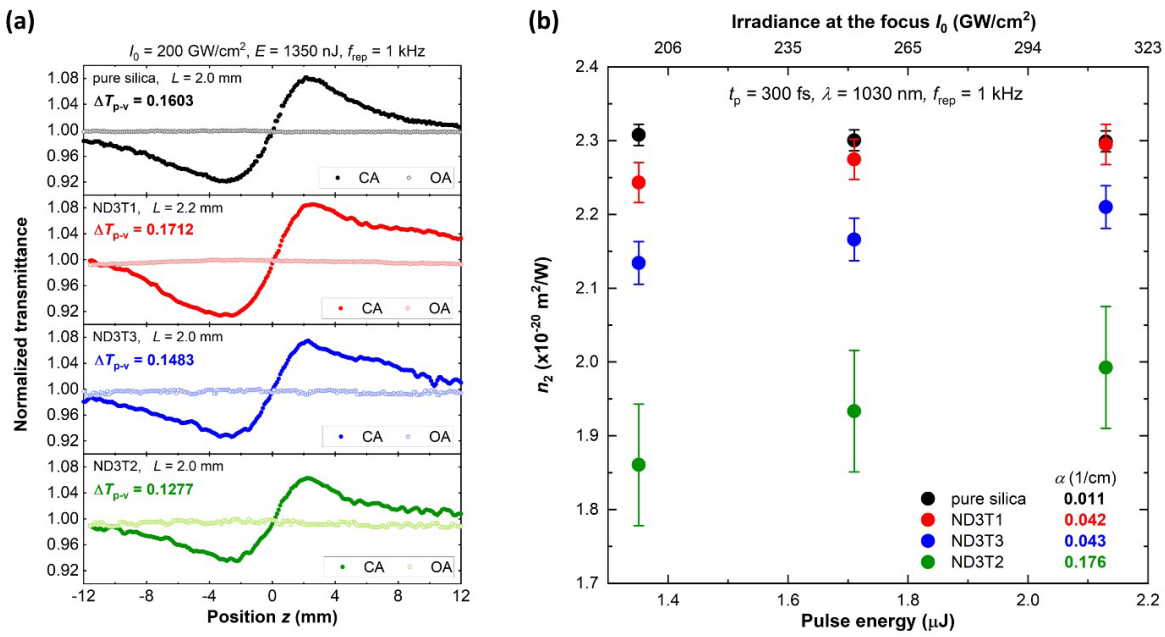

Figure 3.12: (a) z-scan measurements for a reference sample of silica and ND doped preform disks. (b) Extracted n_2 values for different pulse energies. The inset shows the measured absorption in the samples, indicating different doping concentrations.

Since ND doping is not expected to significantly change the refractive index of the core, the preform was first jacketed with a low index fluorine doped cladding tube to form a light guiding structure, followed by a pure silica cladding tube to adjust the final core-cladding ratio of the fiber, which was drawn in a standard silica drawing tower. The refractive index profile of the fabricated fiber, measured with a commercial index profiler (Arden Photonics, UK, nPA600) and shown in fig. 3.11(c) and (d), confirm that the core index remains unchanged by the ND doping, matching the refractive index of the outer pure silica cladding. The NA ($\simeq 0.1$) is defined by the index step to

the fluorine-doped silica cladding, and the core diameter is approximately 10 µm.

Since the presence of nanoparticles can result in scattering losses, the attenuation of the fiber was measured using the cut-back technique at 976 nm, resulting in a value of 0.145 dB m^{-1}. These losses are orders of magnitude lower than those reported for ND-doped soft glass fibers. The dispersion and mode field diameter at 1030 nm were also determined (fig. 3.13 (b)). The angular intensity scan and beam profile confirm

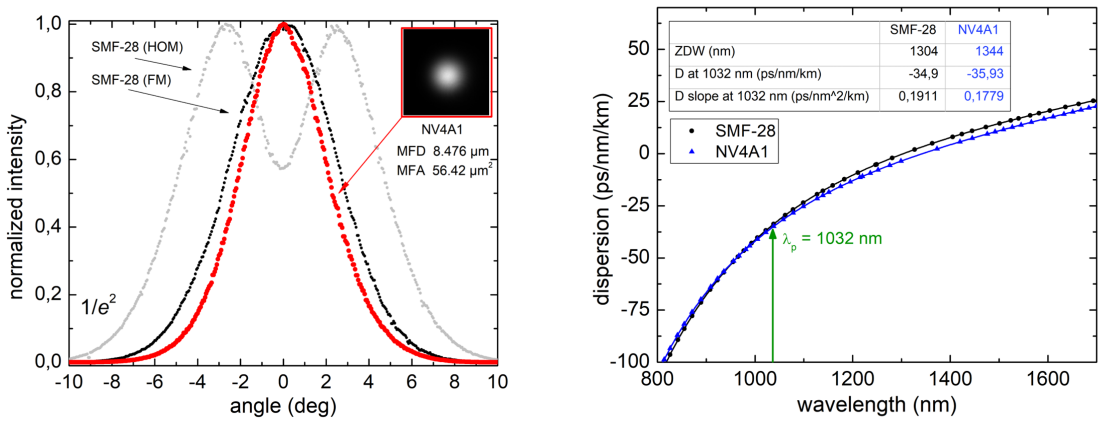

(a) (b)

Figure 3.13: (a) Determination of the mode field diameter at 1030 nm using an angular intensity scan. (b) Dispersion of NV4A1 ND-doped fiber compared to SMF-28.

single mode operation of the fiber. The MFD of 8.476 µm will be relevant for the nonlinearity measurements below. Crucially, the dispersion of the nanodiamond doped fiber is not significantly different from the commercial silica core fiber (SMF28).

3.2.3.3 Effect of nanodiamond doping on fiber nonlinearity

Pulse propagations using two different laser systems at 1560 nm and 1050 nm were used to estimate the n_2 of the ND fiber. Using an erbium-doped fiber laser at 100 fs and 40 MHz, we pump a 16 cm section of the ND fiber, achieving 175 mW of coupled power. The pulse shape, including phase, was determined using time-domain ptychography (TDP) [145, 146]. The same laser source was used extensively in other experiments. The peak power was measured at 28 kW. For further details see section 4. The recorded spectrum is shown in fig. 3.14 together with simulated spectra corresponding to different values of n_2, which is the only free parameter in the simulations.

The simulations were obtained by solving the generalized nonlinear Schrödinger equation (GNLSE) with the pulse electric field and the fiber parameters presented above as inputs. The GNLSE is a more general version of the equation shown in sec. 2.1.5.1 and includes Raman scattering.

The measured pulse spectrum shows significant broadening due to nonlinear pulse propagation. The spectrum is significantly broader than would be expected from pure silica with $n_2 = 2.3 \times 10^{-20}\,\mathrm{m^2/W}$. The closest match between simulation and measurement is obtained with $n_2 = 4.1 \times 10^{-20}\,\mathrm{m^2/W}$. The match on the long wavelength

side is really good, but on the short wavelength side the more complex spectral features are not exactly reproduced, possibly due to changing values of n_2 with wavelength in the fiber.

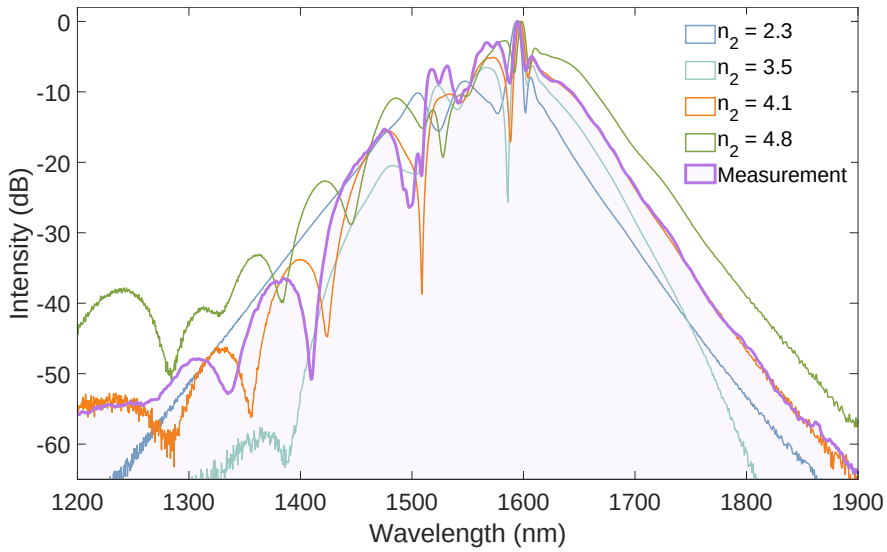

Figure 3.14: Measured spectrum after the ND doped fiber and simulated spectra using different values of n_2, given in units of $10^{-20}\mathrm{m}^2/\mathrm{W}$.

For this reason, we focus on the central part of the spectrum and determine the $-40\,\mathrm{dB}$ width and compare it to the original spectrum. An example is shown in the figure below (fig. 3.15).

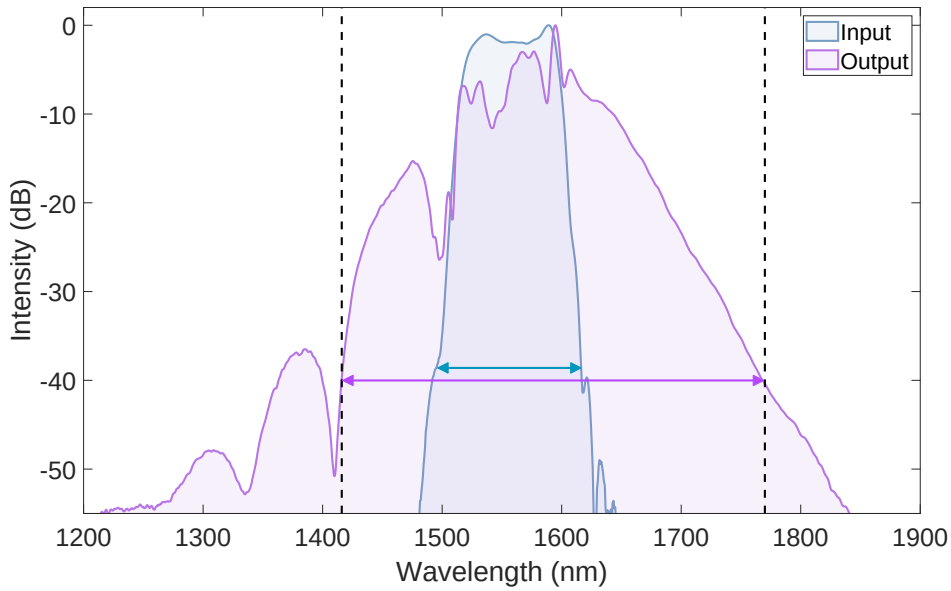

Figure 3.15: Comparison of the 40 dB spectral width of the input and output pulse at 175 mW average power. The initial width was 15.5 THz, which increased to 42.3 THz after the fiber. This gives a broadening factor of 2.7

Since this broadening factor is power dependent, we perform a power sweep as

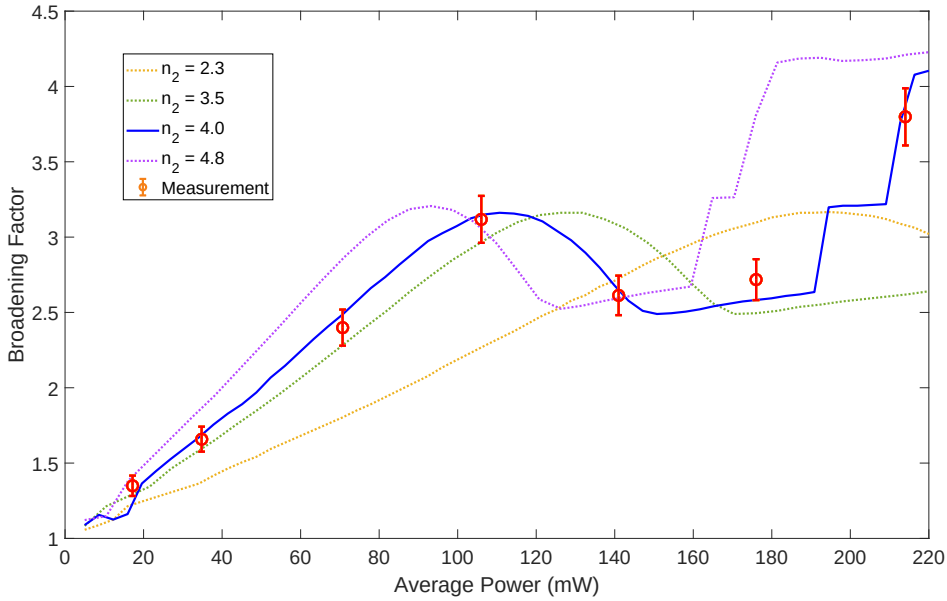

Figure 3.16: Broadening factor curves for different n_2 values compared to the measured values. n_2 is given in units of $10^{-20}\mathrm{m}^2/\mathrm{W}$. The best fitting value of $n_2 = 4$ is shown as the solid blue line. Dotted orange corresponds to pure silica

.

shown in fig. 3.16. The broadening is not strictly linearly increasing, but varies due to complex nonlinear dynamics in the anomalous dispersion region of the fiber. The complex shape of this curve allows us to get a closer fit to n_2. The measured broadening factor curve has distinct characteristics. Therefore, the values of $n_2 = (2.3, 3.5, 4.8) \times 10^{-20}\,\mathrm{m}^2/\mathrm{W}$ can be rejected because they cannot reproduce its shape. However, with $n_2 = 4.0 \times 10^{-20}\,\mathrm{m}^2/\mathrm{W}$ the features are accurately reproduced. This value shows a significant increase of n_2 at 75 % compared to pure silica.

The behavior of pulses from a 1050 nm source with 350 mW average and 28 kW peak power is much simpler, since the fiber normal dispersion is zero in this wavelength range. The dynamics are simply described by SPM. The spectrum and broadening factor curves are shown in fig. 3.17(a)+(b). The figures show that the broadening increases linearly with n_2 and increasing power. By comparing the spectra, the best fit is obtained with $n_2 = 1.9 \times 10^{-20}\,\mathrm{m}^2/\mathrm{W}$. This value is supported by the broadening curves in fig. 3.17 (b).

Curves corresponding to different n_2 have a distinct slope and can be easily distinguished. To check the validity of the method, it is repeated with a standard PM980 fiber. The spectra and broadening factors for the 1050 nm are shown in fig. 3.18 below. The simulated spectra are clearly distinguished as they become broader with n_2. We get a pretty good fit with $n_2 = 2.3 \times 10^{-20}\,\mathrm{m}^2/\mathrm{W}$, which is the established value for pure silica and thus confirms the accuracy of the method. The same conclusion is drawn from the broadening factor curve.

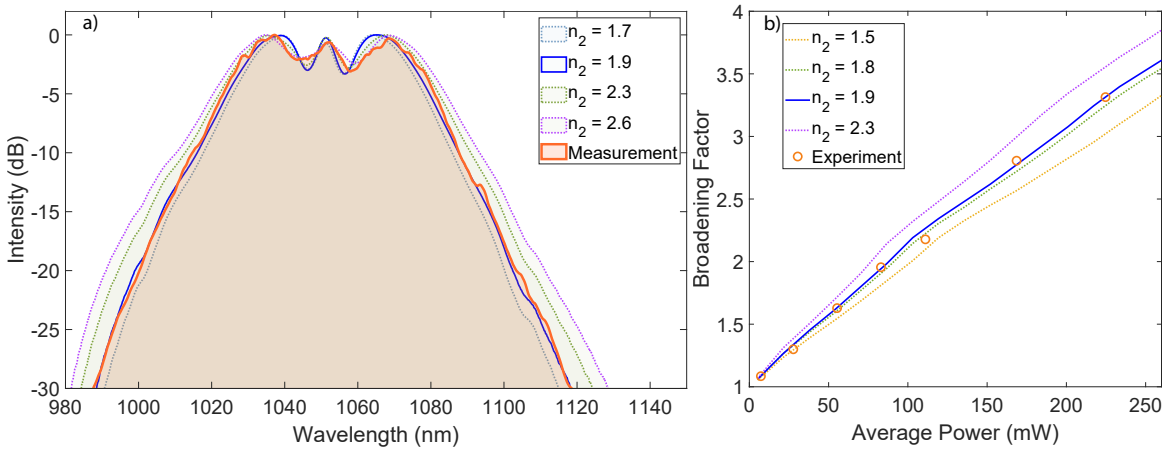

Figure 3.17: (a)Measured spectrum (orange) compared with simulations using different n_2 values. (b) Broadening curves at the $-20\,\mathrm{dB}$ level. The broadening increases monotonically and linearly with n_2 and power. The best fit in both cases is given by $n_2 = 1.9$. All n_2 values in units of $1 \times 10^{-20}\,\mathrm{m}^2/\mathrm{W}$.

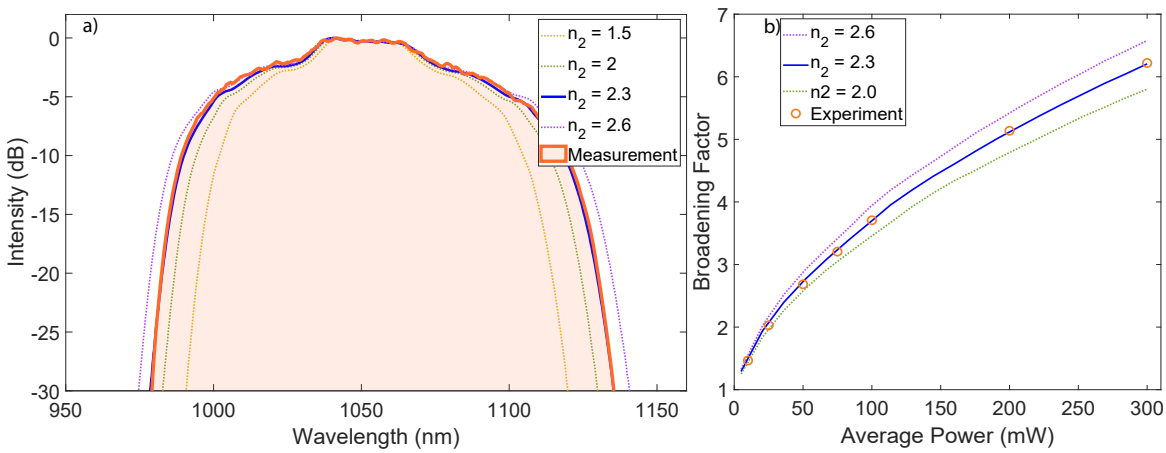

Figure 3.18: (a) Measured and simulated spectra for PM980 pumped at 1060 nm. (b) Measured broadening factor versus values from simulation with different n_2.

3.2.3.4 Conclusion of nonlinearity experiments

The nonlinearity in the nanodiamond doped fiber was measured to be significantly different from its initial host material, silica. A summary of the measurements in the previous section is given below (figure 3.19). The extracted value at 1050 nm is $n_2 = 1.9 \times 10^{-20}\,\mathrm{m}^2/\mathrm{W}$ and at 1550 nm it is $n_2 = 4 \times 10^{-20}\,\mathrm{m}^2/\mathrm{W}$. These measurements indicate a strong dispersion of n_2, and extrapolation of the values suggests a possible negative nonlinearity at shorter wavelengths, as has been suggested for other nanoparticles [23].

Negative nonlinearity would greatly expand the possibilities for exploiting nonlinear effects by allowing soliton formation in the normal dispersion regime. With proper tuning of the fiber properties, it may even be possible to achieve full-spectrum soliton operation [37].

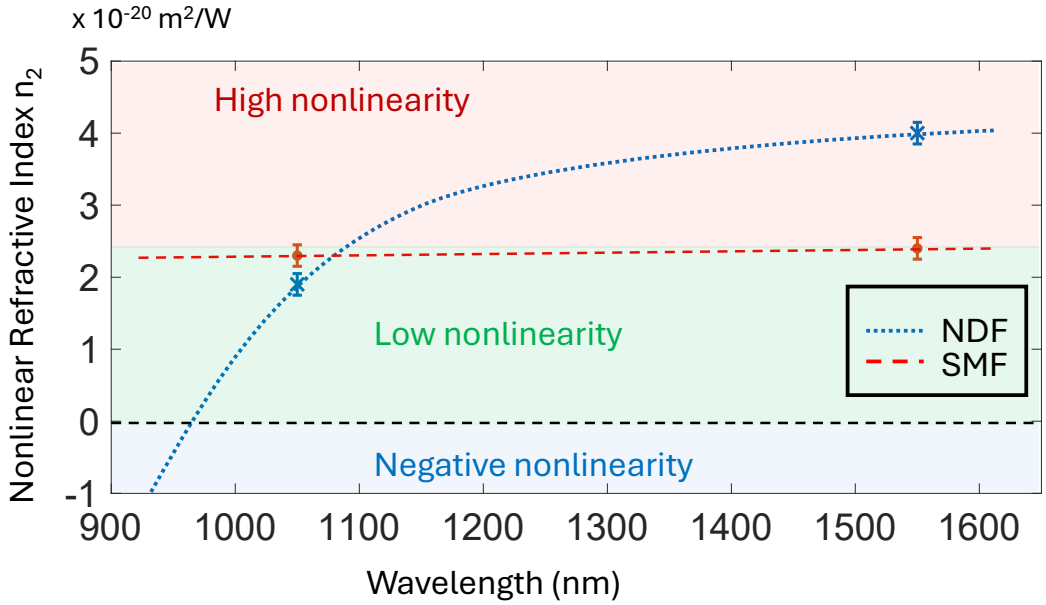

Figure 3.19: Measured n_2 values in nanodiamond doped fiber (blue) and silica core SMF. The dashed red line indicates the low n_2 dispersion, while the dashed blue line highlights the strong n_2 dispersion between the measured points. Its extrapolation suggests the possibility of negative n_2 at shorter wavelengths

However, this will have to be proven by further experiments, as our attempts to obtain n_2 values at shorter wavelengths failed due to the more complex pulse shape of the available source, as well as the onset of higher order modes. Incorporating the full characterization of the electric field using time-domain ptychography at both fiber ends, or an approach based on fundamental conservation laws as in Castello-Lurbe (2023) [147] may prove useful.

Even without speculative extrapolation, we have shown the possibility of changing the nonlinearities in a fiber independently of its geometry and dispersion (fig. 3.13). In the future, this should allow much easier engineering of dispersion and nonlinearity in optical fibers. In addition, it seems possible to reduce or even eliminate the nonlinearity, which would be advantageous for telecommunication or high-power and ultrafast applications.

3.3 Other prototyping methods

Alternative methods have already been established at the IAP and BFH, such as producing the desired glass compositions by direct mixing of the corresponding oxide powders, or by producing a doped TEOS-based sol-gel, which turns into the desired silica powder after drying. A variety of different fibers based on the fumed silica method have already been realized. These include an extensive set of differently Al and P codoped Yb fibers with the aim of analyzing their effect on Yb spectroscopy [112], mechanically homogenized oxide powder mixtures [114], or sol-gel based silica powder with an emphasis on the intrinsic doping homogeneity of the process [148].

An adaptation of the granulated silica method is presented in the form of a Yb-doped aluminium core fiber fabricated by direct drawing of an oxide powder mixture, which has been thoroughly characterized and also evaluated for its gain capabilities in a laser and amplifier configuration.

Also described is a series of terbium-doped fibers fabricated by a variety of methods with varying doping concentrations. These fibers were designed to measure magnetic fields using the Faraday rotation of polarized light as it propagates through a medium exposed to a magnetic field.

3.3.1 Ytterbium-doped aluminium core fiber by direct powder mixing

This section is based on the following publication:
D. Blaser, P. Hänzi, S. Pilz, A. Heidt, V. Romano. "Multimode Ytterbium Aluminosilicate Core Optical Fiber for Amplification and Laser Applications".
Fiber 2023, 11, 95
`https://doi.org/10.3390/fib11110095`

Aluminium oxide has a higher melting temperature than silica. A higher melting point, as well as a higher specific heat and significantly higher thermal conductivity than silica, suggest an improved thermal damage threshold. These properties make high aluminium content fibers interesting candidates for high power CW applications. Taking advantage of the extended transparency at longer wavelengths of Al_2O_3 compared to silica could allow the realization of laser glasses or fibers typically reserved for IR transparent soft glasses, such as dysprosium and erbium in ZBLAN [149, 150] or InF_3. [151, 152]. In addition, increasing the Al content increases the glass density, acoustic velocity and decreases the photoelastic constant, resulting in a greatly reduced Brillouin gain coefficient [153].

The solubility of Rare Earths in the glass matrix is a major limitation on the maximum achievable doping concentration, as Rare Earth ions form clusters at high concentrations in a silica matrix unless the glass is appropriately codoped. Clustering leads to quenching effects and alters the spectroscopy and efficiency of the active fiber. Aluminium co-doping of silica improves the solubility of rare earths and allows the production of fibers with higher doping levels [154]. These are prerequisites for higher gain and allow the active fiber length to be reduced, which in turn reduces dispersion

and nonlinearities.

Here we demonstrate the feasibility of a fiber with an alumina core and a high ytterbium doping concentration of 3 at.%. We describe the doping process of an aluminium oxide powder in an ethanol suspension containing the dissolved Yb precursors. The fiber is drawn using the powder-in-tube technique, its composition and optical properties are analyzed, and its performance is tested in a laser and amplifier configuration.

3.3.1.1 Precursor and fiber fabrication

The powder-in-tube technique is used to fabricate the presented fiber. The preform assembly consists of a thin-walled silica capillary (4/2.75 mm outer/inner diameter) containing the Yb/Al powder prepared from a slurry. The alumina powder is suspended in an ethanol solution containing the dissolved ytterbium chlorides. The slurry is dried under heat and mechanically refined by milling and sieving. The powder carrying capillary is placed inside a larger silica tube (20/17 mm OD/ID) and the remaining gap is filled with pure silica powder (Silitec). Drawing was performed at 2035 °C, which is higher than required for silica-based preforms. A light vacuum was applied to release gases trapped between the powder particles and to control volume shrinkage during vitrification. The target dimensions were 45 µm core diameter and 350 µm shell diameter.

3.3.1.2 Geometry, composition and refractive index

Figure 3.20 (a) shows a micrograph of a polished fiber sample. The core is illuminated with a white light source, revealing a round core shape and fiber dimensions consistent with the target size. A line scan of the core region was performed by EDX and is shown in fig. 3.20 (b).

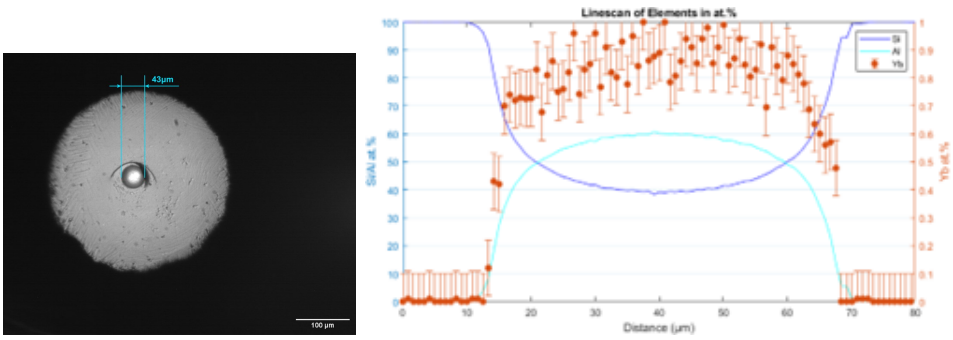

(a) (b)

Figure 3.20: (a) Polished fiber facet with white light back illumination. The core and cladding diameters are 45 µm and 350 µm respectively. (b) EDX line scan

In the center of the fiber core we measure a composition of 60 at.% Al, 1 at.% Yb and 39 at.% Si. Towards the edges of the core region, the Si concentration increases and the Al concentration decreases until they reach the pure silica in the cladding. Therefore, compared to the initial preform core composition of 97 at.% Al and 3 at.% Yb, significant diffusion has taken place during fiber drawing, greatly reducing the

aluminium and ytterbium concentrations. The asymmetry in the elemental distribution at the core-cladding interface reveals Si as the most mobile element, as significant amounts have diffused into the initially pure ytterbium and aluminium oxide core region, while diffusion of core material into the cladding is minimal. This is consistent with the different material viscosities [155], as well as the elemental distribution in the fibers previously presented in sec. 3.2.1, which are a commercially available Yb-doped fiber and one produced by the 3LV method. Examples based on modified chemical vapor deposition (MCVD)/solution doping can be found in [156]. The core composition is greatly reduced by a factor of 2-3. In the case of ytterbium doping, the diffusion effects can simply be mitigated by increasing the initial concentration accordingly, whereas the aluminium concentrations cannot be increased further. Shielding the core from the surrounding silica by replacing the inner silica tube with an aluminium oxide tube could possibly mitigate the diffusion, although one would have to deal with a double cladding structure.

According to the additivity rule for the refractive index found in [15] or the sum weighted by the fractional volume of each dopant as in [157], the refractive index will follow the elemental distribution of the elements corresponding to the higher refractive index in fig. 3.20, with an estimated maximum refractive index of $n = 1.5607$ at 633 nm based on the volumetric mean and the refractive index from [158]. This means that the profile deviates slightly from the optimal step index profile. The NA is estimated to be $NA = 0.56$. An additional cutback measurement showed a background loss of $1.66\,\mathrm{dB\,m^{-1}}$ at 1550 nm. The fiber coupled light source was butt coupled directly to the FUT. The fiber length was reduced from 4924 mm in five approximately 1 m intervals.

3.3.1.3 Fluorescence and spectroscopy

The absorption and fluorescence properties of the fiber were analyzed. The absorption spectrum was obtained by simple cutback using a white light source. The fluorescence spectrum, pumping the fiber at 976 nm, was measured from the side of a short fiber sample by placing the fiber in an integrating sphere and connecting it to a spectrum analyzer with a high NA fiber. Using the Füchtbauer-Ladenburg relationship and the measured fluorescence lifetime of 1.2 ms, the emission cross section for the sample was calculated [159]. The peak of the emission cross section was assumed to be equal to the maximum of the absorption cross section. The results agree with the typical cross section for commonly used ytterbium-doped fibers [122], as shown in fig. 3.21a.

3.3.1.4 Laser and amplifier

A fiber sample of 86 cm with a low index coating was cladding pumped at 976 nm and seeded at 1060 nm. The coupling was performed using a free-space setup and the wavelengths were combined with a dichroic mirror (DMSP1000, Thorlabs). Figure 3.21b shows the signal spectrum after the fiber from the seed alone, the amplified signal, and the laser lines around 1040 nm and 1047 nm, which could be obtained without seeding the fiber and using only the cavity formed by the Fresnel reflection at the fiber ends. For the amplifier configuration, the initial seed and pump powers were set to 740 mW and 17.39 W, respectively, resulting in an output power of 2.644 W and a gain

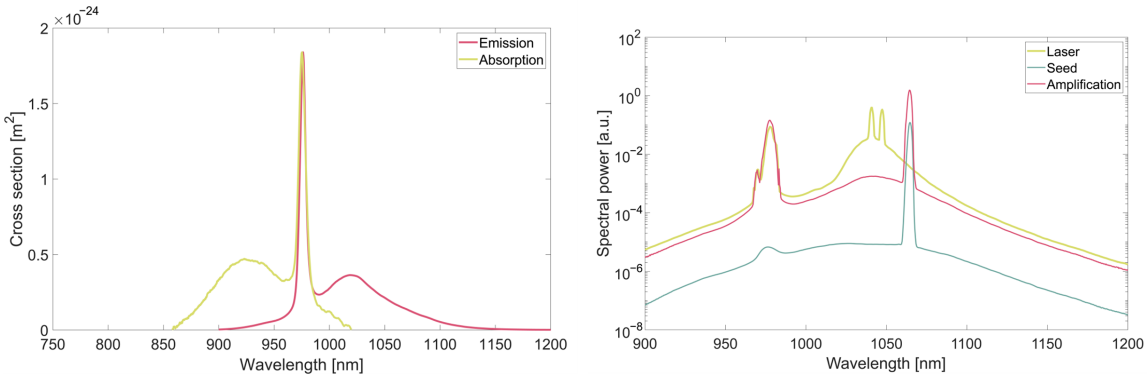

(a) (b)

Figure 3.21: (a) Measured absorption and emission cross sections. (b) Spectra of laser emission (green), amplifier seed (blue), amplifier output (red).

of 5.53 dB (on/off 11.57 dB). At lower seed power, the gain increased to 15 dB around 1060 nm, although a significant ASE background was observed. Note that the length of the fiber was not optimized in these experiments and a significant amount of pump power was left unabsorbed at the fiber end. Nevertheless, the experiments demonstrate the suitability of the fabricated fiber for lasing and amplification applications.

3.3.2 Highly terbium doped fibers

Light propagating through a material exposed to a magnetic field will exhibit a contribution to polarization due to the Lorentz force [160]. Fully polarized light will undergo a continuous rotation of the angle of polarization with distance. Due to the nature of this interaction, the effect is non-reciprocal, i.e. it changes sign when the light propagates in the opposite direction. Its strength is given by the line integral along the path through the medium and looks like this

$$\theta_F = V \int \vec{B} d\vec{l}, \tag{3.1}$$

where θ_F is the angle of rotation, $\vec{B}$ is the magnetic field and $d\vec{l}$ is the direction of propagation and V is the material specific Verdet constant describing the strength of this effect. This property can be exploited to build optical isolators or Faraday mirrors, crucial elements in many optical setups. In an isolator, after passing through the material, the rotation is tuned to $\pi/4$ so that any light reflected back will be at the same angle. The light ends up in orthogonal polarization and can then be output by a polarizer or polarizing beam splitter (PBS). By splitting the reflected light into two polarization components and combining two orthogonal polarization isolators in one package, the isolation can be extended to any angle. The Faraday mirror works on the same principle, except that the entire signal is reflected back through the device. Other applications, such as fiber optic gyroscopes, require a very low Verdet constant, as it can limit the accuracy of the devices [161]. Faraday rotation can also be used the other way around. By measuring the change in polarization angle, the integral in eq.

3.1 can be derived. While this quantity itself is not very useful because it contains the orientation of the medium to the field, it can be reduced to

$$\theta_F = V\mu_0 I, \tag{3.2}$$

by choosing a closed loop geometry and using the Biot-Savart law. We see that by wrapping the material around a current carrying conductor, which is easily done with a fiber, we can measure the current flowing through the loop.

The use of optical fibers as current sensors can be advantageous in harsh environments where corrosion, explosion hazards, or high currents causing interference and lowering accuracy could prohibit the use of electronics [162]. We have developed a range of highly terbium-doped optical fibers with different fabrication methods for current sensing.

Terbium was chosen for its high Verdet constant, which reaches up to $-427.3\,\mathrm{rad\,T^{-1}\,m^{-1}}$ at 633 nm in Tb_2O_3 ceramics. It is also a component of terbium gallium garnet (TGG), commonly used in optical components, which has a Verdet constant for bulk optical materials of $-134\,\mathrm{rad\,T^{-1}\,m^{-1}}$ at 632.8 nm [14]. Since silica has a Verdet constant of opposite sign with $3.13\,\mathrm{rad\,T^{-1}\,m^{-1}}$, doping silica with terbium below a certain concentration will decrease the Verdet constant before increasing it at higher concentrations. Al_2O_3 has been added to improve the solubility of Tb in SiO_2. Its direct effect on the Faraday rotation should be negligible since the Verdet constant of the material is rather low. However, large amounts will replace some of the SiO_2 in the glass and thus remove the contribution from the opposite sign of the Verdet constant of SiO_2. Because of the high aluminium content, the required drawing temperature is increased, and because of the different melting points of the different glass components, they could melt unevenly. Different fractions of Sb have also been added to manipulate the melting point of the glass mixture, which reduces the required furnace temperature during drawing.[163].

3.3.2.1 Drawing methods, composition and attenuation

A variety of fibers were produced with different compositions of aluminium, terbium, and antimony. Not all combinations resulted in flawless fibers. Some turned out to be brittle, showed high scattering, or had bubble formation during fiber drawing.

Figure 3.22 shows the measured attenuation values at 633 nm for different fibers with different concentrations of aluminium, terbium and antimony measured with EDX. Other factors also influence the measured attenuation, such as drawing temperature and speed, precursor purity, as well as oxide grain size distribution and applied vacuum pressure where applicable. Antimony codoping also varies from 0 at.% to 0.19 at.%. However, with the values visualized, we find the highest attenuation at the highest doping concentrations. Increased losses are also present at lower aluminium/terbium ratios.

Comparing the different production methods, the lowest loss is found in the 3LV fibers. Even at elevated doping concentrations of 3.94 at.% terbium, 20.08 at.% aluminium, and some antimony whose concentration is below the EDX detection limit, the loss does not exceed $0.94\,\mathrm{dB\,m^{-1}}$. However, the maximum doping concentration

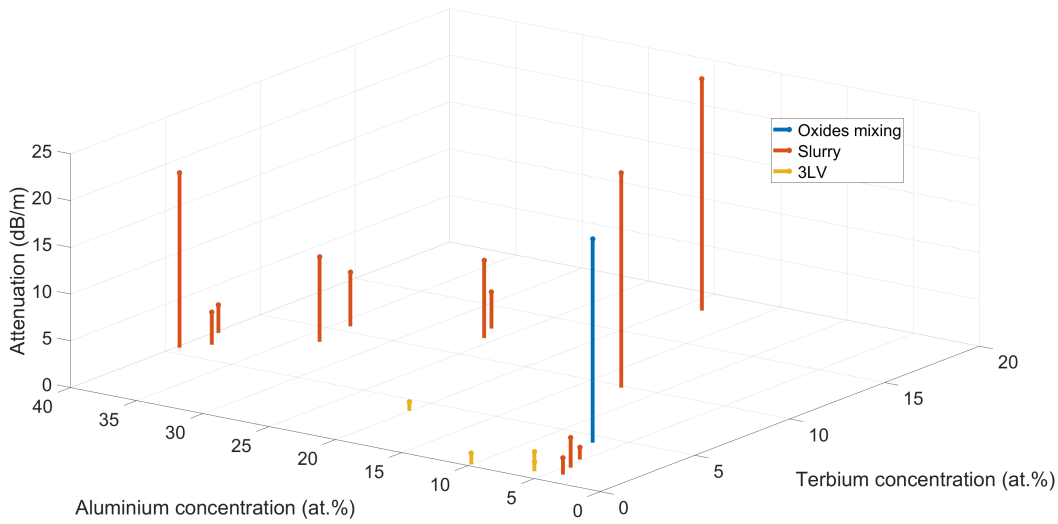

Figure 3.22: Overview of attenuation measurements at 633 nm for fibers with different amounts of aluminium, terbium, and antimony produced by oxide mixing (blue), wet powder doping (slurry), and liquid layer laser vitrification (3LV). The variation of attenuation with antimony is minimal compared to the other components, so its concentration is not visualized.

with this method was limited by the amount of soluble precursor in the sol-gel mixture. Higher amounts would require higher levels of ethanol, which would change the sol-gel chemistry and alter its behavior.

3.3.2.2 Faraday rotation

The fibers with sufficient transmission were tested for their Verdet constant using the setup described in fig. 3.23. The setup consists of a red 658 nm laser diode. Although the diode has a good polarization contrast, a polarizer is added. Then the beam is rotated and coupled into the FUT. The fiber is wound around a conductor to form a closed loop.

After the fiber, the beam is collimated again, polarized, and its intensity is recorded with a photodiode. The setup suffered from back reflections from the fiber facet into the laser diode, causing detrimental interference, so a neutral density filter was added to attenuate the reflections. This came at the expense of signal power, which was offset by increasing the gain of the photodiode. At higher gain, the diode would pick up the magnetic field from the conductor directly, without any light, so it had to be placed at a certain distance.

The conductor is attached to a transformer with a winding ratio of 200 to 1. This is then connected to a variac that is directly connected to the electrical grid. A high current can thus be induced in the conductor, which is limited by rising temperatures that melt the transformer case. Its value is monitored using an electronic current meter (UT-CS09D, UNI-T) as a reference [164]. The rotation of polarization θ is equal to

$$\theta = V \mu_0 I, \tag{3.3}$$

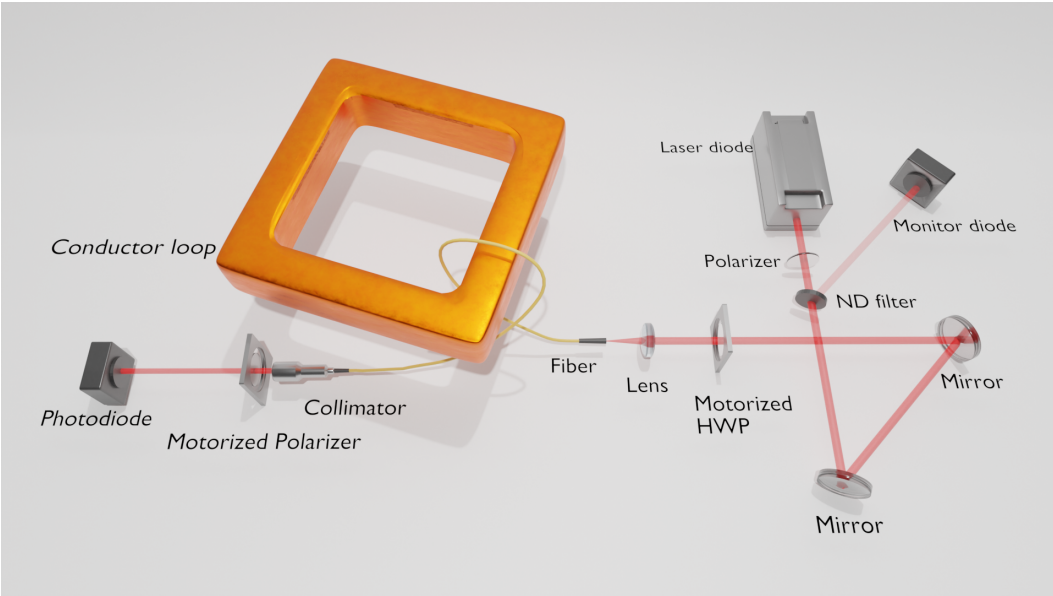

Figure 3.23: Current measurement setup with FUT in a one-loop configuration around a conductor. The source is a 658 nm laser diode.

where V is the material specific Verdet constant and I is the current flowing through the fiber loop. The current is sinusoidally modulated at 50 Hz by the grating. Malus' law for light of a given polarization contrast K passing through a polarizer is

$$\begin{aligned} I &= I_0(cos(\phi)^2 + \frac{1-K}{1+K} sin(\phi)^2), \\ K &= \frac{max(I) - min(I)}{max(I) + min(I)}. \end{aligned} \tag{3.4}$$

ϕ is the angle at which the polarizer is rotated away from the maximum setting. The polarizer setting is then chosen so that the response to any change in polarization is maximal, which is at $\phi = \pi/4$. The power intensity is then given by $I(\pi/4) = I_0/(1+K))$ and the polarizer is set to match this signal. The signal obtained by the setup is then defined by the modulated angle $\phi' = \phi + \theta_F = \phi + V\mu_0 sin(2\pi 50t)$ and is equal to

$$I(\pi/4 + \theta_F) = \frac{I_0}{1+K}(1 + K\theta_F), \tag{3.5}$$

for Faraday rotations within the linear range. We define the time average, which is equal to $I_{DC} = I_0/(1+K)$. We further define the variation on top as I_{AC}. We can then extract θ_F and V from these measurable quantities as

$$\begin{aligned} \theta &= \frac{1}{K}\frac{I_{AC}}{4I_{DC}}, \\ V &= \frac{1}{K}\frac{I_{AC}}{4I_{DC}}\frac{1}{\mu_0 I}. \end{aligned} \tag{3.6}$$

First, the input HWP is set so that the polarization contrast after the fiber is acceptable, since the contrast was found to depend on the input polarization. Then the output polarizer is set accordingly.

3.3.2.3 Measured Verdet constants

The signals obtained ideally follow the sinusoidal current modulation. Figure 3.24 shows the measured signal compared to the current measured by the electronic reference measurement.

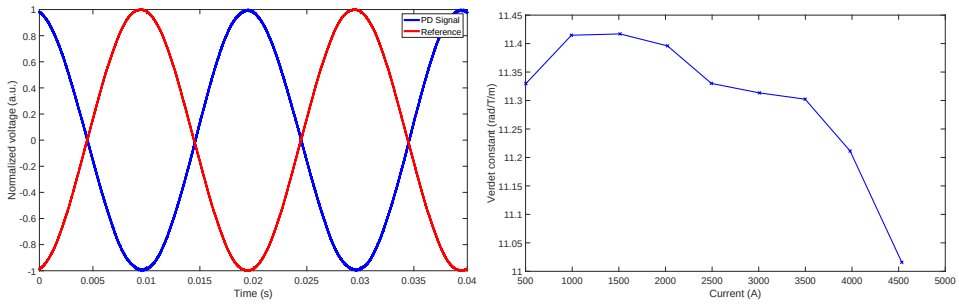

(a) (b)

Figure 3.24: (a) Sinusoidal modulation of the photodiode output voltage (blue) and the output voltage of the electronic reference measurement device. (b) Verdet constant with varying current.

The photodiode signal is centered around a certain offset given by I_{DC} and is modulated as I_{AC}. The signal in fig. 3.24 (a) is centered and normalized. The same is done for the reference measurement of the electronic reference measurement, whose voltage is directly proportional to the applied AC current. The sign of the curve is determined by the winding direction of the fiber loop and the sign of the Verdet constant.

The values obtained are shown in fig. 3.25. For many pieces of fiber, no signal could be generated at all. The results shown here are for selected pieces that showed a response, but choosing another piece of the same fiber or even reassembling the same section could give very different results. Shown are the best values for each fiber. Verdet constants up to 11.2 rad T^{-1} m^{-1} could be obtained for a variety of slurry based fibers. The highest value belongs to a fiber with 7.6 at.% terbium, 39.72 at.% aluminium and 0.13 at.% antimony, while a fiber with 12.89 at.% Tb, 26.68 at.% Al and 0.09 at.% Sb showed a value of 1.77 rad T^{-1} m^{-1} and even lower at 0.6 rad T^{-1} m^{-1} for 18.27 at.% Tb, 18.5 at.% Al and 0.03 at.% Sb. For 3LV produced fibers, no Verdet constant could be determined at all. For reference, some commercially available single mode fibers were also tested and resulted in

Fiber	V (rad T^{-1} m^{-1})
SM400	3.28
SM980	3.30
SM980G80	0.26

Table 3.3: Verdet constants measured on standard single-mode fibers in a single loop configuration

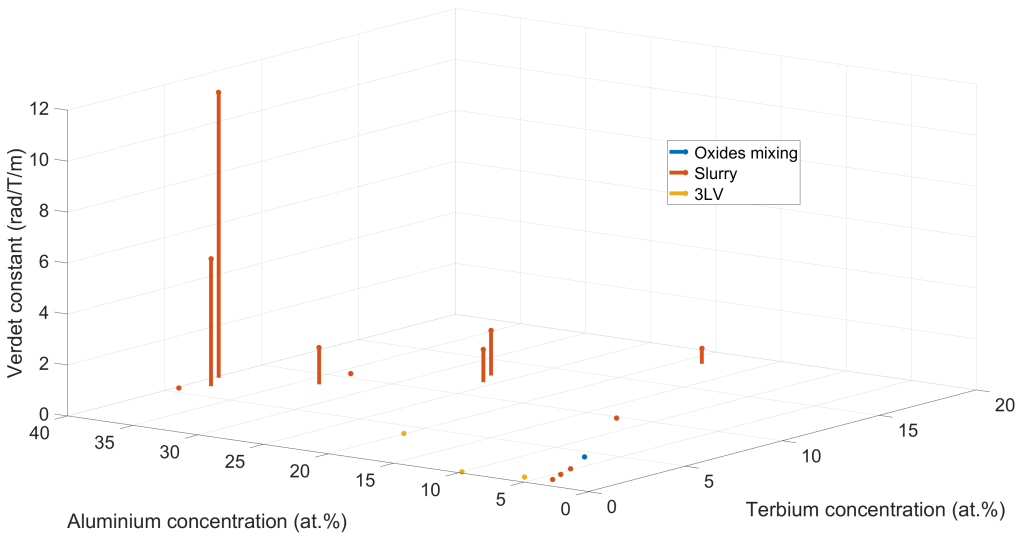

Figure 3.25: Measured Verdet constants for different fiber compositions. The dots indicate failure to obtain a signal.

The SM400 fiber is particularly interesting because its core consists of pure silica [165]. The Verdet constant of silica is given as 3.13 rad T^{-1} m^{-1} at 632.8 nm [166]. This is quite close to the value measured in the fiber. The slightly higher reading could be explained by some of the transmitted light interacting with dopants in the cladding, especially since we are operating the fiber at wavelengths longer than its specified range.

3.3.2.4 Effective Verdet constant

In fact, the Verdet constant of a material is strongly attenuated in the presence of linear birefringence. Some birefringence is randomly generated along a fiber during drawing due to stress gradients. Further bending of a fiber also introduces stress and thus birefringence. In fig. 3.26 we see the polarization contrast after passing light through a bent and a straight fiber. Since a straight slurry-based fiber shows the same contrast variation as the bent fiber, but at different polarization angles, it can be concluded that the bent induced birefringence can somewhat override the draw induced birefringence, but both contributions are significant. Finally, core ellipticity also contributes significantly to the birefringence, which explains why 3LV fibers are

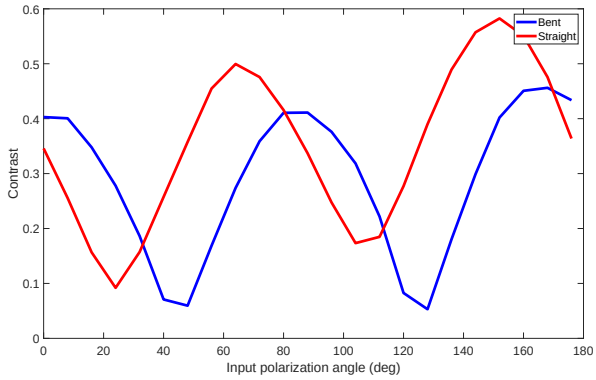

Figure 3.26: Polarization contrast after transmission through a typical slurry-based fiber in a loop (blue) and straight (red) configuration

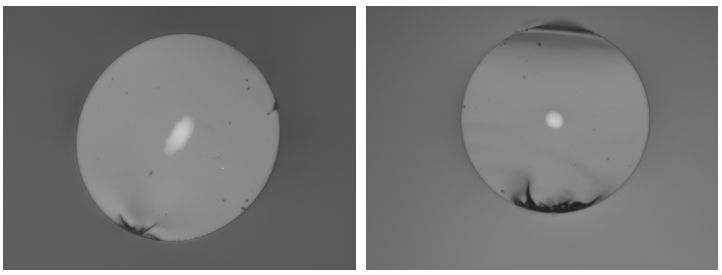

(a) 3LV fiber with significant ellipticity

(b) Slurry based fiber with more round core shape

Figure 3.27: Pictures of the Yb-doped preform and fiber, core illuminated with white light

unable to produce Faraday rotation, since it is difficult to obtain a circular core during preform collapse (see figure 3.27), since the laser heating is not completely symmetric.

As shown in the table 3.3, the measured Verdet constant of the SM400 fiber is equal to the value of the silica, which means that birefringence quenching does not occur. It can be assumed that drawing induced birefringence is minimal in these commercial fibers. This also means that the effect of bending induced birefringence is minimal in this case.

Geometric birefringence caused by core ellipticity is proportional to the ellipticity and the square of the refractive index difference between the core and cladding [167]. Comparing the index differences between the commercial single mode fiber and the best performing fiber above shows that this fiber is 18 times more susceptible to geometrical birefringence. We estimate its index to be 1.52 by an average weighted by the fractional volume of each component [157]. An asymmetric core also causes stress in the fiber, giving another contribution to the birefringence, although it seems to be small, at least in standard non-pm single mode fibers[167]. The third contribution from bend induced birefringence is cubically dependent on the refractive index and proportional to the square of the fiber diameter.

The random nature of the intrinsic birefringence of the fiber, together with the arbitrary bending direction of the fiber in the loop, means that the measured values must

be interpreted as the lower limit of the material-specific Verdet constants. In addition, it is unclear how the guiding dynamics are affected by the multimode structure. Excited modes can change rapidly with coupling, fiber motion, or vibration. Therefore, it is not possible to draw absolute conclusions about the best fiber composition for current measurements. For a better comparison of performance between fibers, single mode geometries would be preferred.

Nevertheless, we fabricated a fiber with high terbium and aluminium concentrations (7.6 at.% Tb, 39.72 at.% Al) and measured a Verdet constant of $11.2\,\mathrm{rad\,T^{-1}\,m^{-1}}$, which is 3× higher than the value in silica.

However, repeating the measurements yielded different results when the fiber was reinstalled in the setup. Other pieces of the same fiber gave no results at all. This shows the large influence of birefringence on the measurement of the Verdet constant. There are steps that can be taken to reduce stress-induced birefringence in coiled fibers. Annealing the fibers at 850 °C for days has been shown to eliminate the stress caused by the bending and drawing process and thus greatly reduce the birefringence.

Geometrical birefringence, on the other hand, is intrinsic to the deformations during fabrication and can only be removed by careful process optimization. A double-pass setup at orthogonal polarizations would eliminate all birefringence effects and allow measurement of the full Verdet constant due to the non-reciprocal nature of the Faraday rotation [161, 162].

In addition, there are fiber designs that eliminate linear birefringence altogether by twisting the fiber at a high rate during drawing, which adds complexity to manufacturing [168, 169].

3.4 Conclusion

We have presented a variety of different fibers made by different methods. A multimode Yb-doped fiber with high aluminium content (60 at.% Al, 1 at.% Yb) was fabricated using wet powder doping and powder-in-tube techniques. As the fiber has demonstrated its ability to produce lasing and gain (see sec. 3.3.1.4), it holds potential for higher power applications due to reduced stimulated Brillouin scattering (SBS) [153] and increased temperature resistance of high concentration alumina glasses, although the losses could be detrimental. The formulation could also be adjusted to allow mid-infrared laser operation by incorporating erbium or dysprosium. The absorbing silica in the core, introduced by diffusion, could possibly be reduced either by adding a buffer between the core and the SiO_2 cladding or by replacing the silica cladding altogether with aluminium-based materials [170].
Terbium-doped fibers for magnetic field or current sensing have been fabricated by the same method. Faraday rotation measurements to determine the Verdet constant yielded a value as high as $V = 11.2\,\mathrm{rad\,T^{-1}\,m^{-1}}$ (7.6 at.% Tb, 39.72 at.% Al), which is 3× higher than silica. Unfortunately, the repeatability was poor. Different sections of the same fiber failed to produce a signal, probably due to the arbitrary combination of intrinsic and bending induced birefringence. All of these fibers have relatively high losses in common.

Much better guiding fibers could be realized by the 3LV method. Unfortunately,

asymmetric collapse during preform fabrication causes significant core ellipticity, which introduces geometric and probably stress-induced birefringence, ultimately suppressing any Faraday rotation. However, the 3LV process has proven excellent for the rapid realization of other fiber concepts. An ytterbium-doped alumina-silicate has been thoroughly characterized and has shown a good slope efficiency of 66 % in a laser application, while all attempts to fabricate laser fibers using the PLV have failed.

The extension of the 3LV to multiple rare earths proved its flexibility. The fiber exhibits fluorescence over an octave bandwidth due to Yb, Er, and Tm incorporated into the glass. The short fabrication time for new rare-earth doped fibers is crucial for optimizing the complex interplay between different ions, as a variety of absorption and emission lines and different cross-excitation possibilities occur. In general, the 3LV has been shown to produce significantly better quality rare earth doped glass than any of the powder-based methods investigated in this work.

The ability to monitor vitrification and adjust its parameters in real time has allowed the incorporation of volatile nanodiamond particles into silica using the PLV method. The survival of these particles was demonstrated in the preform, as their fluorescence could be observed in the core. We have shown significant changes in the n_2 of the core material by the nanodiamonds, as its value in the fiber at 1550 nm was measured significantly higher than in a silica core fiber ($4 \times 10^{-20}\,\mathrm{m^2/W}$ vs. $2.3 \times 10^{-20}\,\mathrm{m^2/W}$), comparing measured pulse broadening with simulations. At 1050 nm, we measured a reduction to $n_2 = 1.9 \times 10^{-20}\,\mathrm{m^2/W}$, both in the fiber, using the same pulse broadening approach, and in the preform, using a z-scan [38].

This shows a high dispersion of the nonlinearity, possibly reaching negative values at shorter wavelengths, while the group velocity dispersion (GVD) was found to be quite similar. This opens the door to truly flexible optimization of the dispersion-nonlinearity landscape by nanodiamond doping, as they can be manipulated independently. Furthermore, the possible negative nonlinearity would essentially double the possibilities for nonlinear optical systems, as the dynamics of one dispersion regime would become available in the opposite regime, such as normal dispersion solitons, as proposed in Bose (2016) [23].

Chapter 4

Low noise supercontinuum generation using a hybrid fiber approach

The following chapter contains work published in the following references:

A. Rampur, D. Spangenberg, B. Sierro, P. Hänzi, M. Klimczak, A. Heidt. "Perspective on the next generation of ultra-low noise fiber supercontinuum sources and their emerging applications in spectroscopy, imaging, and ultrafast photonics". Appl. Phys. Lett. 14 June 2021; 118 (24): 240504.
https://doi.org/10.1063/5.0053436

B. Sierro, P. Hänzi, D. Spangenberg, A. Rampur, and A. Heidt. "Reducing the noise of fiber supercontinuum sources to its limits by exploiting cascaded soliton and wave breaking nonlinear dynamics".
Optica 9, 352-359 (2022)
https://doi.org/10.1364/OPTICA.450505

P. Hänzi, B. Sierro, Z. Liu, V. Romano, A. Rampur, and A. Heidt. "Benefits of cascaded nonlinear dynamics in hybrid fibers for low-noise supercontinuum generation."
Opt. Express 31, 11067-11079 (2023)
https://doi.org/10.1364/OE.481970

4.1 Introduction

As already highlighted in the first pages of this thesis, this chapter showcases the importance of supercontinuum (SC) sources, exhibits the dominant noise mechanisms, focusing on birefringence and different dispersion regimes, and presents a novel low-noise SC source, based on a hybrid-dispersion fiber concept, which separates the nonlinear processes into a pulse compression step in an anomalous dispersion fiber, and the subsequent SC generation step in a highly nonlinear all-normal dispersion (ANDi) fiber.

Supercontinuum (SC) sources in the visible and near-IR have been commercially available for over a decade and are the excitation source of choice for a range of advanced microscopy techniques such as multiphoton and stimulated emission depletion (STED) microscopy [171] or optical resolution photo-acoustic microscopy [172]. In optical coherence tomography (OCT), SC sources facilitate high-speed, high-resolution 3D imaging across several medical specialities, including ophthalmology and cardiology [173], and provide an important diagnostic tool in dermatology for the early stage detection of skin cancer and other skin diseases. Optical spectroscopy and imaging using broadband coherent light sources that cover several molecular absorption bands and spectroscopic regimes have enabled fascinating insights into the world of molecular dynamics, revealing how greenhouse gases interact with pollutant particles or the unexpected complexities of water molecule vibrations [174, 175].

The nonlinear transformation of a narrowband ultrafast laser into a broadband SC in a highly non-linear fiber (HNLF) is often a two-stage process: higher-order soliton compression is followed by additional nonlinear broadening dynamics, whose details depend on the dispersion design of the particular HNLF in use [176]. Typically, a single HNLF is used for SC generation, such that simultaneously satisfying the application demands of maximizing spectral bandwidth and minimizing noise has remained a major challenge, as they often place diametrically opposing constraints on the nonlinear fiber design.

Conventional SC sources employ fiber designs with single zero-dispersion wavelength (ZDW) closely matched to the central wavelength of the pump pulses, which are injected in the region of anomalous group velocity dispersion (GVD) (fig. 4.1(a,top)). The resulting coherent nonlinear dynamics dominated by soliton fission generate large spectral bandwidths but rather complex and highly structured spectral and temporal profiles (fig. 4.1(a,bottom)) that are mostly unsuitable for ultrafast photonics applications.

The predominating noise source during the nonlinear transformation of a narrowband input into a broadband SC spectrum in an optical fiber is the amplification of random quantum fluctuations by incoherent nonlinear effects, which either have a scalar character, such as modulation instability or stimulated Raman scattering [176–178], or a vectorial nature emerging from a coupling of the two orthogonal eigenmodes of the fiber, such as polarization modulation instability (PMI) [179, 180]. The occurrence and strength of these processes depend critically on the dispersion and birefringence engineering of the fiber, as well as on the characteristics of the input pulse. Therefore, a considerable effort has been directed toward identifying fiber designs that favor highly

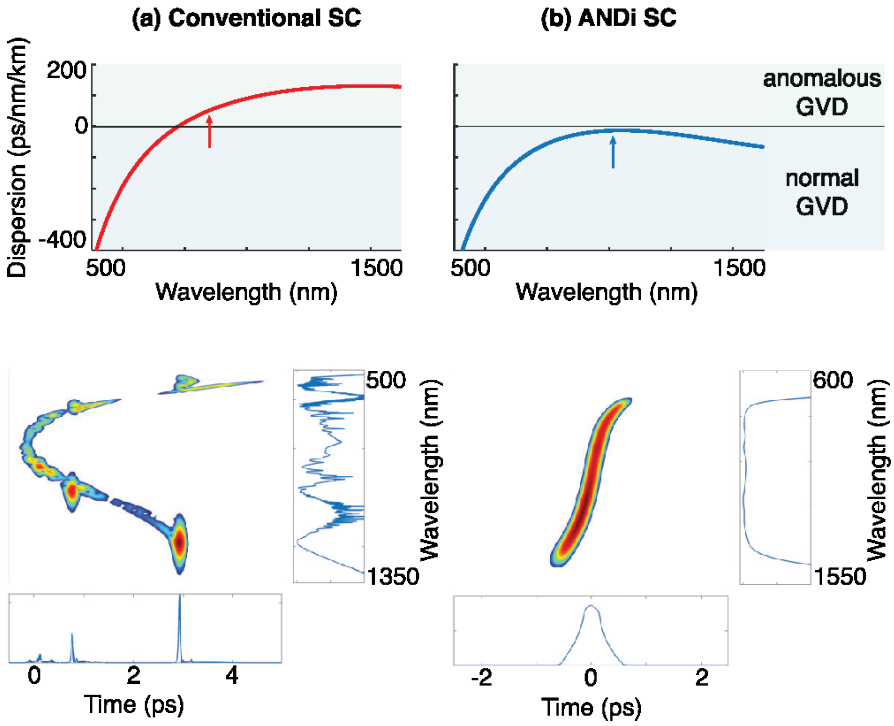

Figure 4.1: Characteristics of SC generation in fibers of different dispersion regimes, pumped with femtosecond pulses. (a,top) anomalous dispersion profile at pump wavelength (arrow). (b,top) all-normal dispersion profile at pump wavelength. (a,bottom) Spectrogram for SC generated in anomalous dispersion fiber and projections. (b,bottom) ANDi spectrogram and projections.

coherent spectral broadening dynamics. Driven by the increased application demand for ultra-low noise broadband coherent light sources, ANDi SC sources have recently attracted attention as a promising alternative to conventional SC sources. Typically, there is a trade-off to be considered when engineering the dispersion landscape of nonlinear fibers.

Generally, SC noise is reduced, and coherence is improved by shorter input pulse durations in any fiber design [22, 176]. Here, anomalous dispersion fibers have a clear advantage as they benefit from an initial stage of soliton compression dynamics, which shorten the injected pulse to a fraction of its initial duration and increase its peak power by up to 1 order of magnitude before the actual spectral broadening dynamics set in [181]. Hence, conventional SC sources require significantly lower input peak power than ANDi SC sources for the generation of equal spectral bandwidths and, consequently, are often the only choice for the nonlinear spectral broadening of lasers with repetition rates of hundreds of megahertz or gigahertz, where the peak power per pulse is limited. Unfortunately, the subsequent soliton fission dynamics produce rather complex spectral and temporal profiles, and the anomalous dispersion environment provides strong amplification for incoherent nonlinear processes.

Recent advances in specialty optical fibers (SOF) design and fabrication have facilitated the emergence of a new generation of highly birefringent, polarization-maintaining (PM) ANDi fibers, which are designed to suppress both scalar and vectorial noise-

amplifying incoherent nonlinear effects under sub-picosecond pumping [21, 22], resulting typically in much smoother spectrograms (fig. 4.1(b,bottom)). The main cause is that the nonlinear dynamics are dominated by optical wave braking (OWB), which is capable of simultaneously delivering low noise, octave-spanning bandwidth, superb spectral flatness, high spectral power densities, and single-cycle temporal waveform support [145]. This new class of SC sources has driven recent advancements of the state-of-the-art in several applications, which so far were either not able to use or were limited by conventional fiber SC sources due to their noise or complex spectra and pulse shapes, e.g., in hyperspectral and multimodal imaging, near-field optical microscopy, optical coherence tomography at the shot-noise limit, and ultrafast photonics [182–189].

Nevertheless, even in the ANDi regime, the noise and temporal properties of SC sources are becoming increasingly limiting factors, which are closely linked to the design of the nonlinear fiber used to achieve spectral broadening. In this work, we investigate optimal fiber properties for low-noise SC generation, regarding geometrical cross section, birefringence and dispersion. The result is a novel fiber noise fingerprint technique, which measures the noise in SC generation in dependence of polarization angle. This leads to a pattern, that is unique for each fiber and can be used to identify noise contributions from polarization effects such as PMI. Finally, the benefits of different fiber designs are combined in a hybrid fiber approach for ultra-low noise SC generation, which splits the nonlinear dynamics into two discrete fibers, both individually optimized for each stage.

Inspired by early works with dispersion-flattened and dispersion-decreasing fibers [190, 191], in this work, we separate the different nonlinear dynamics, i.e., soliton compression and OWB into different fiber sections. We utilize an anomalous dispersion fiber with optimized length for optimal pulse compression with nonlinear broadening in different HNLF with different dispersion properties. We show that this hybrid fiber approach is reducing relative intensity noise (RIN) in all dispersion regimes, while leading to much increased broadening in the ANDi fiber. The hybrid ANDi approach proves to be the one producing the lowest RIN at comparably large bandwidths. With this reason we investigate the hybrid ANDi fiber more closely in simulations, leading to improved performance. Crucially, we identify PMI as the main noise contribution in the stand-alone ANDi fiber, revealing a noise suppression mechanism in the hybrid fiber based on the reduced length scale of the OWB dynamics outpacing the incoherent PMI.

4.2 Noise fingerprints of highly non-linear fibers and contributing mechanisms

The noise properties of SC sources can be understood in terms of a competition between coherent and incoherent nonlinear processes. A low-noise and phase-coherent SC can be generated in the normal dispersion regime under a wide range of conditions when self-phase modulation (SPM) and OWB dominate [22], or in the anomalous dispersion regime when soliton fission dominates, i.e., using pump pulses with very short durations

and low soliton numbers. However, these coherent dynamics can be disturbed by incoherent nonlinear effects, which can build up new spectral components from quantum noise and whose influence grows with longer pump pulse durations [176].

Examples of this noise amplification are illustrated in fig.4.2, showing SC generated by (a) four-wave mixing (FWM)-induced modulation instability (MI) and (b) stimulated Raman scattering (SRS). Both nonlinear effects generate gain bands spectrally separated from the input pulse spectrum, providing enormous exponential gain to any seed signal injected into these bands.

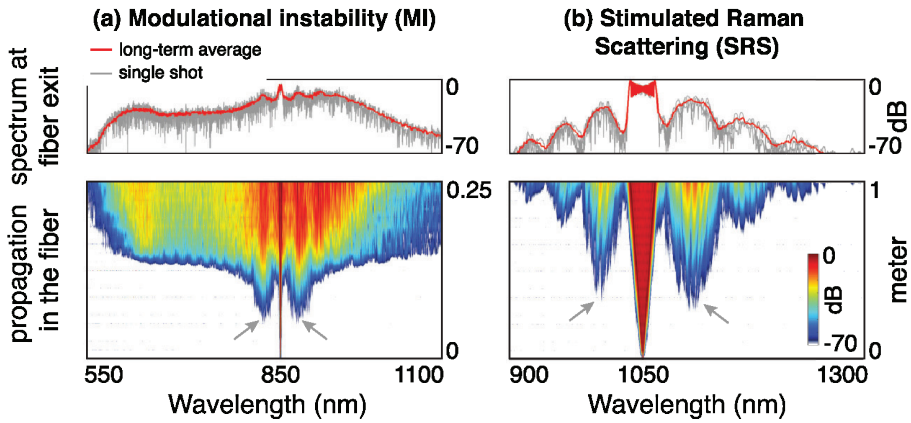

Figure 4.2: Quantum noise seeded gain mechanisms. (a) Modulational Instability in ANDi fiber. (b) Stimulated Raman Scattering in anomalous dispersion fiber. Both processes were simulated for 5 ps pulse width and 5kW peak power. Gray arrows are indicating the strongest noise amplification events.

When this gain remains unseeded, as in these examples, then random quantum fluctuations serve as the seed and are amplified to become significant and eventually dominate the nonlinear dynamics. The noise-seeded spectral components contained in the MI and SRS peaks exhibit random fluctuations in the amplitude and phase from shot to shot and are thus incoherent with the pump. With further propagation, cascaded Stokes (redshifted) and anti-Stokes (blueshifted) gain bands emerge and eventually distribute noise throughout the SC pulse. Similar noise amplifying nonlinear effects exist when coherent and incoherent mode coupling between the two principal polarization axes of a fiber is considered.

4.2.1 Noise control by dispersion engineering

Under the necessary conditions for SC generation, low dispersion and high low nonlinearity, a nonlinear coupling of SRS and FWM occurs [192]. In a single-mode fiber, the interaction between these two nonlinear processes can be described by the mixed parametric Raman (MPR) gain [177]. It is given by

$$g_{MPR} = 2\gamma Re\left(\sqrt{K(2q-K)}\right), \tag{4.1}$$

where $K = -\beta_2\Omega_R^2/(2\gamma P_0)$ describes the ratio of chromatic dispersion and nonlinearity, with the fiber dispersion coefficient β_2 and the nonlinearity parameter γ, the peak

angular frequency shift of the Raman gain Ω_R, and the pulse peak power P_0. The factor $q = (1 - f_R) - f_r \chi^{(3)} \Omega_R$ contains the Raman susceptibility $\chi_R^{(3)}$ and a fractional contribution f_r (0.18 for silica) of the Raman effect to the total nonlinear response of the fiber material. Fig.4.3 shows g_{MPR} for a silica fiber as a function of K, normalized to the standard Raman gain coefficient $g_R \approx \gamma/2$.

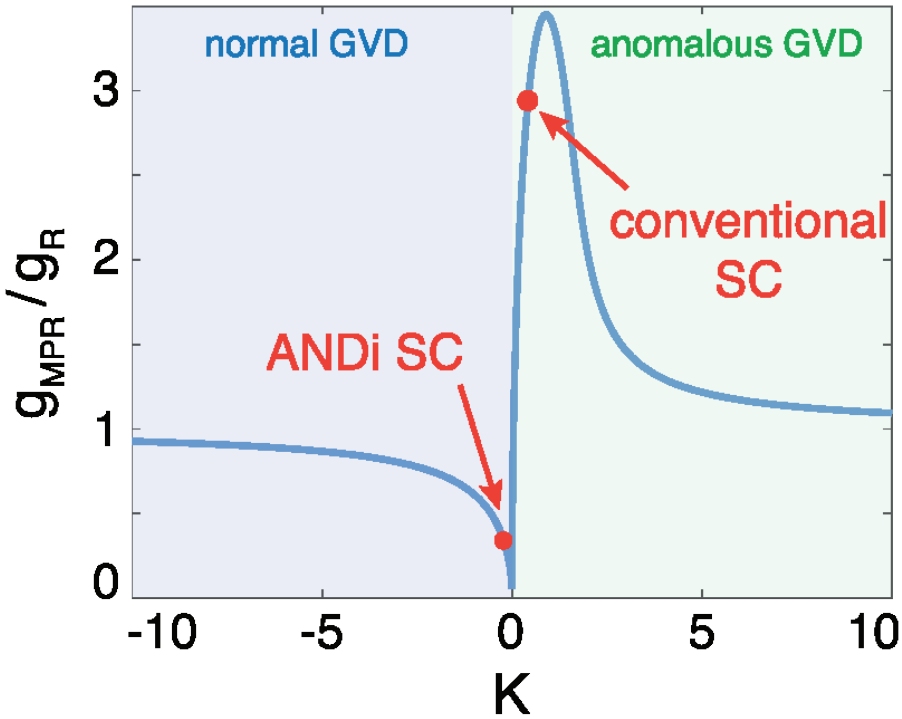

Figure 4.3: Mixed parametric Raman gain normalized by the standard Raman gain. The region of normal dispersion is shaded blue, the region of anomalous dispersion green. Highlighted in red are the points in the curve corresponding to the simulations above.

Eq. 4.1 describes an explicit dependence of the MPR gain on chromatic dispersion and nonlinearity, and its validity in nonlinear fibers has been experimentally verified [190, 193]. However, so far its implications for the control of nonlinear noise amplification by engineering the fiber dispersion profile have not been fully realized. While recent work has shown the important role of the MPR gain for the noise properties of ANDi SC [194], we believe that it can in fact be applied more universally to explain the observed noise properties of SC generated in both dispersion regimes.

In fig. 4.3, mainly the region $|K| < 1$ is relevant to SC generation, where we observe a strong suppression of the MPR gain in normal dispersion, while MPR-induced noise-amplification is strongly amplified in the anomalous dispersion region. The peak of the MPR gain is located at $K \approx 1 - f_r/2$, where Stokes and anti-Stokes Raman sidebands are effectively amplified by MI, whose role in the coherence collapse of conventional SC has been investigated since the early days of fiber-based SC generation [195, 196]. When we consider the typical conditions for octave-spanning SC generation, we find that the MPR gain and associated noise amplification can be decreased by over one order of magnitude by changing from the conventional to the ANDi fiber design. In

fact, this order of magnitude difference in noise susceptibility is a recurrent factor found in many theoretical and experimental studies, as we detail below, and can be seen as the main reason behind the attraction of ANDi fibers for the low-noise SC source development.

The competition between the coherent and incoherent dynamics typically leads to a threshold pulse duration T_{crit} or threshold soliton number N_{crit} above which the nature of the SC changes from coherent to incoherent [176, 197]. The ANDi fiber design exhibits about 10× higher T_{crit} and 50× higher N_{crit} than its conventional counterparts for octave spanning bandwidths. The superior coherence and noise properties of ANDi SC over conventional SC were verified, for example, by measurements of RIN, spectral coherence, dispersive Fourier transformation, and RF beating with stabilized laser diodes [180, 198, 199].

ANDi SC also possess a remarkable resistance against technical pump laser fluctuations [200–202], while conventional SC amplify such fluctuations by up to 20 dB, even in the regime where coherent dynamics dominate [203]. Describing incoherent nonlinear dynamics in terms of the MPR gain is therefore a successful concept for explaining the superior stability of ANDi SC. It also provides a new perspective on the considerable potential for noise control in nonlinear fiber optics.

A future challenge will therefore lie in the development of new fiber designs specifically tailored for low-noise operation in a variety of nonlinear frequency conversion applications.

4.2.2 Noise control by designing fiber geometry and birefringence

Every fiber exhibits a certain amount of birefringence that breaks the degeneracy of polarization modes. Birefringence might be induced unintentionally by unavoidable external stresses or bending of the fiber, or it can be engineered, e.g., by including stress rods or asymmetries into the design of the fiber cross-sectional geometry. The coherent and incoherent coupling of the fiber's polarization modes leads to several nonlinear effects that, in addition to the MPR gain, have the potential to amplify quantum noise and result in unpredictable fluctuations of the polarization state. In the context of ANDi SC sources especially relevant are PMI [189, 204], cross-phase modulation instability (XMI) [205, 206], and Raman amplification assisted by cross-phase modulation [139, 207].

In general, the occurrence of noise amplification is a complex function of fiber birefringence and dispersion, as well as a relative orientation of input pulse polarization and fiber axes. In fig. 4.4, we present preliminary results of high-resolution polarization-dependent RIN measurements visualizing this complexity. For these measurements, pulses from an ultrafast Er:fiber laser (80 fs, 40 MHz, 0.05 % RIN) were coupled into SC fibers with similar dispersion profiles, but very different geometries and birefringence, generating SC with comparable spectral bandwidths in the range of $1.2-2.2\,\mu$m. A rotating half-wave plate in front of the fiber and a synchronized analyzer at the fiber exit control the plane of pump pulse and detection polarization with respect to the fiber geometry. Polarization-dependent RIN values are measured with an angular resolution

of approximately 0.2 deg using a photodiode and an electronic spectrum analyzer and visualized in polar plots. These plots were found to be unique for each tested fiber and are therefore referred to as “noise fingerprints”.

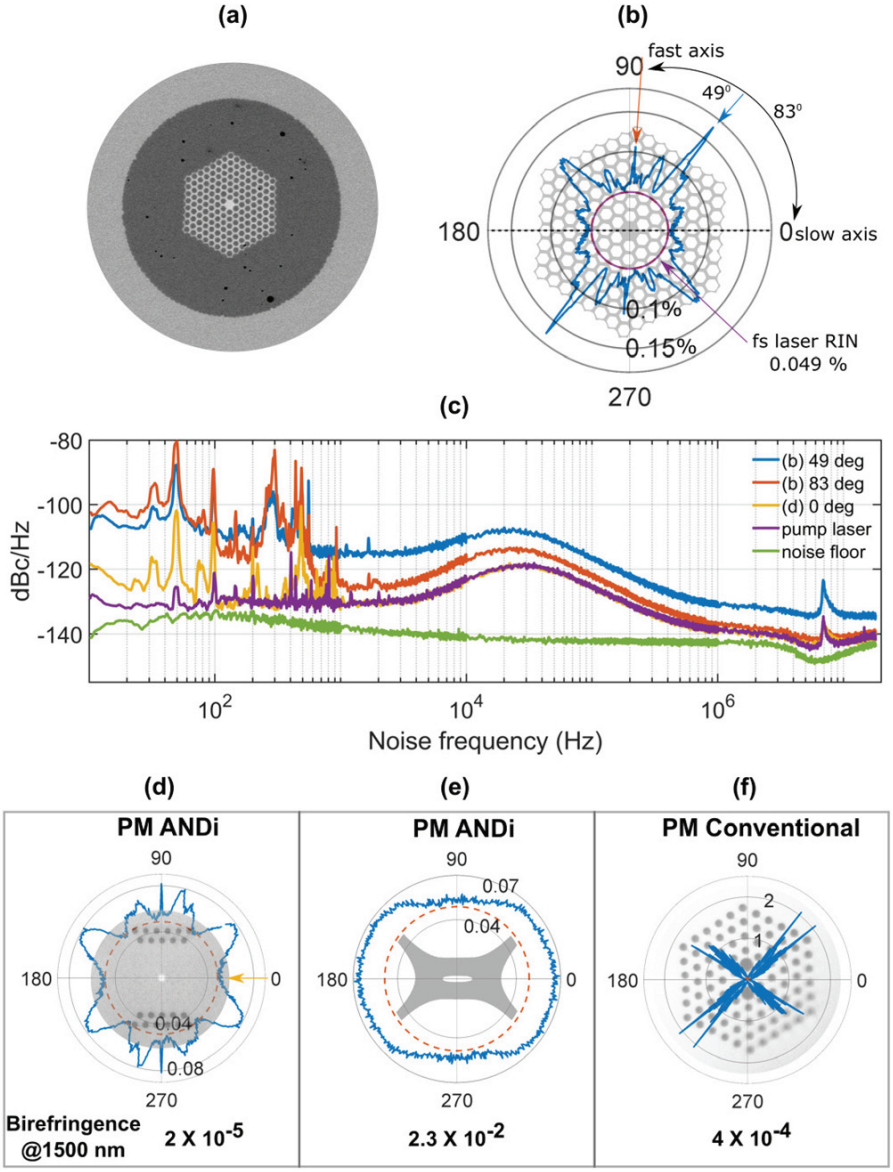

Figure 4.4: Noise fingerprints of SC generated in different fibers using a femtosecond Er fiber laser (80 fs, 40 MHz, 1550 nm) measured from 10 Hz – 20 MHz. (a) Low birefringent ANDi-PCF cross section [208]. (b) RIN values with changing pump polarization angle on top of fiber geometry. Red circle shows Pump RIN. (c) Noise PSD for (blue) polarization in between slow and fast axis (49 deg), polarization aligned to fast axis (red,83 deg) and polarization aligned to slow axis (yellow, 0 deg, pump RIN (purple) and noise floor (green). (d) Airhole PM ANDi photonic crystal fiber (PCF) [209]. (e) Suspended core ANDi [197]. (f) anomalous PM-1550-01, NKT.

These measurements reveal a strong correlation between the nonlinear noise amplification and the cross-sectional geometry of a particular fiber, which we attribute to the

unique stress profile associated with each fiber structure and its drawing conditions. The ANDi fiber in fig. 4.4(a) and fig. 4.4(b) is designed as an all-solid microstructured PCF made from two different soft glasses forming the photonic lattice and inclusions. The structure causes a complex stress pattern due to different thermal expansion coefficients of the two glasses. Since there is no intentional stress axis defined in this design, the resulting birefringence is random and the polarization axes are not well defined, evident by the 83 deg angle measured between the axes. The complex stress profile is also reflected in the highly polarization-dependent nonlinear noise amplification pattern, which we found to be highly susceptible to environmental disturbances such as bending the fiber, different clamping conditions, or day-to-day temperature changes.

Since for each angular RIN measurement a full noise spectrum is available, we can identify the underlying noise amplification process for every feature of the fingerprint by analyzing its characteristic noise frequencies (fig. 4.4). For example, at 49 deg the noise spectrum of the SC is shifted upward in comparison to the pump laser due to a significant contribution of excess white noise, which is a characteristic signature of quantum noise amplification, and can therefore be attributed to the occurrence of XMI and PMI. Near the fast axis, on the other hand, we mainly observe low-frequency noise, which indicates polarization instability caused by the cancellation of the small linear fiber birefringence by the nonlinear Kerr effect. In general, we observe a complex superposition of these effects.

Figure 4.4 (a)-(f) also illustrates that birefringence is an effective control parameter to reduce polarization-dependent noise in ANDi SC generation. With increasing birefringence, the noise fingerprints become more regular and environmentally stable, as shown for the air hole microstructured silica PCF with germanium-doped core in fig. 4.4(d). Near the slow axis (0 deg) of this fiber, the noise spectrum is virtually identical to the noise of the pump laser (fig. 4.4(c)), while we continue to observe a strong correlation of noise features and fiber geometry for off-axis pumping. Eventually, we observe complete suppression of noise-amplifying nonlinear processes for extremely birefringent ANDi fiber designs, such as the nanohole suspended core fiber in fig. 4.4(e), even when the pump polarization is not aligned to one of the principal fiber axes.

In contrast, the noise fingerprint of a comparable polarization-maintaining conventional SC source (fig. 4.4(f)) is significantly more complex and shows noise amplification up to a factor of 40. In the test conditions, the soliton number is $N = 6$, such that a stable SC is generated when the polarization of the pump pulses is exactly aligned to a principal axis of the fiber. However, even slight misalignment of the polarization on the order of just 1 deg causes a significant rise of the SC noise.

These measurements highlight the importance of the cross-sectional fiber geometry and the homogeneity of the stress profile, in addition to dispersion engineering, for the realization of high-quality, low-noise SC sources. ANDi SC sources designed with these considerations in mind are currently emerging also for other pump wavelengths, providing further experimental evidence for the excellent quality and stability of these broadband coherent light sources [210].

4.3 Supercontinuum generation by separating nonlinearities in hybrid fibers

So far we have highlighted the necessity of birefringent fibers to suppress noise from polarization effects, such as PMI and XMI. Additionally, ANDi fibers offer clear advantages in terms of quantum noise amplification, however at the disadvantage of requiring higher input powers than anomalous dispersion fibers. In the next section we utilize a hybrid fiber approach to compress the initial pulse separately in an anomalous single mode fiber (SMF) using soliton self-compression before the broadening stage in a HNLF, effectively separating the nonlinear mechanisms.

We first present a hybrid fiber based on an ANDi fiber, benefitting from soliton self-compression, followed by OWB, resulting in an ultra-low noise and highly coherent fiber SC source covering the $930-2130\,\mathrm{nm}$ range with a spectrally resolved RIN as low as $0.05\,\%$ and averaging $0.1\,\%$ over a bandwidth of $750\,\mathrm{nm}$. Due to a short falling of the scalar generalized nonlinear Schrödinger equation (GNLSE) to accurately replicate the noise at the center wavelengths occurring in the stand-alone ANDi fiber, we then identify incoherent polarization effects such as PMI and XMI as the sources responsible for the remaining noise. This finding is backed by simulations illustrating the corresponding gain bands using a vectorial GNLSE.

Further, the coherence of the ANDi SC is measured at a very high average value of 0.96 over a broad range. Finally, we extend the treatment to other HNLF and show that the hybrid approach is beneficial to fibers of all dispersion regimes in terms of noise. ANDi fibers benefit the most in terms of spectral broadening. By direct comparison, hybrid fiber ANDi SC proves to be the superior platform for low-noise broadband SC generation. The basic scheme is illustrated in fig. 4.5.

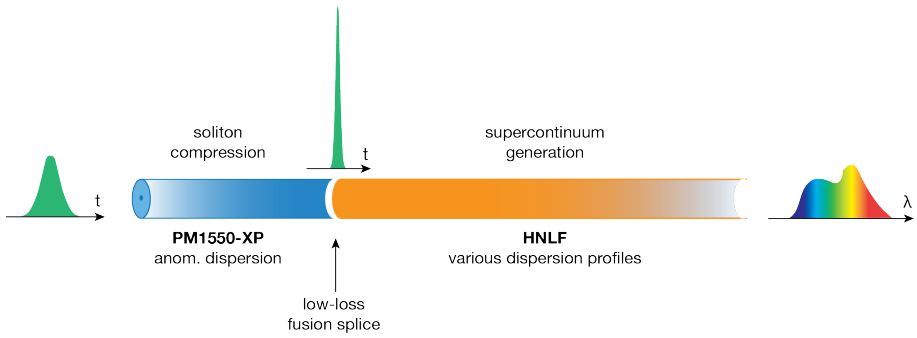

Figure 4.5: Hybrid fiber concept. The hybrid version of a particular HNLF consists of a short piece of single mode fiber (here: PM1550-XP), exhibiting anomalous dispersion at the pump wavelength, fusion spliced to the input side of the HNLF. This induces cascaded nonlinear dynamics, where in the first section nonlinear soliton compression shortens the duration and increases the peak power of the input pulse, while in the subsequent HNLF section a broadband SC spectrum is generated by nonlinear dynamics that depend on the dispersion profile of the particular HNLF.

4.3.1 Hybrid approach using all-normal dispersion highly nonlinear fiber

The source is based on a standard ultrafast Er:fiber laser seeding cascaded nonlinear dynamics in two discrete, widely available commercial PM step-index fibers. The individual fibers exhibit anomalous and all-normal chromatic dispersion at the pump wavelength, respectively, and are joined together by a low-loss fusion splice to form a hybrid fiber.

We show that this hybrid approach not only doubles the generated spectral bandwidth but also decreases the RIN by up to 1 order of magnitude compared to direct pumping of the individual fibers. While our measurements reveal that PMI instabilities set a lower limit to the RIN of the directly pumped ANDi SC source, we identify a novel noise suppression mechanism in the hybrid fiber such that the SC noise approaches the theoretical limit determined by the noise and pulse shape of the pump laser.

The fibers used in this work are two commercial PM step-index fibers produced by Coherent-Nufern, namely PM1550-XP and PM2000D (HNLF-ANDi from now on), which exhibit anomalous and all-normal chromatic dispersion at the pump wavelength of 1560 nm, respectively, as shown in fig. 4.6 [211]. PM1550-XP has a core-diameter of

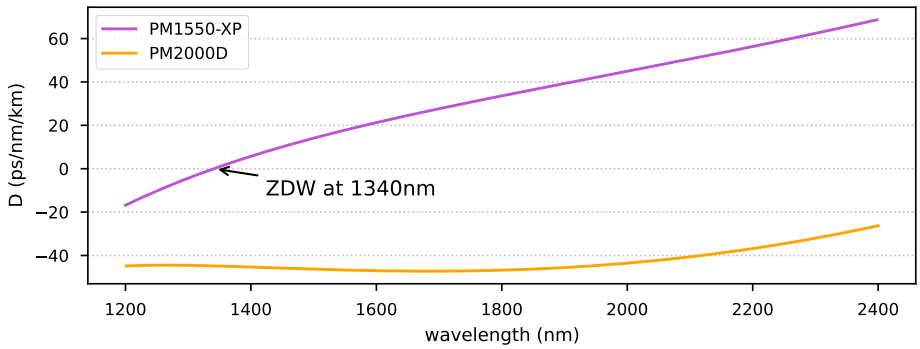

Figure 4.6: Measured chromatic dispersion profiles of PM1550-XP and PM2000D (HNLF-ANDi) fibers used to form the hybrid fiber in this study.

8.5 µm and numerical aperture (NA) of 0.125, resulting in a zero-dispersion wavelength of 1.34 µm and dispersion parameter $D = 18\,\mathrm{ps/(nm\,km)}$ at 1560 nm. In contrast, the small 2.1 µm diameter core, high NA of 0.37, and highly Germanium (Ge)-doped core material composition of HNLF-ANDi were specifically designed to exhibit flat and normal dispersion over the entire near-IR spectral region, with $D = -46\,\mathrm{ps/(nm\,km)}$ at 1560 nm. Both fibers are PANDA-type PM fibers, with birefringence values at the pump wavelength of 3×10^{-4} given by the manufacturer for PM1550-XP, and 2×10^{-5} measured in-house for HNLF-ANDi.

In order to exploit cascaded nonlinear dynamics in both fibers, a low-loss fusion splice is an essential requirement, but due to the large core diameter and NA mismatch losses in the order of 4 dB are to be expected when using a standard splicing recipe. Better results can be obtained with the thermally expanding core (TEC) technique [212]. Owing to the high Ge content of the HNLF-ANDi core material, long arc duration leads to thermal diffusion of Ge from the core to the cladding region, which gradually

increases the mode field diameter in the hot zone and thus reduces the splice loss. By monitoring the transmission of a 1550 nm continuous-wave laser in real-time during the splice, we reach a minimum splice loss of 0.7 dB (85 % transmission) with an arc time of 14 s. The splice is executed simply by modifying the arc duration of the standard PM single-mode program of a Fujikura FSM45+ fusion splicer and using auto-alignment of the polarization axes.

4.3.1.1 Soliton pre-compression

After the splice, the hybrid fiber is cleaved such that it consists of a 6.2 cm length of PM1550-XP at the input followed by 20 cm of HNLF-ANDi, where in the former soliton compression and in the latter optical wave-breaking dynamics are exploited. Hence, the length of PM1550-XP is of particular importance in our approach and was carefully optimized using the numerical pulse propagation simulations and experimental time-domain ptychography (TDP) measurements summarized in fig. 4.7 [146, 213].

In the fiber, the 110 fs, 32 kW, 40 MHz input pulse supplied by the Er:fiber laser

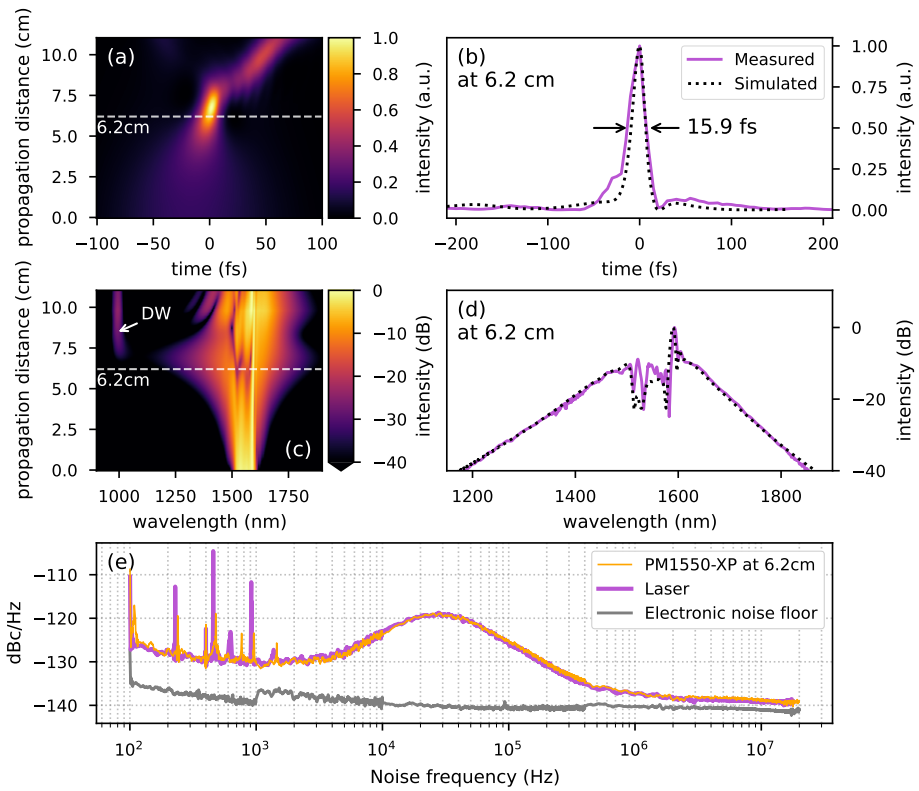

Figure 4.7: Soliton compression in the PM1550-XP fiber pumped with 110 fs, 32 kW input pulses. (a) Simulated temporal intensity profile as function of propagation distance. (b) Simulated (dashed) and measured (solid) pulse shape at 6.2 cm. The measured pulse is recorded after propagating through dispersive elements (thin lens and half-wave plate) and therefore slightly longer (20.6 fs). (c) Simulated spectral evolution; DW: dispersive wave. (d) Simulated (dotted) and measured (solid) spectra at 6.2 cm. (e) Frequency resolved noise measurements of the injected pump and the compressed soliton pulse trains.

forms a soliton of order $N = 4.3$ that temporally compresses until soliton fission around 6.5 cm breaks it up into its fundamental constituents. The optimized fiber length is chosen such that the resulting pulse is as short as possible while avoiding soliton fission. Fig. 4.7 (b) and (d) show the simulated compressed pulse with 15.9 fs full width at half maximum (FWHM) and the corresponding spectrum, respectively, using the final fiber length of 6.2 cm.

Both results are in excellent agreement with the experimental TDP measurements done using a separately prepared PM1550-XP fiber of equal length. The input pulses are therefore compressed by a factor of 7 while the peak power increases by a factor of about 5.3 to 170 kW, with the remaining energy distributed in a low-level pedestal typical of soliton compression. We also note that increasing the fiber length beyond the point of soliton fission does not significantly increase the spectral bandwidth in this case, as shown in fig. 4.7 (c), apart from the formation of a dispersive wave (DW) around 1 µm wavelength.

4.3.1.2 Experimental setup and RIN measurement

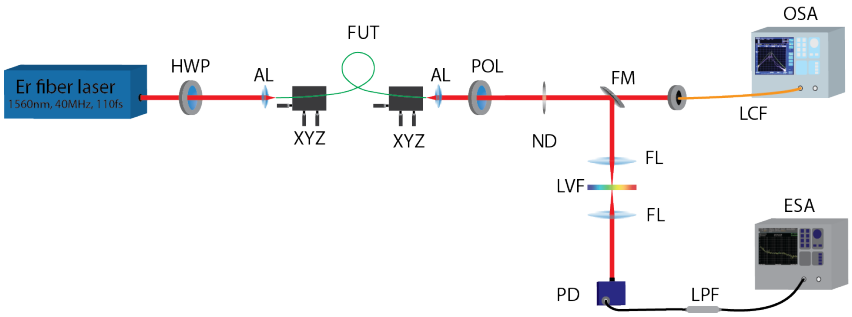

Figure 4.8: Schematic setup for supercontinuum generation and RIN measurement. HWP: half wave plate; AL: aspheric lens; XYZ: three axis translation stage; FUT: fiber under test; POL: polarizer; ND: neutral density filter; FM: flip mirror; LCF: large core fiber patch cord; OSA: optical spectrum analyzer; FL: focusing lens; LVF: linear variable filter $1.3 - 2.6$ µm; PD: photo diode; LPF: low pass filter (< 21 MHz); ESA: electronic spectrum analyzer.

The experimental setup used to generate and analyze the SC is shown in fig. 4.8. An ultrafast Er:fiber laser (Toptica FemtoFiber pro) centered at 1560 nm delivers a 90 fs pump pulse train with 40 MHz repetition rate, RIN of 0.05% (measured in the frequency range 100 Hz – 20 MHz), and polarization extinction ratio (PER) of 30 dB. A half-wave plate is used to align the polarization state of the input pulses to the fiber's principal birefringence axes. The pump pulses are coupled into the fiber under test (FUT) by an aspheric lens with focal length chosen to match the mode field diameter of the fiber, resulting in a maximum coupled average power of 210 mW. This corresponds to a peak power of 33 kW, calculated using the real pulse shape emitted by the laser measured by time-domain ptychography [213]. The generated SC spectra are recorded using two optical spectrum analyzer (OSA) (Yokogawa AQ6370 for $\lambda < 1700$ nm and AQ6375 for $\lambda > 1700$ nm). A polarizer is inserted in the beam path in order to analyze the PER

of the SC, and also serves for converting possible polarization state fluctuations into amplitude noise that can be detected using the subsequent RIN measurement system.

Our RIN measurements are based on low-bandwidth photodetection of the pulse train and measurement of the noise power spectral density (PSD) at baseband frequencies in the range from 100 Hz up to the Nyquist frequency of 20 MHz, corresponding to half of the repetition rate f_{rep} of the pulse train. The limitation of the measurement bandwidth to the baseband (frequencies between 0 and $f_{rep}/2$) is an essential requirement for accurate intensity noise measurements, as is well documented in literature [214, 215].

In order to measure the spectrally resolved RIN, the SC pulse train is first passed through a linear variable bandpass filter with 20 nm bandwidth covering the range 1300 − 2600 nm (Vortex Optical Coatings, UK) and detected with a low-bandwidth amplified photodiode (Thorlabs PDA10D2, bandwidth DC - 25 MHz, 900 − 2600 nm spectral range, 5 kV/A transimpedence gain) connected to an electronic spectrum analyzer (ESA) (Signal Hound USB-SA44B, bandwidth 1 Hz − 4.4 GHz). Additional discrete bandpass filters with similar bandwidths cover the shorter wavelengths below 1300 nm. For each spectral position, the DC level of the voltage signal (V_0) and the voltage noise PSD $S_V(f)$ [V^2/Hz] are measured with a voltmeter and the ESA, respectively. For the PSD measurement the photodiode signal is filtered by a 21 MHz filter to avoid saturation of the ESA at the pulse repetition rate as well as a DC block capacitor with cut-off frequency < 3 Hz to protect the ESA from harmful DC voltage. The RIN PSD can then be obtained by $S_{\mathrm{RIN}}(f) = S_V(f)/V_0^2$ (1 Hz^{-1} or dB$_c$ in logarithmic presentation] because the measured voltage V is proportional to the optical power P. The root mean square (RMS) RIN in percent is then given by the square root of $S_{RIN}(f)$ integrated from 100 Hz up to the Nyquist frequency of 20 MHz. This value is used in this manuscript when integrated RIN values are referenced.

Fig. 4.7 (e) shows that the noise power spectra of the soliton-compressed pulses and the driving Er:fiber are indistinguishable, the integrated RIN is 0.06 % in both

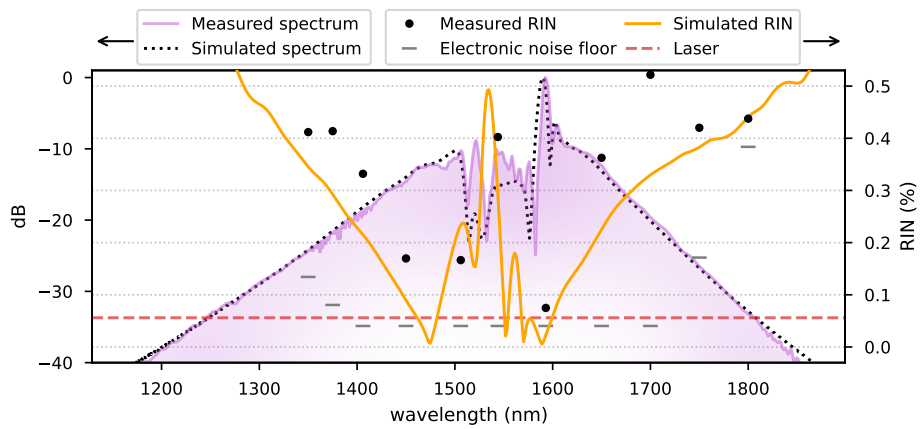

Figure 4.9: Spectrum and spectrally resolved RIN of the soliton-compressed 16 fs pulse train. Left scale: measured (solid red) and simulated (dotted) spectra; right scale: spectrally resolved measured RIN (dots) with corresponding noise floor (-), simulated RIN (solid yellow) computed with eq. 4.2; the RIN of the pump laser is indicated by a red-dashed line.

cases. Hence, the substantial temporal compression and peak power amplification is obtained without incurring any noise penalty.

The broad peak in the noise spectrum at mid-range frequencies between $10-100\,\mathrm{kHz}$ stems from intracavity dynamics of the Er:fiber oscillator, while the sharp peaks at low frequencies can be traced to power supplies as well as vibrationally and acoustically induced noise from the laboratory environment, which can slightly change between measurements. We note that spectrally resolved RIN measurements of the soliton-compressed pulses reveal locally increased RIN up to $0.52\,\%$, see fig. 4.9, but this is less relevant for our purposes since spectral filtering also modifies the temporal characteristics of the pulse.

4.3.1.3 Hybrid ANDi fiber

In the normal dispersion regime provided by the ANDi fiber, the initial nonlinear spectral broadening dynamics are dominated by SPM followed by OWB redistributing energy from the spectral center to the wings and smoothing the spectrum [145]. Both processes are known to provide low-noise and coherent broadening of the input pulse spectrum for our pump pulse parameters [22]. The fiber length over which these dynamics occur depends on duration T_0 and peak power P_0 of the injected pulse, $L_{OWB} \propto T_0/\sqrt{P_0}$, while the obtainable spectral bandwidth is independent of T_0 but scales approximately with $\sqrt{P_0}$ [145]. Since the pre-compressed soliton enters the ANDi fiber with much shorter pulse duration and higher peak power than the original pulse supplied by the Er:fiber laser, we expect faster nonlinear dynamics and broader SC bandwidth generated in the hybrid fiber when compared to the directly pumped, stand-alone ANDi fiber.

Fig. 4.10 compares the measured SC spectra generated in the hybrid fiber and the directly pumped ANDi fiber. Both measurements were obtained with a coupled pump peak power of $32\,\mathrm{kW}$ supplied by a $110\,\mathrm{fs}$ Er:fiber laser at $40\,\mathrm{MHz}$ repetition rate and with similar overall fiber lengths. The hybrid approach increases the generated $-30\,\mathrm{dB}$ spectral bandwidth from $76\,\mathrm{THz}$ to $183\,\mathrm{THz}$ by a factor of $2.4 \simeq \sqrt{5.3}$, which agrees well with the theoretically expected scaling of the SC bandwidth with $\sqrt{P_0}$. The hybrid fiber SC covers the range $930 - 2130\,\mathrm{nm}$ while maintaining the typical smooth shape of a SC generated predominantly by OWB. The spectral modulation around the pump wavelength, observed in both fibers, can be traced back to low-level temporal sub-structures of the pump pulses emitted by the Er:fiber laser [188]. Both spectra can be reproduced very well with numerical simulations based on the GNLSE, also shown in fig. 4.10. As input all simulations use the real pulse shape of the pump laser reconstructed from TDP measurements, as well measured dispersion curves of the investigated fibers.

Simulations are carried out using the single mode GNLSE using the integration scheme presented in [216]. Nonlinear effects such as Kerr-induced SPM, self-steepening and delayed Raman effect (as modelled in [217]) are included and the angular frequency dependent nonlinear parameter $\gamma(\omega)$, as formulated in [218], relies on an approximation of the effective mode-field area [219]. A single mode scalar equation implies that polarization effects are ignored but this approximation is tolerable since only PM fibers are considered. Finally, the shortness of the fibers in use allows us to neglect any kind

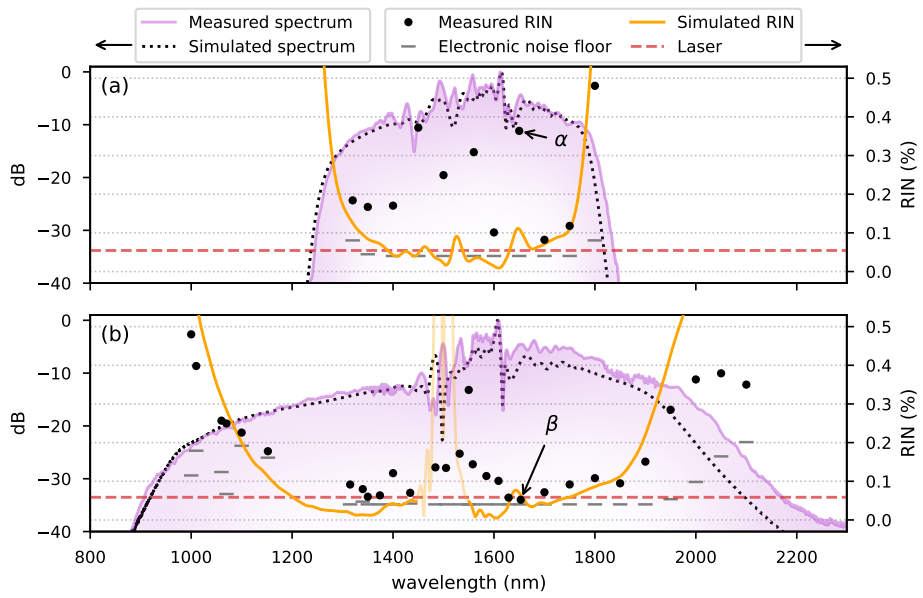

Figure 4.10: Supercontinuum spectra and spectrally resolved RIN in (a) directly-pumped ANDi fiber and (b) hybrid fiber for equal pumping conditions and similar fiber lengths. Left scale: measured (solid) and simulated (dotted) spectra; right scale: spectrally resolved measured RIN (dots) with corresponding electronic noise floor (-) and simulated values using scalar GNLSE simulations (solid yellow). The RIN of the pump laser is indicated by a red-dashed line. Detailed noise-frequency spectra of the RIN measurements at 1650 nm, marked α and β, are shown in fig. 4.12.

of loss in all the simulations. The full simulated SC generation dynamics are visualized in fig. 4.11, and confirm that the coherent OWB dynamics are enhanced and develop significantly faster in the hybrid fiber.

L_{OWB} is reduced from 1.7 cm in the directly pumped ANDi fiber to only 0.1 cm in the hybrid fiber. In the following sections, we will show that these enhanced and faster coherent dynamics are the underlying physical reason for the lower noise level of the hybrid SC.

4.3.1.4 Reduction of relative intensity noise

The spectrally resolved RIN of both SC is measured by isolating 20 µm sections of the respective spectrum with variable bandpass filters and using an ESA-based detection system sensitive to amplitude and polarization state fluctuations, as detailed above. The results are displayed in fig. 4.10. We note that both spectral bandpass and polarization filters are important to fully characterize the SC stability. As the intensity noise of SC sources is typically anti-correlated across the spectrum [220, 221], omitting these filters conceals the noise features discussed below by averaging fluctuations of anti-correlated portions of the spectrum leading to lower apparent RIN values. For this reason, our measurements are not directly comparable to studies that did not implement this spectral and polarization selectivity.

For each measured RIN value in fig. 4.10 the electronic noise floor of the detection

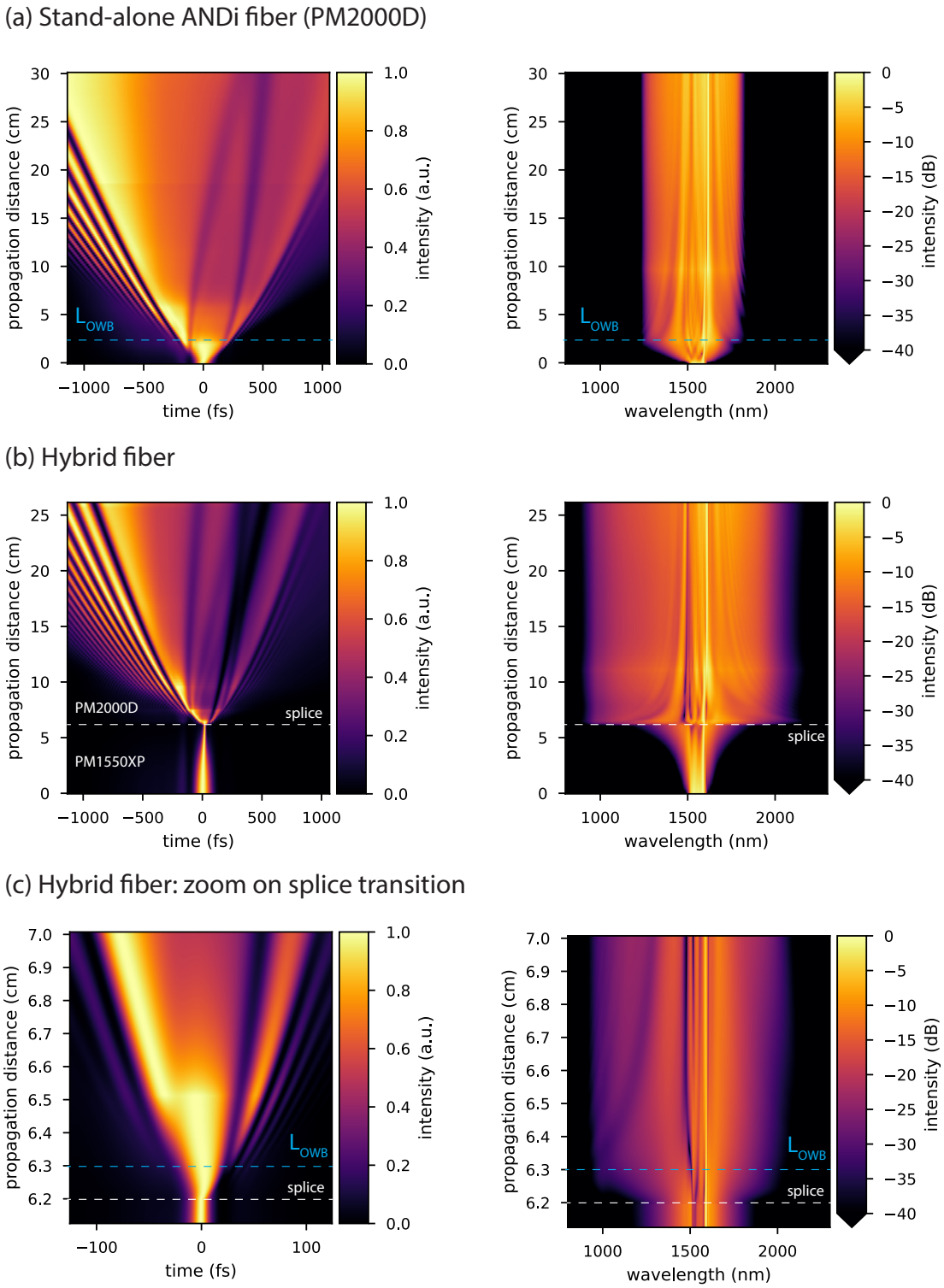

Figure 4.11: Simulated temporal (left) and spectral (right) evolution of the SC generation dynamics. (a) Stand-alone HNLF ANDi (PM2000D). The optical wave breaking length $L_{OWB} = 1.7\,\text{cm}$ is indicated. (b) Hybrid fiber. The splice between anomalous dispersion fiber (PM1550XP) and HNLF ANDi is indicated. (c) Magnified view of the splice transition. L_{OWB} decreases to approximately 0.1 cm, indicating a significant enhancement of the coherent optical wave breaking dynamics in comparison to (a).

system is also displayed so that it can be easily determined whether the detected fluctuations truly stem from the SC pulse train or are limited by the noise of the measurement apparatus. We obtain a typical electronic noise floor of 0.04 % RIN (or $-140\,\mathrm{dB_c\,Hz^{-1}}$ at high Fourier frequencies). This is higher than typically used for ultrafast laser characterization, because we tuned the system not for high sensitivity at the peak wavelength, but for providing a similar noise floor over as much spectral bandwidth and signal levels as possible. Nevertheless, in most cases the electronic noise floor is sufficiently low to fully resolve the SC noise. We also compare the measured RIN levels to corresponding values retrieved from the scalar GNLSE simulations including quantum noise and technical pump laser fluctuations [222].

Quantum shot noise is simulated by adding one photon of random phase per frequency bin at the input [223] whereas RIN is simulated by multiplying the intensity of the measured laser field by $1+\psi$ for each simulation, where ψ is sampled on a normal distribution of mean 0 and standard deviation 0.057 %, which is the measured laser RIN. After simulating the propagation of 40 pulses of complex envelope $A_i(\lambda)$, $i = 1, ..., 40$, we compute the RIN as a function of the wavelength λ in a similar way to that used in the experiment, masking the spectra with a Gaussian window and working out the coefficient of variation of the remaining energy:

$$\mathrm{RIN}(\lambda) = \frac{\sqrt{\left\langle \left(E_i(\lambda) - \langle E_j(\lambda)\rangle_j\right)^2 \right\rangle_i}}{\langle E_i(\lambda)\rangle_i}, \tag{4.2}$$

$$E_i(\lambda) = \int_{-\infty}^{\infty} |A_i(\lambda')|^2 \exp\left[\left(\frac{\lambda'-\lambda}{\lambda_0}\right)^2\right] \mathrm{d}\lambda' \tag{4.3}$$

where $\langle\rangle_i$ denotes the ensemble average over the 40 simulations and $\lambda_0 = 12.02\,\mathrm{nm}$ corresponds to a window width of 20 nm at half maximum. As consequences of this method, the input RIN is assumed to be frequency-independent and is modeled only between 1 MHz and 20 MHz. This is nevertheless adequate because the measured RIN spectrum is nearly flat in this frequency range and accounts for $> 90\,\%$ of the total measured RIN.

Surprisingly, the SC generated in the directly pumped HNLF ANDi exhibits elevated noise levels especially in the central section of the spectrum between 1400 – 1700 nm, where RIN values up to 0.4 % are detected. While this is in range with the lowest RIN values reported to date for PM-ANDi SC sources [224], in our case it corresponds to an order-of-magnitude amplification of the pump laser noise, which is unexpected for this fiber design. Importantly, the measured noise levels in the spectral center cannot be reproduced using scalar GNLSE simulations, which predict much lower RIN on the level of the pump laser noise. However, below 1400 nm and particularly above 1700 nm the simulations model the measured noise evolution more accurately, and also reproduce well the increasing RIN on the spectral edges due to the effect of laser peak power fluctuations on the SC bandwidth. This variation in simulation accuracy over the spectral range points towards the presence of incoherent nonlinearities with vectorial nature in the central part of the spectrum, since noise amplification emerging from the nonlinear coupling of polarization eigenmodes is ignored in the scalar numerical model. Indeed, a more detailed analysis provided below

identifies PMI as the origin of the elevated RIN.

In contrast, the intensity noise of the SC generated in the hybrid fiber is significantly lower and in general exhibits an exceptionally low variation with wavelength. The RIN follows very closely the values predicted by the scalar GNLSE simulations and remains mostly confined between 0.05 % and 0.2 % in the range 1150 − 1900 nm, with an average value of approx. 0.1 %. This is quite remarkable when compared to SC generated under very similar pumping conditions in the anomalous dispersion region of a fiber, where the intensity noise varies over at least two orders of magnitude and reaches several percent [220]. The RIN measured in our experiments is also up to one order of magnitude lower than previously reported values obtained from stand-alone ANDi SC sources [224–226]. Higher noise only occurs at the spectral edges and in the vicinity of sharp spectral features, where small spectral shifts induced by peak power fluctuations lead to a relatively large change in SC signal. The exact spectral position of these features is hard to simulate since they sensitively depend on low-level temporal sub-structures of the input pulse interfering with spectral components generated by SPM [188]. Hence, in fig. 4.10 (b) the simulated RIN is faded around 1500 nm where the agreement of simulated and measured SC spectrum is less accurate. The intensity noise around these features is not linked to quantum noise amplification by incoherent nonlinearities, but simply arises from the sensitivity of coherent dynamics to the input pulse parameters. Significant additional noise reduction can therefore only be achieved by improving the noise characteristics and the pulse shape of the pump laser.

4.3.1.5 Suppression of polarization modulation instability

A significant advantage of the noise detection in the frequency domain over the histogram-based statistical analysis of time-domain photodiode traces in recent work [224, 226] is the availability of a full noise frequency spectrum for every measured RIN value, which can be used to identify the underlying noise amplification mechanisms. We illustrate this for the RIN measurements recorded at 1650 nm, which are marked α and β in fig. 4.10 and result in integrated RIN of 0.38 % and 0.05 % for stand-alone ANDi and hybrid fiber SC, respectively. The detailed noise spectra for these two measurements are displayed in fig. 4.12 (a) and compared directly to the pump laser. The noise spectrum of the stand-alone ANDi SC is shifted upward by about 20 dB with respect to the pump due to the dominance of excess white noise, which is a characteristic signature of quantum noise amplification [177]. This unambiguously confirms the presence of incoherent nonlinear dynamics, which have to be of vectorial nature since they cannot be reproduced by scalar simulations, as discussed above. In contrast, these nonlinearities are suppressed in the hybrid fiber, which even exhibits slightly lower noise than the pump laser in the mid-range frequencies between 1 kHz − 1 MHz.

Fig. 4.12 (b) identifies PMI as the origin of this nonlinear noise amplification in the stand-alone HNLF-ANDi, showing that the analytically calculated PMI gain bands [82] for our experimental conditions overlap exactly with the 1400 nm − 1700 nm spectral region where the measurements in fig. 4.10 (a) detect elevated RIN values. In order to illustrate how this PMI gain leads to pulse-to-pulse intensity fluctuations of the generated SC, we conduct vectorial GNLSE simulations taking into account the coherent coupling of the two polarization eigenmodes [227]. Additionally, we increase

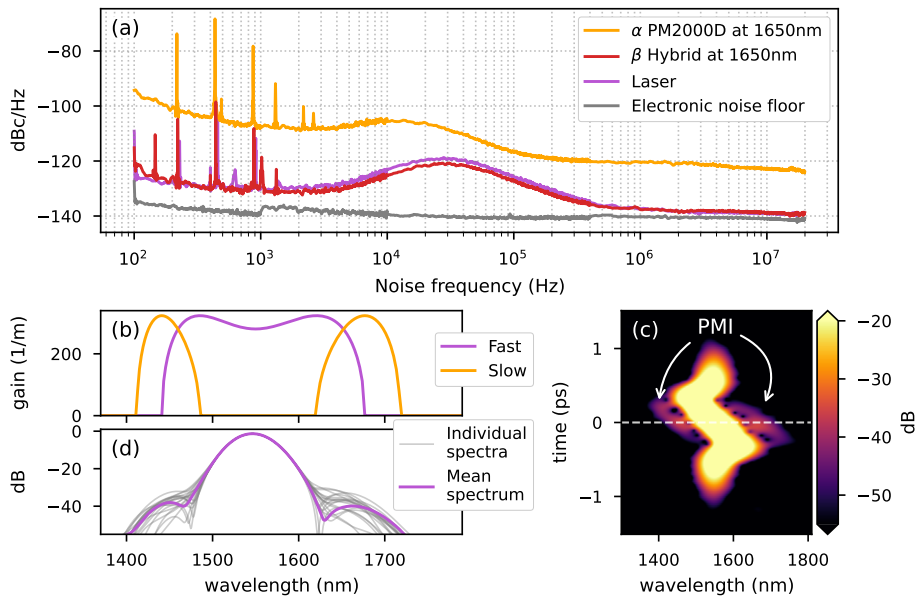

Figure 4.12: (a) Detailed noise-frequency spectra of the RIN measurements at 1650 nm, marked α and β in fig. 4.10, compared to the pump laser. (b) Analytically calculated PMI gain in HNLF-ANDi assuming a 30 kW peak power pulse propagating on slow and fast axis, respectively. (c) Simulated fast axis spectrogram of a 500 fs, 30 kW pulse after 3 cm propagation in HNLF-ANDi injected into the slow axis. (d) Spectral slice through the spectrogram in (c) at $t = 0$ for multiple simulations with random noise seeds (grey) and corresponding mean (purple).

the input pulse duration to 500 fs, which enhances the visibility of the incoherent PMI dynamics by slowing down the coherent wave-breaking process.

The simulated spectrogram in fig. 4.12 (c) shows clear signatures of PMI after only 3 cm of propagation in the form of two side bands being generated at spectro-temporal positions outside of the main pulse. As these side-bands remain unseeded, random quantum fluctuations serve as the seed and are amplified to become significant. Taking a slice through the spectrogram at $t = 0$ and repeating the simulations several times clearly shows the random amplitude fluctuations introduced by PMI at spectral positions corresponding very well to the analytically calculated PMI gain bands (compare figs. 4.12 (b) and (d)). While we consider pure slow-axis pumping in this case, in reality we expect a blend of fast- and slow-axis dynamics as we also observe linear coupling of the polarization states in the HNLF-ANDi reducing the PER from > 30 dB at the input to about 15 dB at the output, even at low power.

Why does PMI occur in the stand-alone ANDi fiber but is suppressed in the hybrid fiber? The underlying mechanism for this noise reduction relies on cascaded nonlinear dynamics. First, the pulse duration is shortened by soliton compression in the anomalous dispersion fiber, which subsequently enhances OWB and suppresses PMI in the ANDi fiber. Physically this can be understood by considering the characteristic length scales of the coherent OWB and the incoherent PMI dynamics and noting that the process with the shortest length scale plays the dominant role [82].

In the case of the stand-alone ANDi fiber, the OWB length $L_{OWB} = 1.7$ cm is

shorter but comparable to the PMI length $L_{PMI} = 5.3\,\text{cm}$, indicating a certain balance between the two processes that allows PMI to amplify noise from the shot-noise level. In the hybrid fiber, two factors suppress PMI. First, the higher birefringence and anomalous dispersion of the PM1550-XP fiber completely suppress PMI during the soliton pre-compression phase for slow axis pumping, as depicted in fig. 4.13.

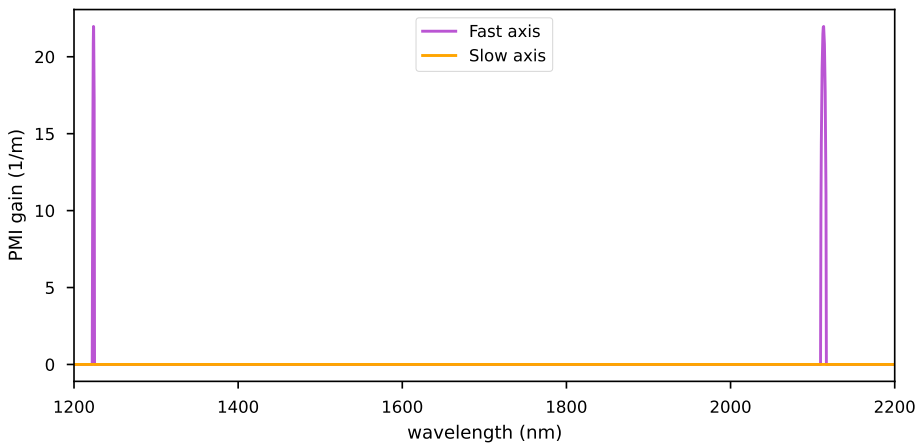

Figure 4.13: PMI gain occurring in PM1550-XP fiber assuming a 30 kW peak power pulse propagating in slow or fast axis, respectively. The calculation is based on the analytical approach detailed in [82].

Second, the pre-compressed soliton enters the ANDi fiber with much shorter duration and higher peak power than the original pulse, leading to a significant enhancement of the OWB dynamics as evident by a 17× reduction of L_{OWB} to only 0.1 cm (fig. 4.11). PMI, on the other hand, is independent of pulse duration and less influenced by the soliton pre-compression [82], resulting in a clear dominance of the coherent OWB dynamics.

The short L_{OWB} is associated with an accelerated spectro-temporal transformation of the pulse by SPM and OWB followed by a fast drop in peak power due to dispersive stretching, which in combination prevent the accumulative build-up of noise by constantly shifting the spectro-temporal positions of the PMI gain peaks. These dynamics are very similar to the suppression of scalar incoherent Raman and four-wave mixing processes in ANDi fibers at short pulse durations discussed in detail in [22].

4.3.1.6 Phase stability

The dominance of the inherently phase-coherent processes of SPM, soliton compression, and optical wave breaking during nonlinear spectral broadening suggests that the SC generated in the hybrid fiber should also exhibit excellent phase stability.We experimentally quantify the phase fluctuations using a free-space asymmetric Michelson interferometer, see fig. 4.14.

One arm of the device is set to provide a delay with respect to the other arm corresponding to the pulse repetition period, such that two subsequent SC pulses interfere with each other. If the SC pulse train is phase-stable over time intervals exceeding the

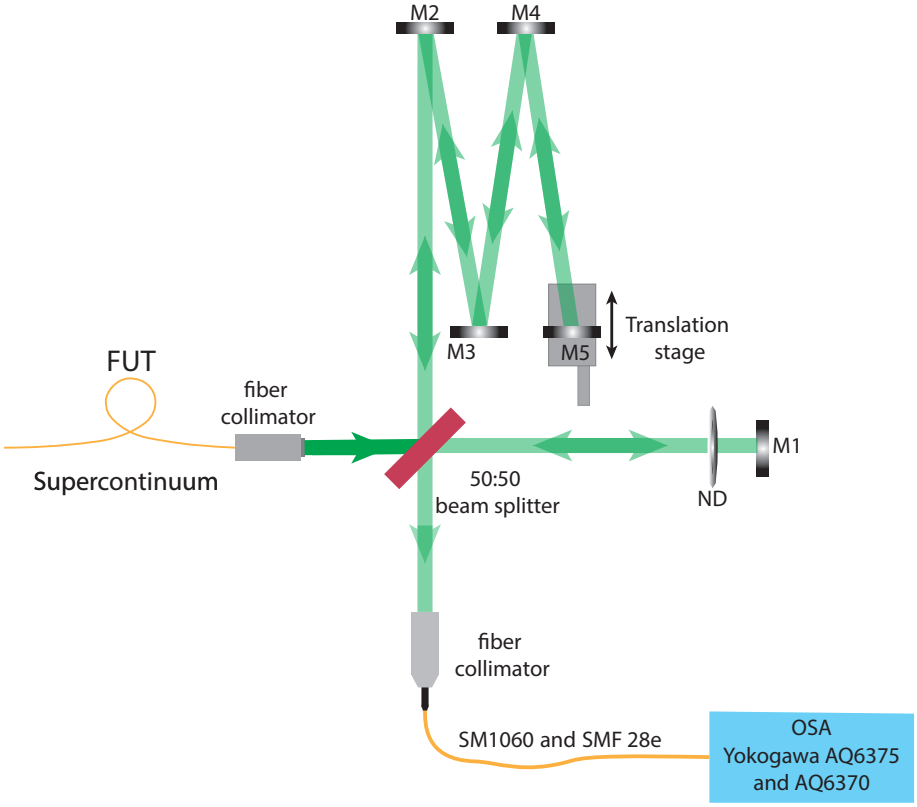

Figure 4.14: Experimental setup for the measurement of the phase coherence of the SC generated in the hybrid fiber with a free-space asymmetric Michelson interferometer. FUT: Fiber under test; M: mirror; ND: Neutral density filter; OSA: Optical spectrum analyzer; SMF: single-mode fiber

OSA sweep time, spectral interference fringes appear [228]. The SC pulses exiting the hybrid fiber are collimated using reflective optics and split into two arms by a broadband 50:50 beam splitter. One arm of the device is set to provide a delay with respect to the other arm corresponding to the pulse repetition period, such that two subsequent SC pulses interfere at the output of the interferometer. The signal is collected with a SMF and directed to an OSA, where spectral interference fringes are created if the SC pulse train is phase-stable over time intervals exceeding the OSA sweep time. The measurement was performed in sections of approximately 200 nm with optimization of the SMF coupling for each wavelength region. A neutral density filter (ND) is used to approximately match the intensity between the two arms in order to obtain good fringe visibility. Two different SMF patch cords (SM1060 and SMF28e) and two OSA (Yokogawa AQ6370 and AQ6375) were employed to cover the full bandwidth of the SC spectrum with adequate signal-to-noise levels while simultaneously ensuring single-mode guidance for good spatial overlap of the interfering signals. The fringe spacing, and hence the spectral resolution of the coherence measurement, is chosen by fine tuning the delay time between the interfering pulses using a translation stage located in the long arm. We experimentally verified that the chosen spacing has negligible effect on fringe visibility and extracted coherence as long as the fringes can be well resolved

with the OSA. A single sweep lasts several seconds and thus records the ensemble average of $> 10^8$ interference events, such that the magnitude of the degree of first-order coherence as a function of wavelength becomes measurable as [229]

$$|g_{12}(\lambda)| = \frac{V(\lambda)[I_1(\lambda) + I_2(\lambda)]}{2[I_1(\lambda)I_2(\lambda)]^{1/2}}, \tag{4.4}$$

where $I_1(\lambda)$ and $I_2(\lambda)$ are the measured light intensities in each arm of the interferometer, and $V(\lambda)$ is the fringe visibility given by the maximum and minimum fringe intensity, $V(\lambda) = [I_{\max}(\lambda) - I_{\min}(\lambda)]/[I_{\max}(\lambda) + I_{\min}(\lambda)]$. Equation (4.4) is equal to the expression routinely used in numerical studies $|g_{12}| = \langle E_1^* E_2\rangle/[\langle|E_1|^2\rangle\langle|E_2|^2\rangle]^{1/2}$ with the spectral field envelopes $E_1(\lambda), E_2(\lambda)$ and ensemble average $\langle.\rangle$, but expressed in experimentally accessible variables.

Note that the calculation of $|g_{12}(\lambda)|$ accounts for differences in the interfering intensities, which in practice are difficult to equalize exactly in broadband measurements, and therefore represents a better figure of merit for coherence than the visibility $V(\lambda)$ itself. It is well known that the value of $|g_{12}(\lambda)|$ is primarily sensitive to phase fluctuations and only to a much lesser extend to intensity noise [176, 230], such that it provides a convenient, broadband, self-referenced and high resolution measure of phase-stability complementary to the RIN characterizations performed above.

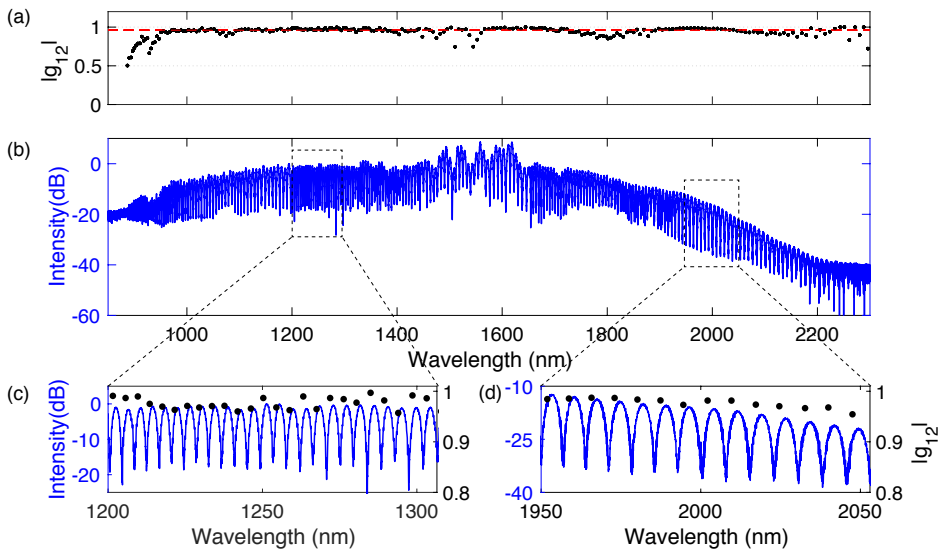

Figure 4.15: Experimental phase coherence measurements of the SC generated in the hybrid fiber using spectral interferometry. (a) Magnitude of first order coherence determined according to eq. (4.4). The red dashed line indicates the spectrally averaged coherence of $\langle|g_{12}|\rangle = 0.96$. (b) Spectral interference measurement showing high extinction fringes over the entire SC bandwidth. (c), (d) Magnified views of interference fringes and coherence around 1250 nm and 2000 nm.

Fig. 4.15 confirms the excellent phase stability of the generated SC, evident from high contrast interference fringes with visibility in the order of 20 dB measured over the entire bandwidth of the hybrid fiber SC. $|g_{12}(\lambda)|$ is near unity for the majority of

the bandwidth, as exemplary highlighted in the magnified views of fig. 4.15 (c) and (d). The coherence averaged over the full $900 - 2000\,\mathrm{nm}$ bandwidth is calculated to $\langle|g_{12}|\rangle = \int |g_{12}(\lambda)|I(\lambda)d\lambda / \int I(\lambda)d\lambda$ =0.96. This ranks among the highest experimentally confirmed magnitude and uniformity of $|g_{12}(\lambda)|$ for fiber- and waveguide-based SC sources to date [231–236]. Slightly degraded coherence is only detected at the spectral edges and around the sharp spectral features near the pump wavelength, coinciding with the regions of increased RIN in fig. 4.10 whose origin was already discussed in section 4.3.1.4. Near 1800 nm the coherence measurement is disturbed by water vapour absorption lines preventing accurate extraction of visibility and intensities. Using our experimentally determined value of $\langle|g_{12}|\rangle$ and the results of previously published numerical studies [222], we can assign a median shot-to-shot timing jitter $\delta t < 0.5\,\mathrm{fs}$ to the pulse train emitted by the hybrid SC source, revealing stability down to a small fraction of an optical cycle.

4.3.2 Extending the hybrid fiber concept to other dispersion regimes

So far we have shown ultra-low noise performance and excellent coherence values for the hybrid ANDi SC. We identified the reduced length scale of OWB, caused by the initial soliton compression, as the mechanism effectively eliminating PMI and lowering the noise, while achieving great spectral bandwidth from 930 nm to 2130 nm. But are these benefits truly unique to ANDi fibers? Could fibers in other dispersion regimes benefit from the same approach and show the same or similar effects? Here we evaluate this hybrid fiber concept for two additional common and commercially available HNLF and compare their performance under identical pumping conditions with the HNLF ANDi. The HNLF are all Germanium doped and chosen such that they form a representative set of the most common types of dispersion designs used for SC generation and, therefore, are ideally suited to experimentally study the influence of the fiber dispersion design on spectral bandwidth, flatness, and noise characteristics of the resulting SC.

We present a detailed comparison of spectrally resolved RIN of the SC light generated in these different HNLF designs, both for directly pumped and hybrid fiber versions. Only polarization-maintaining fibers are considered, as high birefringence suppresses noise arising from the nonlinear coherent coupling of the two orthogonal eigenmodes [237].

4.3.2.1 Experiment and highly nonlinear fibers

The experimental setup is the same as in the previous section, utilizing an ultrafast Er:fiber laser. While HNLF-AD and HNLF-ND exhibit a single ZDW and provide low anomalous and normal dispersion at the pump wavelength, respectively, HNLF-ANDi has an all-normal dispersion profile. Therefore, the fibers are ideally suited to experimentally clarify the influence of the fiber dispersion profile on the noise characteristics of the resulting SC under identical pumping conditions. Fig. 4.16 shows the pump source spectrum in relation to the measured group velocity dispersion profiles of the

fibers. A summary of geometric, linear and nonlinear optical parameters of the fibers used in this work is given in Table 4.1. HNLF-AD (sold by FORC-Photonics as HNLF DS) exhibits anomalous dispersion at the pump wavelength, with a ZDW of 1.47 µm and $D = 3.3\,\mathrm{ps/(nmkm)}$ at 1550 nm. Its mode field diameter (MFD) is given as 4.2 µm by the manufacturer and we estimate its nonlinear coefficient to $\gamma = 10.3\,\mathrm{W^{-1}\,m}$. Due to a slightly elliptic core the fiber has a group birefringence of 0.9×10^{-4} relative index units (RIU). On the other hand, HNLF-ND (marketed by OFS as HNLF-PM-M2) provides normal dispersion over the pump spectrum, with a ZDW of 1.62 µm and $D = -1.07\,\mathrm{ps/(nmkm)}$ at 1550 nm. Birefringence of 2.8×10^{-4} RIU is introduced by an elliptic core, and MFD as well as nonlinear coefficient are similar to HNLF-AD.

For comparison, the properties of the third fiber, HNLF-ANDi

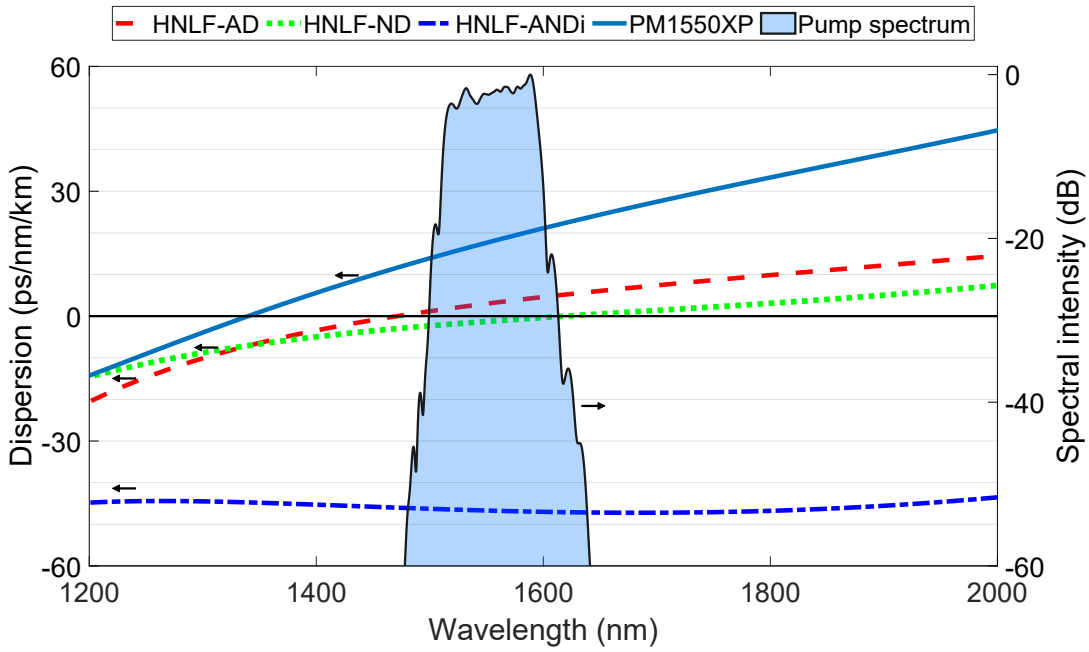

Figure 4.16: Measured dispersion curves of HNLF-AD, HNLF-ND, HNLF-ANDi, and PM1550-XP in relation to the measured spectrum of the Er:fiber femtosecond laser.

Fiber	MFD [µm]	ZDW [nm]	Dispersion $[\frac{\mathrm{ps}}{\mathrm{nm\,km}}]$	Group birefringence	Nonlinearity $[\frac{1}{\mathrm{W\,km}}]$
PM1550-XP	10.1	1340	18	4.6×10^{-4}	1.4
HNLF-AD	4.2	1469	3.3	0.9×10^{-4}	10.3
HNLF-ND	4	1620	-1.07	2.8×10^{-4}	10.5
HNLF-ANDi	3.5	All normal	-46.7	0.2×10^{-4}	13.3

Table 4.1: Geometric, linear, and nonlinear properties of the fibers used in this work. All values except ZDW are given for a wavelength of 1550 nm.

(Coherent-Nufern PM2000D) are listed again, as it has already been covered in the previous section. Compared to the other two fibers, HNLF-ANDi exhibits relatively strong and flat all-normal dispersion over the entire wavelength region of interest with $D = -46.7\,\mathrm{ps/(nm\,km)}$ at 1550 nm [211]. Its birefringence of 0.2×10^{-4} RIU is introduced by a panda structure, and it provides about 30 % higher nonlinearity compared to the other HNLFs used in this study.

The length of PM1550-XP was chosen at 5.7cm, which leads to slightly reduced pulse compression compared to the previous section. Fig. 4.17 c) illustrates the effect of the soliton compression by comparing the original 109.3 fs Er:fiber laser pulse with the compressed soliton of 22.9 fs duration obtained at the output of the 5.7 cm long piece of PM1550-XP. Both pulses are retrieved from a full spectro-temporal measurement by time-domain ptychography [213].

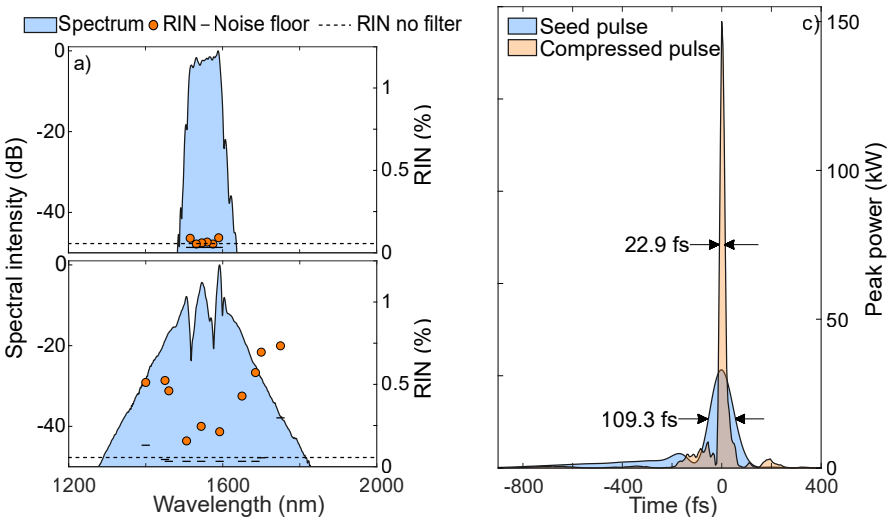

Figure 4.17: Spectrum and spectrally resolved RIN of the a) uncompressed Er:fiber femtosecond laser, and b) the compressed soliton after propagation through 5.7 cm of PM1550-XP. Left scale: measured (solid blue) spectrum; right scale: measured spectrally resolved RIN (circles) with corresponding noise floor (-). The dashed line indicates the overall RIN without any spectral filtering applied. (b) Pulse shape of the Er: fiber femtosecond laser and the compressed soliton, measured using TDP.

The compression corresponds to a temporal compression factor of 4.77 (factor 7 before) and an increase in peak power from 30 kW to 150 kW (factor 5), which is only slightly less than the 5.3 before. We still get a much shorter input pulse at much higher peak power. For the compressed 23 fs soliton pulse train, the spectrally resolved measurements reveal an increased RIN of about 0.2 % in the center and exceeding 0.6 % at the edges of the nonlinearly broadened spectrum (fig. 4.17 b). However, when the spectral filter is removed, the RIN drops to a value 0.05%, i.e. equal to the pump laser. In terms of RIN these numbers are indistinguishable to the 6.2 cm presented before.

We fabricate hybrid versions for each of the three HNLF. The PM1550-XP fiber is cleaved to a length of 5.7 ± 0.2 cm and directly fusion spliced to the respective HNLF. Using the thermally expanding core technique, already mentioned above, we routinely achieve ≤ 1 dB splice loss for all of the fibers. Taking the splice loss of ~ 1 dB into

account, we estimate the pulses to enter the HNLF section with a peak power of about 120 kW.

4.3.2.2 Performance in different dispersion regimes

Figure 4.18 presents the SC spectra generated in the six investigated nonlinear fibers together with measurements of the respective spectrally resolved RIN. All measurements were obtained with identical pumping conditions with a coupled pump peak power of 33 kW and 110 fs pulse duration. The pulses were injected into HNLF-AD, HNLF-ND and HNLF-ANDi fibers either directly (left column) or in their respective hybrid version (right column). We obtained output SC average powers of 200 mW from the directly pumped HNLF, which is reduced to about 160 mW from the hybrid fibers due to splice loss. The length of each fiber is adjusted individually in such a way that the full spectral bandwidth can develop, but short enough to avoid unnecessary spectral modulation and build-up of noise. The choice of fiber length is supported by numerical simulations further detailed in the discussion further down.

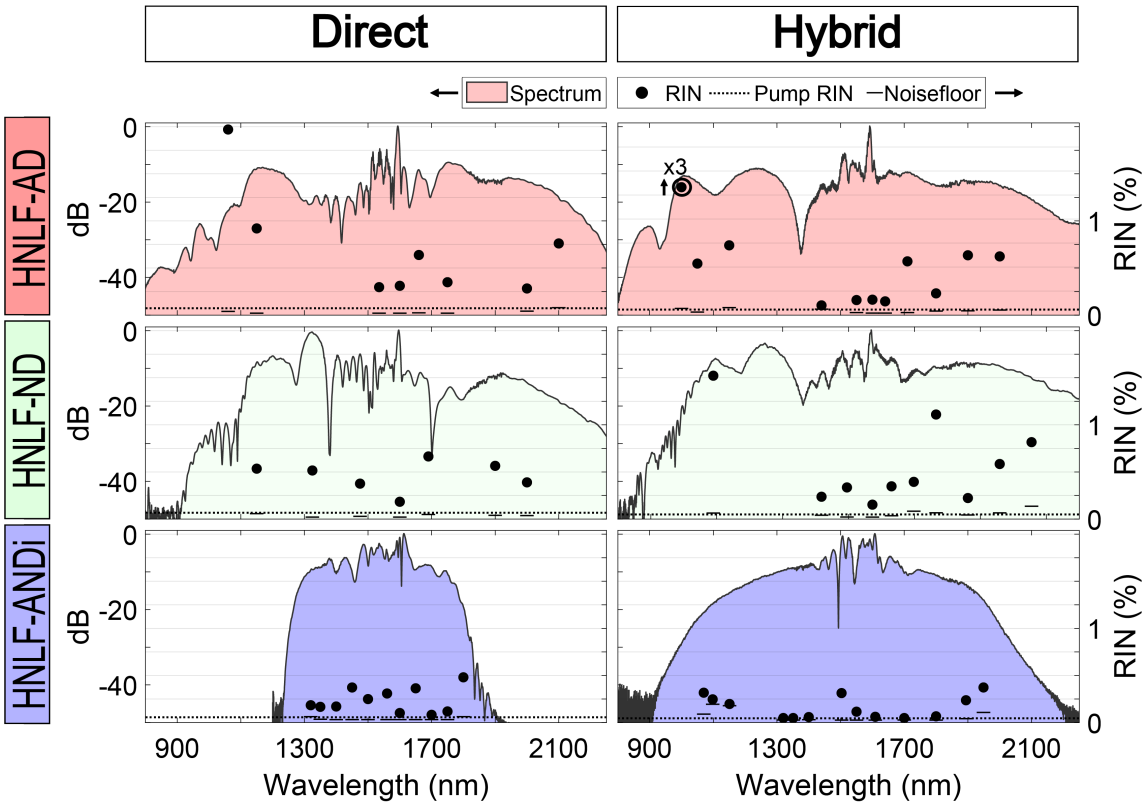

Figure 4.18: Measured SC spectra generated in the six investigated nonlinear fibers and their spectrally resolved RIN under identical pumping conditions. Pump pulses were injected directly into HNLF (left column) or in their respective hybrid version (right column). Results for HNLF-AD, HNLF-ND, and HNLF-ANDi are shown in top, middle, and bottom row, respectively. RIN is measured for spectral slices of 20 nm width (dots) shown with respective noise floor (-) and compared to the pump laser RIN (0.05 %, dashed line).

In general, we observe increased RIN levels near sharp spectral features, such as strong modulations or dips. This is due to the fact that the position of these features depends on the total nonlinear phase shift linked to the pump peak power, such that small pump fluctuations are translated to a relatively large change in SC signal. Hence, sharp spectral features generally act as amplifier of input intensity noise, and constitute an important link between flatness and noise level of SC sources.

For HNLF-AD, fig. 4.18 a) and b), the hybrid fiber generates SC spectra with significantly less fine structure, overall improved spectral flatness, and increased $-30\,\mathrm{dB}$ spectral bandwidth (176 THz vs. 150 THz). The spectra feature a broad and smooth soliton structure around 2 µm and a massive dispersive wave extending from 1.35 µm down to below 1 µm wavelength, whose position can be tuned by controlling input pulse chirp [238].

In contrast, in the SC spectra emitted by the directly pumped fiber these features are narrower and exhibit stronger spectral modulation. However, the spectrally resolved RIN measurements result in similar values for both fibers, ranging mostly between $0.25 - 1\,\%$. Near the pump wavelength we observe a noise reduction in the hybrid fiber SC to $0.1 - 0.2\,\%$, while the short wavelength dispersive wave peak generally exhibits higher noise, reaching 2 % for the directly pumped fiber and increasing to 4 % in the hybrid fiber, which corresponds to nearly 80 times amplification of the pump laser noise.

Although HNLF-ND exhibits normal dispersion at the pump wavelength, nonlinear self-phase modulation dynamics quickly transfer significant energy to the anomalous dispersion region, where dynamics are very similar to HNLF-AD discussed above, both for the directly pumped and the hybrid fiber. This is evident from the measured spectra shown in Fig. 4.18 c) and d), which generally resemble the spectra generated in HNLF-AD, but are slightly narrower on the short wavelength edge and, in the case of the directly pumped fiber, even more strongly modulated. The effect of the hybrid approach is also very similar to the previous discussion: we observe a general reduction in spectral fine structure, improved spectral flatness, and an increase in $-30\,\mathrm{dB}$ spectral bandwidth from 142 THz to 173 THz.

It is interesting to note that pumping on the normal dispersion side of the ZDW does not have a notable benefit for the stability of the SC, except for the absence of the singular very high noise peaks. In fact, for the conditions investigated in this work there is hardly any significant advantage of HNLF-ND over HNLF-AD, with the latter producing broader SC bandwidth, similar spectral shapes, and similar noise levels. HNLF-ANDi, fig. 4.18 e) and f), clearly benefits the most of all tested fibers from the hybrid approach, which approximately doubles the generated spectral bandwidth in comparison to the directly pumped fiber (145 THz vs. 75 THz, an increase by factor 1.93, measured at $-30\,\mathrm{dB}$). We note that the more optimal soliton compression stage shown before increases this bandwidth to over 180 THz, scaling according to $\sqrt{P_0}$, which easily competes with the bandwidths generated in the other investigated fibers.

The hybrid HNLF-ANDi generates the flattest SC spectrum in this study, particularly below 1400 nm and above 1700 nm. In this case we also observe also the significant noise reduction in the hybrid version of the fiber. Although the non-hybrid HNLF-ANDi generates the SC with the lowest RIN of all directly pumped HNLF, rang-

ing between $0.1 - 0.5\,\%$, this still corresponds to an amplification of the pump laser noise by up to an order of magnitude. In contrast, this noise amplification is suppressed in the hybrid fiber, as we have seen before, resulting in a SC with exceptionally low variation with wavelength. RIN is essentially equal to the pump laser noise near $0.05\,\%$ for most of the measurement points, averaging $< 0.1\,\%$ between 1150 nm and 1900 nm. RIN increases only at the spectral edges to $0.3 - 0.4\,\%$ due to a drop in signal level, which is pretty much identical to the noise levels before (fig. 4.10).

4.3.3 Discussion

For HNLF-AD choosing the correct length is critical. The fiber should be cut just after the maximum spectral broadening is obtained, i.e. to a length of 5 cm in the directly pumped case and about 1 cm for the hybrid fiber. In both cases the use of a longer HNLF section would induce stronger spectral modulations and higher noise without increasing spectral bandwidth. The same is valid for HNLF-ND, where slower nonlinear dynamics require slightly longer fiber lengths (8.5 cm for the directly pumped fiber and 2 cm for the hybrid fiber).

However, the opposite is true for HNLF-ANDi: using a longer HNLF section can be beneficial for improving flatness and noise properties. This is due to the fact that nonlinear OWB dynamics continue to reorder spectral components to unique temporal positions within the SC pulse even after spectral broadening ceases [239]. This flattens the spectrum by reducing spectral interference and reduces noise associated with sharp spectral features. Care must be taken not to use excessive fiber lengths, as this can lead to the onset of incoherent dynamics, coherence collapse, and increasing noise levels [22]. We choose 8.5 cm for the directly pumped fiber and 20 cm for the hybrid fiber. The benefit of the hybrid fiber approach for HNLF-AD and HNLF-ND is apparently limited to an improved spectral flatness and increased bandwidth, while the noise properties do not change significantly. In this section we show that these observations can be explained by the temporal characteristics of the pump pulses at the point of maximum compression reached during propagation in the fiber, which have a decisive influence over the spectral bandwidth, flatness, and noise characteristics of the resulting SC. We do this using numerical simulations for HNLF-AD and HNLF-ANDi.

Since the dynamics for HNLF-ND are qualitatively very similar to HNLF-AD, we do not discuss a separate set of simulations for this case. As the nonlinear dynamics in the HNLF-ANDi under almost identical conditions have already been covered above, a comparison of performance based on the quality of compression is made.

4.3.3.1 Spectral bandwidth and flatness

Figure 4.19 compares the simulated nonlinear spectral evolution in HNLF-AD for both direct-pumping and hybrid approaches. Although the injected pump pulses undergo soliton compression in both fibers, the nonlinear dynamics are quite different. Temporal compression and SC generation occur simultaneously in the directly pumped fiber, while in the hybrid version these processes occur largely separated in the two discrete fibers optimized for each task. Soliton compression takes place in the hybrid fiber with a nearly ideal soliton number of $N \simeq 4$, which leads to a much better quality of

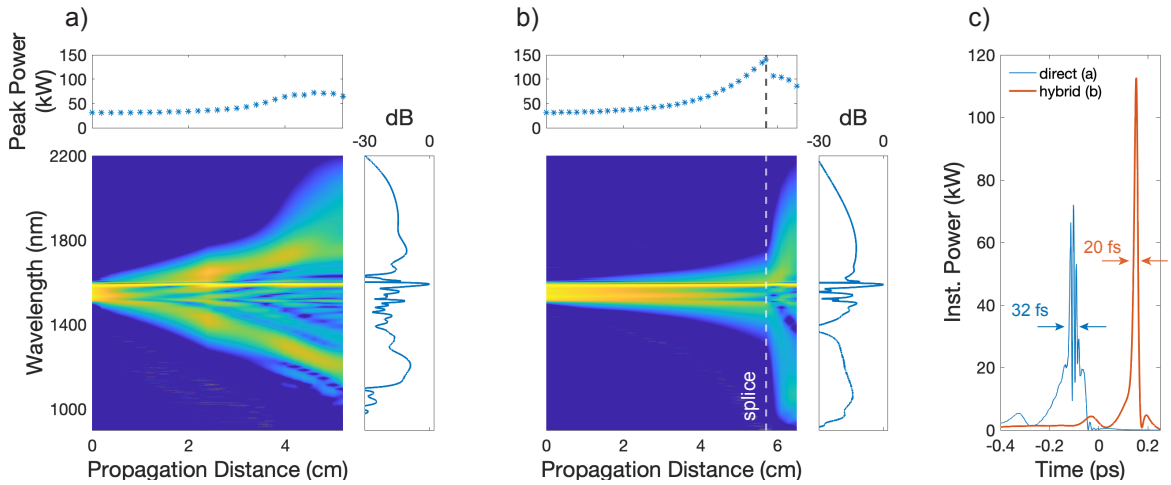

Figure 4.19: Numerical simulation of the nonlinear spectral evolution in HNLF-AD fiber using (a) direct pumping and (b) the hybrid version of the fiber. The top projections show the evolution of pulse peak power, while the right projections show the the spectrum at the exit of the fiber. (c) Temporal pulse shape at the point of maximum compression for both fibers, which occurs at a propagation distance of 4.2 cm in case of direct pumping in (a) and 5.7 cm in the hybrid version in (b), where splice losses are taken into account. The input pulse properties are modeled after the experimental conditions and are identical in both cases.

the compressed pulse as compared to the case of directly injecting the pump pulses into HNLF-AD, where they form a soliton of order $N \simeq 17$. This is evident from the comparison of the pulse shapes at the point of maximum compression in both fibers shown in fig. 4.19 c).

The high quality compression in the hybrid fiber produces a cleaner pulse shape concentrating more energy in the central pulse peak and, therefore, producing higher peak power even after splice losses are taken into account (120 kW vs. 70 kW). This directly explains the increased SC bandwidth generated with the hybrid fiber approach. The cleaner pulse shape is also the reason for the reduced spectral modulation observed in the hybrid fiber SC, because any form of temporal imperfections directly translate to strong spectral interference structures in the generated SC [188].

The same arguments can be made for HNLF-ANDi, which clearly benefits the most of all tested fibers from the hybrid concept. The corresponding simulations are shown in fig. 4.20. The directly pumped fiber does not induce any mechanisms of pulse compression and, hence, the maximum peak power is available at the input and then drops continuously during propagation in the fiber. This generates the narrowest SC spectral bandwidth in this comparison. In contrast, the initial soliton compression in the hybrid fiber increases the peak power at the point of maximum compression from 33 kW to about 120 kW by a factor of 3.6. The spectral bandwidth $\Delta\omega$ of ANDi SC can be analytically related to the peak power P_0 of the pump pulse via $\Delta\omega \propto \sqrt{P_0}$ [240], such that we expect an increase of $\Delta\omega$ by a factor of 1.9 in the hybrid fiber, which is in excellent agreement with this experiment, as well as the one presented in the previous section with better compression, where the peak power scaled by 5.3 and the frequency broadening by 2.4.

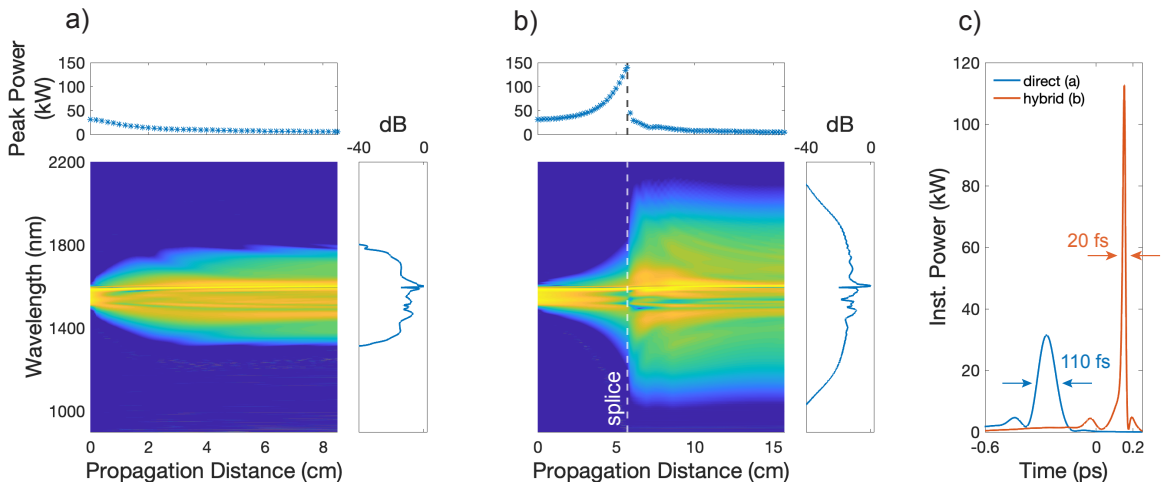

Figure 4.20: Numerical simulation of the nonlinear spectral evolution in HNLF-ANDi fiber using (a) direct pumping and (b) the hybrid version of the fiber. (c) Minimum pulse duration encountered during propagation in both fibers, which corresponds to the input pulse in case of direct pumping in (a) and to the compressed soliton at 5.7 cm in the hybrid version in (b), where splice losses are taken into account. The input pulse properties are modelled after the experimental conditions and are identical in both cases.

The quality of the pulses at the point of maximum compression shown in fig. 4.20 c) is similar, resulting also in very similar flatness of the generated SC spectra. While ANDi fibers generally produce much smoother and flatter SC spectra than their conventional counterparts, in this case there are spectral modulations present near the center in both direct pumping and hybrid approaches. These features are well reproduced in the simulations and can be identified as spectral interference structures caused by low-level temporal side peaks and pedestals of the pump pulse [188].

4.3.3.2 Noise properties

For HNLF-AD the injected pump pulses reach a very similar duration at the point of maximum compression in directly pumped and hybrid fibers, as shown in fig. 4.19 c), despite the differences in pulse quality. Hence, the noise properties of the subsequently generated SC remain similar as well. The situation is different for HNLF-ANDi. In this case we observe a significant noise reduction in the hybrid version of the fiber, which we can trace back to the strong temporal compression of the injected pulse. In the previous section we have related the elevated RIN level of up to 0.5 % in the directly pumped fiber to the occurrence of incoherent polarization modulation instability (PMI), facilitated by the relatively low birefringence of HNLF-ANDi (see table 4.1). Whether or not PMI-amplified noise becomes significant mainly depends on the strength of the competing OWB-driven coherent nonlinear dynamics [180].

With direct pumping, the coherent dynamics are relatively slow and require about 3 cm of propagation through the fiber before spectral broadening is concluded, as shown in fig. 4.20 a). This is sufficiently long for PMI to simultaneously amplify noise from the shot noise level. In the hybrid fiber however, the pump pulses enter HNLF-ANDi

with just 20 fs duration, which leads to extremely fast coherent dynamics occurring on the scale of just 1 mm after the splice, as shown in fig. 4.20 b). This suppresses PMI and prevents the accumulative build-up of noise. As a result, no significant noise amplification occurs during spectral broadening and the SC RIN drops to the limit given by the pump laser noise. It is interesting to directly compare the noise levels achieved in the three different hybrid fibers. In all of these cases, the pulse at the point of maximum compression is identical, namely the compressed 20 fs soliton delivered at the end of the SMF section. Under these conditions only the fiber design determines the noise properties of the generated SC.

As is evident from our measurements, the SC generated in the hybrid ANDi HNLF exhibits on average significantly lower noise than can be obtained in the other hybrid HNLF with conventional dispersion design pumped near their ZDW. This experimentally confirms the theoretical considerations presented at the begining of this chapter, suggesting that the gain for noise-amplifying nonlinear effects in ANDi fibers is suppressed by up to one order magnitude with respect to fibers in which a significant part of the SC spectrum overlaps with the anomalous dispersion regime.

4.4 Conclusion

We present extensive treatment of important noise sources in SC generation with regard to different fiber designs. ANDi fibers offer a clear advantage based on the coherent broadening dynamics, mainly OWB, compared to the incoherent nature of soliton-fission in anomalous dispersion. The superior noise properties of ANDi SC can be explained by the MPR gain which is an order of magnitude lower in the normal dispersion regime relevant for spectal broadening.

The importance of birefringence is highlighted, as PMI and XMI can be greatly suppressed in highly birefringent fibers. We present a noise fingerprint technique by polarization dependent RIN measurements, displaying high correlation of nonlinear noise amplification and a fibers cross-sectionial geometry. Coupling exactly to the slow axis can reduce noise greatly and leads to the lowest RIN in all fibers, while small deviations can lead to big increases in noise amplification. On the fast axis the Kerr effect can effectively negate that noise suppressing effect. In fibers experiencing very high birefringence the noise correlation is strongly reduced, as polarization noise effects are suppressed overall.

Based on the promising properties of ANDi fibers, we experimentally demonstrate a way to overcome the most significant drawback of ANDi fibers in low-noise SC generation, which is the lack of input pulse compressing properties. We combine an anomalous dispersion fiber with an ANDi fiber by carefully choosing the length of the first fiber for optimal soliton compression, reducing the pulse width of the ultrafast ER:fiber laser by 7× and increasing peak power by 5.3× before it reaches the interface with the spliced ANDi fiber, where the nonlinear broadening occurs. The result is an octave-spanning ($930 - 2130$ nm) highly coherent SC ($|g_{12}(\lambda)| = 0.96$) with ultra-low RIN between 0.05 % and 0.2 % in the range $1150 - 1900$ nm. The noise is reduced by up to an order of magnitude compared to directly pumping the ANDi fiber.

Simulations effectively identify PMI as the cause, as the birefringence of the fiber

is insufficient. The noise reduction is caused by the much reduced length scale of the broadening dynamics ($L_{OWB} = 1\,\mathrm{mm}$ compared to the length relevant for PMI ($L_{PMI} = 5.3\,\mathrm{cm}$), which is independent of peak power. This effectively eliminates PMI, as the broadening happens almost instantly, before the peak power is dropped by dispersion due to the large spectral width. Any residual noise above the pump noise level is effectively caused by the pumps pulse shape.

We then extend the hybrid fiber approach to fibers with other dispersion properties, strong anomalous dispersion as well as almost no dispersion at the pump wavelength. We see no significant change in bandwidth, compared to directly pumping the fibers and increased spectral smoothness and slightly reduced RIN. This can be traced to the improved pulse shape caused by the optimized pulse compression in the hybrid fiber. Comparing the ANDi SC to the other cases confirms the superior noise properties of ANDi SC highlighted at the beginning of the text, while reaching bandwidths even greater than the other disperion regimes, using the hybrid fiber approach. Choosing an ANDi fiber with dispersion closer to zero could further enhance OWB-dominated spectral broadening.

Using only commercial step-index polarization maintaining fibers, the hybrid approach avoids the complications associated with sourcing and integration of more complex photonic crystal fiber designs and can be readily adapted to a wide range of laser platforms and facilitate the scaling of low-noise SC sources to high repetition rates where the peak power per pulse is limited. The fibers required to reproduce our experiments are commercially available from an online catalogue at a combined cost of US$50. Hence, hybrid fibers are simple and easily reproducible solution for obtaining broadband spectra in wide range of high-precision laser applications where intensity and phase stability critically matter, including frequency comb spectroscopy, synchronization of ultrafast light sources, photonic radars, coherent optical communications, and photonic signal processing.

Bibliography

[1] Charles K. Kao. "Nobel Lecture: Sand from centuries past: Send future voices fast". In: *Rev. Mod. Phys.* 82.3 (2010), pp. 2299–2303. ISSN: 0034-6861. DOI: 10.1103/revmodphys.82.2299.

[2] Pascal Deladurantaye et al. "Material micromachining using a pulsed fiber laser platform with fine temporal nanosecond pulse shaping capability". In: *Fiber Lasers VI: Technology, Systems, and Applications*. Ed. by Denis V. Gapontsev et al. Vol. 7195. International Society for Optics and Photonics. SPIE, 2009, 71951S. DOI: 10.1117/12.809532. URL: https://doi.org/10.1117/12.809532.

[3] Anupamaa Rampur et al. "Perspective on the next generation of ultra-low noise fiber supercontinuum sources and their emerging applications in spectroscopy, imaging, and ultrafast photonics". In: *Appl. Phys. Lett.* 118 (2021), p. 240504. URL: https://doi.org/10.1063/5.0053436.

[4] Ping Lu et al. "Distributed optical fiber sensing: Review and perspective". In: *Appl. Phys. Rev.* 6.4 (2019). ISSN: 1931-9401. DOI: 10.1063/1.5113955.

[5] Gerd Keiser et al. "Review of diverse optical fibers used in biomedical research and clinical practice". In: *Journal of Biomedical Optics* 19.8 (2014), p. 080902. ISSN: 1083-3668. DOI: 10.1117/1.jbo.19.8.080902.

[6] Gabriel Loke et al. "Recent Progress and Perspectives of Thermally Drawn Multimaterial Fiber Electronics". In: *Adv. Mater.* 32.1 (2020). ISSN: 0935-9648. DOI: 10.1002/adma.201904911.

[7] Ursula J. Gibson, Lei Wei, and John Ballato. "Semiconductor core fibres: materials science in a bottle". In: *Nat. Commun.* 12.1 (2021). ISSN: 2041-1723. DOI: 10.1038/s41467-021-24135-3.

[8] J. Ballato and A. C. Peacock. "Perspective: Molten core optical fiber fabrication—A route to new materials and applications". In: *APL Photonics* 3.12 (2018). ISSN: 2378-0967. DOI: 10.1063/1.5067337.

[9] Wilfried Blanc et al. "Nanoparticles in optical fiber, issue and opportunity of light scattering [Invited]". In: *Optical Materials Express* 12.7 (2022), p. 2635. ISSN: 2159-3930. DOI: 10.1364/ome.462822.

[10] S. Nagel, J. MacChesney, and K. Walker. "An overview of the modified chemical vapor deposition (MCVD) process and performance". In: *IEEE Journal of Quantum Electronics* 18.4 (1982), pp. 459–476. ISSN: 0018-9197. DOI: 10.1109/jqe.1982.1071596.

[11] J. E. Townsend, S. B. Poole, and D. N. Payne. "Solution-doping technique for fabrication of rare-earth-doped optical fibres". In: *Electronics Letters* 23.7 (1987), p. 329. ISSN: 0013-5194. DOI: 10.1049/el:19870244.

[12] John Ballato and Peter Dragic. "Rethinking Optical Fiber: New Demands, Old Glasses". In: *Journal of the American Ceramic Society* 96.9 (2013), pp. 2675–2692. ISSN: 0002-7820. DOI: 10.1111/jace.12516.

[13] Qiubai Yang et al. "High ytterbium concentration Yb/Al/P/Ce co-doped silica fiber for 1-µm ultra-short cavity fiber laser application". In: *Opt. Express* 31.20 (Sept. 2023), pp. 33741–33752. DOI: 10.1364/OE.500051. URL: https://opg.optica.org/oe/abstract.cfm?URI=oe-31-20-33741.

[14] Dianjun Hu et al. "Terbium (III) oxide (Tb2O3) transparent ceramics by two-step sintering from precipitated powder". In: *Magnetochemistry* 8.7 (2022), p. 73.

[15] Sonja Unger et al. "Optical properties of ytterbium/aluminium doped silica glasses". In: *Opt. Mater. Express* 10.4 (2020), pp. 907–925. DOI: 10.1364/OME.388350. URL: https://opg.optica.org/ome/abstract.cfm?URI=ome-10-4-907.

[16] Mario Christian Falconi et al. "Design of a multi-wavelength fiber laser based on Tm: Er: Yb: Ho co-doped germanate glass". In: *Journal of Lightwave Technology* 38.8 (2020), pp. 2406–2413.

[17] Zhe Li et al. "Random laser emission at 1064 and 1550 nm in a Er/Yb co-doped fiber-based dual-wavelength random fiber laser". In: *Opt. Express* 32.4 (Feb. 2024), pp. 5737–5747. DOI: 10.1364/OE.508025. URL: https://opg.optica.org/oe/abstract.cfm?URI=oe-32-4-5737.

[18] GG Vienne et al. "Role of aluminum in ytterbium–erbium codoped phosphoaluminosilicate optical fibers". In: *Optical Fiber Technology* 2.4 (1996), pp. 387–393.

[19] Stuart Jackson. "Chapter 6 - Energy transfer processes in rare-earth-doped glass fiber". In: *Mid-Infrared Fiber Photonics*. Ed. by Stuart Jackson, Martin Bernier, and Réal Vallée. Woodhead Publishing Series in Electronic and Optical Materials. Woodhead Publishing, 2022, pp. 305–331. ISBN: 978-0-12-818017-4. DOI: https://doi.org/10.1016/B978-0-12-818017-4.00004-5. URL: https://www.sciencedirect.com/science/article/pii/B9780128180174000045.

[20] R.R Alfano, ed. *The supercontinuum laser source (3rd edition)*. Springer, New York, 2016.

[21] T. Sylvestre et al. "Recent advances in supercontinuum generation in specialty optical fibers [Invited]". In: *Journal of the Optical Society of America B* 38.12 (Oct. 2021), F90. DOI: 10.1364/josab.439330.

[22] Alexander M. Heidt et al. "Limits of coherent supercontinuum generation in normal dispersion fibers". In: *J. Opt. Soc. Am. B* 34.4 (2017), pp. 764–775. DOI: 10.1364/JOSAB.34.000764. URL: http://josab.osa.org/abstract.cfm?URI=josab-34-4-764.

[23] Surajit Bose et al. "Study of nonlinear dynamics in silver-nanoparticle-doped photonic crystal fiber". In: *J. Opt. Soc. Am. B* 33.6 (June 2016), pp. 1014–1021. DOI: 10.1364/JOSAB.33.001014. URL: https://opg.optica.org/josab/abstract.cfm?URI=josab-33-6-1014.

[24] John Ballato et al. "Glass and Process Development for the Next Generation of Optical Fibers: A Review". In: *Fibers* 5.1 (2017), p. 11. ISSN: 2079-6439. DOI: 10.3390/fib5010011.

[25] Gia Quyet Ngo et al. "In-fibre second-harmonic generation with embedded two-dimensional materials". In: *Nature Photonics* 16.11 (2022), pp. 769–776. ISSN: 1749-4885. DOI: 10.1038/s41566-022-01067-y.

[26] M. R. Henderson et al. "Diamond in Tellurite Glass: a New Medium for Quantum Information". In: *Advanced Materials* 23.25 (2011), pp. 2806–2810. ISSN: 0935-9648. DOI: 10.1002/adma.201100151.

[27] John Ballato and Peter D. Dragic. "Glass: The carrier of light—Part II—A brief look into the future of optical fiber". In: *International Journal of Applied Glass Science* 12.1 (2021), pp. 3–24. ISSN: 2041-1286. DOI: 10.1111/ijag.15844.

[28] Wei Zhang et al. "Yb-doped silica glass and photonic crystal fiber based on laser sintering technology". In: *Laser Phys.* 26.3 (2016), p. 035801. ISSN: 1054-660X. DOI: 10.1088/1054-660x/26/3/035801.

[29] Pawel Maniewski et al. "Rapid prototyping of silica optical fibers". In: *Opt. Mater. Express* 12.7 (2022), p. 2426. ISSN: 2159-3930. DOI: 10.1364/ome.459400.

[30] Pawel Maniewski et al. "Advances in laser-based manufacturing techniques for specialty optical fiber". In: *J. Am. Ceram. Soc.* 107.8 (2024), pp. 5143–5158. ISSN: 0002-7820. DOI: 10.1111/jace.19838.

[31] U. C. Paek. "Laser Drawing of Optical Fibers". In: *Appl. Opt.* 13.6 (June 1974), pp. 1383–1386. DOI: 10.1364/AO.13.001383. URL: https://opg.optica.org/ao/abstract.cfm?URI=ao-13-6-1383.

[32] A. Heptonstall et al. "Invited Article: CO2 laser production of fused silica fibers for use in interferometric gravitational wave detector mirror suspensions". In: *Review of Scientific Instruments* 82.1 (2011). ISSN: 0034-6748. DOI: 10.1063/1.3532770.

[33] Clarissa M. Harvey et al. "Specialty optical fiber fabrication: fiber draw tower based on a CO laser furnace". In: *J. Opt. Soc. Am. B* 38.12 (2021), F122. ISSN: 0740-3224. DOI: 10.1364/josab.437667.

[34] Taras Oriekhov et al. "Specialty optical fiber fabrication: preform manufacturing based on asymmetrical CO laser heating". In: *Journal of the Optical Society of America B* 38.12 (2021), F130. ISSN: 0740-3224. DOI: 10.1364/josab.438027.

[35] Yanhua Luo et al. "Toward optical fibre fabrication using 3D printing technology". In: *Opt. Fiber Technol.* 58 (2020), p. 102299. ISSN: 1068-5200. DOI: 10.1016/j.yofte.2020.102299.

[36] Pawel Maniewski et al. "Er-doped silica fiber laser made by powder-based additive manufacturing". In: *Optica* 10.10 (2023), p. 1280. ISSN: 2334-2536. DOI: 10.1364/optica.493601.

[37] F. R. Arteaga-Sierra, A. Antikainen, and Govind P. Agrawal. "Soliton dynamics in photonic-crystal fibers with frequency-dependent Kerr nonlinearity". In: *Phys. Rev. A* 98 (1 July 2018), p. 013830. DOI: 10.1103/PhysRevA.98.013830. URL: https://link.aps.org/doi/10.1103/PhysRevA.98.013830.

[38] Grzegorz Stępniewski et al. "Nonlinearity shaping in nanostructured glass-diamond hybrid materials for optical fiber preforms". In: *Carbon* 215 (2023), p. 118465.

[39] Urs Pedrazza, Valerio Romano, and Willy Lüthy. "Yb3+: Al3+: sol–gel silica glass fiber laser". In: *Optical Materials* 29.7 (2007), pp. 905–907.

[40] S Acosta et al. "Preparation of alumina gels by a non-hydrolytic sol-gel processing method". In: *Journal of non-crystalline solids* 170.3 (1994), pp. 234–242.

[41] Dunia Blaser et al. "Multimode Ytterbium–Aluminosilicate Core Optical Fibre for Amplification and Laser Applications". In: *Fiber* 11 (2023). DOI: 10.3390/fib11110095. URL: https://www.mdpi.com/2079-6439/11/11/95.

[42] Eugene Hecht. *Optics*. 5th. Pearson, 2016. ISBN: 9780133977226.

[43] Rick Trebino. *Frequency-Resolved Optical Gating: The Measurement of Ultrashort Laser Pulses*. 1st ed. Springer Book Archive. Springer Science+Business Media New York 2000. Springer New York, NY, 2000, pp. XVII, 425. ISBN: 978-1-4020-7066-2. DOI: 10.1007/978-1-4615-1181-6. URL: https://doi.org/10.1007/978-1-4615-1181-6.

[44] G.P. Agrawal. *Fiber-Optic Communication Systems*. Wiley, 2021. ISBN: 9781119737360. URL: https://books.google.ch/books?id=RkwvEAAAQBAJ.

[45] Xiaoqiang Jiang and Ruichun Wang. In: *Journal of Optical Communications* 29.1 (2008), pp. 12–15. DOI: doi:10.1515/JOC.2008.29.1.12. URL: https://doi.org/10.1515/JOC.2008.29.1.12.

[46] Anton V. Bourdine. "Design of reverse DMD multimode fibers". In: *Optical Technologies for Telecommunications 2007*. Ed. by Vladimir A. Andreev et al. Vol. 7026. International Society for Optics and Photonics. SPIE, 2008, p. 702606. DOI: 10.1117/12.801466. URL: https://doi.org/10.1117/12.801466.

[47] Constance Valentin et al. "Top-hat beam output of a single-mode microstructured optical fiber: Impact of core index depression". In: *Opt. Express* 21.20 (Oct. 2013), pp. 23250–23260. DOI: 10.1364/OE.21.023250. URL: https://opg.optica.org/oe/abstract.cfm?URI=oe-21-20-23250.

[48] C. Jollivet et al. "Specialty flat-top beam delivery fibers with controlled beam parameter product". In: *Laser Resonators, Microresonators, and Beam Control XVIII*. Ed. by Alexis V. Kudryashov, Alan H. Paxton, and Vladimir S. Ilchenko. Vol. 9727. International Society for Optics and Photonics. SPIE, 2016, 97270T. DOI: 10.1117/12.2209348. URL: https://doi.org/10.1117/12.2209348.

[49] Rafal Kasztelanic et al. "Free-Form Optical Fiber with a Square Mode and Top-Hat Intensity Distribution". In: *Advanced Science* n/a.n/a (), p. 2402886. DOI: https://doi.org/10.1002/advs.202402886. eprint: https://onlinelibrary.wiley.com/doi/pdf/10.1002/advs.202402886. URL: https://onlinelibrary.wiley.com/doi/abs/10.1002/advs.202402886.

[50] Alaaeddine Rjeb et al. "Inverse-raised-cosine fibers for next-generation orbital angular momentum systems". In: *Optics Communications* 458 (2020), p. 124736. ISSN: 0030-4018. DOI: https://doi.org/10.1016/j.optcom.2019.124736. URL: https://www.sciencedirect.com/science/article/pii/S0030401819309162.

[51] Zhishen Zhang et al. "Optical fiber design with orbital angular momentum light purity higher than 99.9%". In: *Opt. Express* 23.23 (Nov. 2015), pp. 29331–29341. DOI: 10.1364/OE.23.029331. URL: https://opg.optica.org/oe/abstract.cfm?URI=oe-23-23-29331.

[52] T. A. Birks, J. C. Knight, and P. St. J. Russell. "Endlessly single-mode photonic crystal fiber". In: *Opt. Lett.* 22.13 (July 1997), pp. 961–963. DOI: 10.1364/OL.22.000961. URL: https://opg.optica.org/ol/abstract.cfm?URI=ol-22-13-961.

[53] J. C. Knight et al. "Properties of photonic crystal fiber and the effective index model". In: *J. Opt. Soc. Am. A* 15.3 (Mar. 1998), pp. 748–752. DOI: 10.1364/JOSAA.15.000748. URL: https://opg.optica.org/josaa/abstract.cfm?URI=josaa-15-3-748.

[54] Jonas Scheuner et al. "Design and realisation of leakage channel fibres by the powder-in-tube method". In: *Micro-Structured and Specialty Optical Fibres IV*. Vol. 9886. SPIE. 2016, pp. 163–172.

[55] Xiuquan Ma et al. "Single-mode chirally-coupled-core fibers with larger than 50μm diameter cores". In: *Optics express* 22.8 (2014), pp. 9206–9219.

[56] D. Mogilevtsev, T. A. Birks, and P. St. J. Russell. "Group-velocity dispersion in photonic crystal fibers". In: *Opt. Lett.* 23.21 (Nov. 1998), pp. 1662–1664. DOI: 10.1364/OL.23.001662. URL: https://opg.optica.org/ol/abstract.cfm?URI=ol-23-21-1662.

[57] Kunimasa Saitoh and Masanori Koshiba. "Highly nonlinear dispersion-flattened photonic crystal fibers for supercontinuum generation in a telecommunication window". In: *Opt. Express* 12.10 (May 2004), pp. 2027–2032. DOI: 10.1364/OPEX.12.002027. URL: https://opg.optica.org/oe/abstract.cfm?URI=oe-12-10-2027.

[58] Van Thuy Hoang et al. "Broadband low-dispersion low-nonlinearity photonic crystal fiber dedicated to near-infrared high-power femtosecond pulse delivery". In: *Optical Fiber Technology* 42 (2018), pp. 119–125. ISSN: 1068-5200. DOI: https://doi.org/10.1016/j.yofte.2018.03.003. URL: https://www.sciencedirect.com/science/article/pii/S1068520017304509.

[59] Pochi Yeh, Amnon Yariv, and Emanuel Marom. "Theory of Bragg fiber". In: *JOSA* 68.9 (1978), pp. 1196–1201.

[60] R. F. Cregan et al. "Single-Mode Photonic Band Gap Guidance of Light in Air". In: *Science* 285.5433 (1999), pp. 1537–1539. DOI: 10.1126/science.285.5433.1537. eprint: https://www.science.org/doi/pdf/10.1126/science.285.5433.1537. URL: https://www.science.org/doi/abs/10.1126/science.285.5433.1537.

[61] Zhixin Liu et al. "Nonlinearity-free coherent transmission in hollow-core antiresonant fiber". In: *Journal of Lightwave Technology* 37.3 (2018), pp. 909–916.

[62] R Zeltner et al. "Fluorescence-based remote irradiation sensor in liquid-filled hollow-core photonic crystal fiber". In: *Applied Physics Letters* 108.23 (2016).

[63] John R Hayes et al. "Antiresonant hollow core fiber with an octave spanning bandwidth for short haul data communications". In: *Journal of Lightwave Technology* 35.3 (2017), pp. 437–442.

[64] O. Schmidt et al. "High power narrow-band fiber-based ASE source". In: *Opt. Express* 19.5 (Feb. 2011), pp. 4421–4427. DOI: 10.1364/OE.19.004421. URL: https://opg.optica.org/oe/abstract.cfm?URI=oe-19-5-4421.

[65] Orazio Svelto et al. "Lasers and Coherent Light Sources". In: *Springer Handbook of Lasers and Optics*. Ed. by Frank Träger. Berlin, Heidelberg: Springer Berlin Heidelberg, 2012, pp. 641–1046. ISBN: 978-3-642-19409-2. DOI: 10.1007/978-3-642-19409-2_11. URL: https://doi.org/10.1007/978-3-642-19409-2_11.

[66] W. J. Miniscalco and R. S. Quimby. "General procedure for the analysis of Er3+ cross sections". In: *Opt. Lett.* 16.4 (Feb. 1991), pp. 258–260. DOI: 10.1364/OL.16.000258. URL: https://opg.optica.org/ol/abstract.cfm?URI=ol-16-4-258.

[67] B Aull and H Jenssen. "Vibronic interactions in Nd: YAG resulting in nonreciprocity of absorption and stimulated emission cross sections". In: *IEEE Journal of Quantum Electronics* 18.5 (1982), pp. 925–930.

[68] Valerii (Vartan) Ter-Mikirtychev. "Optical Properties and Optical Spectroscopy of Rare Earth Ions in Solids". In: *Fundamentals of Fiber Lasers and Fiber Amplifiers*. Cham: Springer International Publishing, 2014, pp. 7–26. ISBN: 978-3-319-02338-0. DOI: 10.1007/978-3-319-02338-0_2. URL: https://doi.org/10.1007/978-3-319-02338-0_2.

[69] HM Pask et al. "Ytterbium-doped silica fiber lasers: versatile sources for the 1-1.2/spl mu/m region". In: *IEEE Journal of Selected Topics in Quantum Electronics* 1.1 (1995), pp. 2–13.

[70] Michel JF Digonnet. *Rare-earth-doped fiber lasers and amplifiers, revised and expanded*. CRC press, 2001.

[71] W.L. Barnes et al. "Absorption and emission cross section of Er/sup 3+/ doped silica fibers". In: *IEEE Journal of Quantum Electronics* 27.4 (1991), pp. 1004–1010. DOI: 10.1109/3.83335.

[72] Hongkun Nie et al. "Rare-earth ions-doped mid-infrared (2.7–3 µm) bulk lasers: a review [Invited]". In: *Chinese Optics Letters* 19.11 (Sept. 2021), p. 091407. URL: https://www.researching.cn/articles/OJc8f3d5caaf05f93a.

[73] Zian Cheak Tiu et al. "Q-Switching pulse generation with thulium-doped fiber saturable absorber". In: *Chinese Physics Letters* 31.12 (2014), p. 124203.

[74] Amos Martinez and Zhipei Sun. "Nanotube and graphene saturable absorbers for fibre lasers". In: *Nature Photonics* 7.11 (2013), pp. 842–845.

[75] Joachim Herrmann. "Theory of Kerr-lens mode locking: role of self-focusing and radially varying gain". In: *Josa b* 11.3 (1994), pp. 498–512.

[76] Masataka Nakazawa, Eiji Yoshida, and Yasuo Kimura. "Low threshold, 290 fs erbium-doped fiber laser with a nonlinear amplifying loop mirror pumped by InGaAsP laser diodes". In: *Applied physics letters* 59.17 (1991), pp. 2073–2075.

[77] U. Keller. *Ultrafast Lasers: A Comprehensive Introduction to Fundamental Principles with Practical Applications*. Graduate Texts in Physics. Springer International Publishing, 2022. ISBN: 9783030825317. URL: https://books.google.ch/books?id=jjuEzgEACAAJ.

[78] Sandro M. Link et al. "Dual-comb modelocked laser". In: *Opt. Express* 23.5 (Mar. 2015), pp. 5521–5531. DOI: 10.1364/OE.23.005521. URL: https://opg.optica.org/oe/abstract.cfm?URI=oe-23-5-5521.

[79] S. Schiller. "Spectrometry with frequency combs". In: *Opt. Lett.* 27.9 (May 2002), pp. 766–768. DOI: 10.1364/OL.27.000766. URL: https://opg.optica.org/ol/abstract.cfm?URI=ol-27-9-766.

[80] Zachary L. Newman et al. "Architecture for the photonic integration of an optical atomic clock". In: *Optica* 6.5 (May 2019), pp. 680–685. DOI: 10.1364/OPTICA.6.000680. URL: https://opg.optica.org/optica/abstract.cfm?URI=optica-6-5-680.

[81] Ian Coddington, Nathan Newbury, and William Swann. "Dual-comb spectroscopy". In: *Optica* 3.4 (2016), pp. 414–426.

[82] G.P. Agrawal. *Nonlinear Fiber Optics*. Academic Press, 2007.

[83] F. Silva et al. "Multi-octave supercontinuum generation from mid-infrared filamentation in a bulk crystal". In: *Nature Communications* 3 (2012), p. 807. DOI: 10.1038/ncomms1816.

[84] S. Lakó et al. "Pulse compression of nanojoule pulses in the visible using microstructure optical fiber and dispersion compensation". In: *Applied Physics B* 76 (2003), pp. 267–275. DOI: 10.1007/s00340-002-1090-6.

[85] U. C. Paek. "Free Drawing and Polymer Coating of Silica Glass Optical Fibers". In: *Journal of Heat Transfer* 121.4 (Nov. 1999), pp. 774–788. ISSN: 0022-1481. DOI: 10.1115/1.2826066. eprint: https://asmedigitalcollection.asme.org/heattransfer/article-pdf/121/4/774/5911368/774_1.pdf. URL: https://doi.org/10.1115/1.2826066.

[86] H. A. Aulich, J. G. Grabmaier, and K. H. Eisenrith. "Drawing optical fiber bundles from a double crucible: a new technique". In: *Appl. Opt.* 17.2 (Jan. 1978), pp. 170–171. DOI: 10.1364/AO.17.000170. URL: https://opg.optica.org/ao/abstract.cfm?URI=ao-17-2-170.

[87] M. Yoshiyagawa et al. "Optical transmission properties of low loss-large numerical aperture glass fibers made by the double-crucible technique". In: *Journal of Non-Crystalline Solids* 40.1 (1980). Proceedings of the Fifth University Conference on Glass Science, pp. 489–497. ISSN: 0022-3093. DOI: https://doi.org/10.1016/0022-3093(80)90124-6. URL: https://www.sciencedirect.com/science/article/pii/0022309380901246.

[88] Yao-Ming Chang. "Manufacture of optical fiber by the double crucible with 20 nozzles". In: *Optoelectronic Devices and Applications*. Ed. by Sriram Sriram. Vol. 1338. International Society for Optics and Photonics. SPIE, 1990, pp. 41–47. DOI: 10.1117/12.22975. URL: https://doi.org/10.1117/12.22975.

[89] Lili Wang et al. "A new approach to mass fabrication technology of microstructured polymer optical fiber preform". In: *Chin. Opt. Lett.* 3.S1 (Aug. 2005), S94–S95. URL: https://opg.optica.org/col/abstract.cfm?URI=col-3-101-S94.

[90] Amit Belwalkar et al. "Extruded tellurite glass optical fiber preforms". In: *Journal of Materials Processing Technology* 210.14 (2010), pp. 2016–2022. ISSN: 0924-0136. DOI: https://doi.org/10.1016/j.jmatprotec.2010.07.018. URL: https://www.sciencedirect.com/science/article/pii/S0924013610002128.

[91] M. Mignanelli et al. "Polymer microstructured fibers by one-step extrusion". In: *Opt. Express* 15.10 (May 2007), pp. 6183–6189. DOI: 10.1364/OE.15.006183. URL: https://opg.optica.org/oe/abstract.cfm?URI=oe-15-10-6183.

[92] Brit M. Quandt et al. "Optimization of novel melt-extruded polymer optical fibers designed for pressure sensor applications". In: *European Polymer Journal* 88 (2017), pp. 44–55. ISSN: 0014-3057. DOI: https://doi.org/10.1016/j.eurpolymj.2016.12.032. URL: https://www.sciencedirect.com/science/article/pii/S0014305716315257.

[93] Kevin Kiedrowski et al. "Laser-induced damage in passive and active polymer optical fibers". In: *2019 Conference on Lasers and Electro-Optics Europe and European Quantum Electronics Conference*. Optica Publishing Group, 2019, $ce_{p2}1$. URL: https://opg.optica.org/abstract.cfm?URI=CLEO_Europe-2019-ce_p_21.

[94] Corning Incorporated. *Corning® SMF-28® ULL Optical Fiber Datasheet*. Accessed: 2024-06-06. 2023. URL: https://www.corning.com/media/worldwide/coc/documents/Fiber/SMF-28%20ULL.pdf.

[95] H. Bauch and V. Paquet. In: *Journal of Optical Communications* 8.4 (1987), pp. 136–139. DOI: doi:10.1515/JOC.1987.8.4.136. URL: https://doi.org/10.1515/JOC.1987.8.4.136.

[96] H. Bauch, V. Paquet, and W. Siefert. "Preparation of Optical Fiber Preforms by Plasma-Impulse-CVD". In: *Optical Fiber Characteristics and Standards*. Ed. by Remy Bouillie. Vol. 0584. International Society for Optics and Photonics. SPIE, 1986, pp. 33–39. DOI: 10.1117/12.950954. URL: https://doi.org/10.1117/12.950954.

[97] Th. Hünlich et al. In: *Journal of Optical Communications* 8.4 (1987), pp. 122–129. DOI: doi:10.1515/JOC.1987.8.4.122. URL: https://doi.org/10.1515/JOC.1987.8.4.122.

[98] "Method of making optical waveguide fibers". US4217027A. Accessed: 2024-06-06. 1980. URL: https://patents.google.com/patent/US4217027A/en.

[99] JR Simpson, John B MacChesney, and KL Walker. "High rate MCVD". In: *Journal of Non-Crystalline Solids* 38 (1980), pp. 831–836.

[100] EM Dianov et al. "Application of reduced-pressure plasma CVD technology to the fabrication of Er-doped optical fibers". In: *Optical materials* 3.3 (1994), pp. 181–185.

[101] J. Stone and C.A. Burrus. "Neodymiumâ€doped silica lasers in endâ€pumped fiber geometry". In: *Applied Physics Letters* 23.7 (Oct. 1973), pp. 388–389. ISSN: 0003-6951. DOI: 10.1063/1.1654929. eprint: https://pubs.aip.org/aip/apl/article-pdf/23/7/388/18428283/388_1_online.pdf. URL: https://doi.org/10.1063/1.1654929.

[102] S.B. Poole, D.N. Payne, and M.E. Fermann. "Fabrication of low-loss optical fibres containing rare-earth ions". Undetermined. In: *Electronics Letters* 21.17 (1985), pp. 737–738. DOI: 10.1049/el:19850520.

[103] SM Aljamimi et al. "Aluminum doped silica preform fabrication using MCVD and solution doping technique: Effects of various aluminum solution concentrations". In: *2013 IEEE 4th International Conference on Photonics (ICP)*. IEEE. 2013, pp. 268–271.

[104] Adam Filipkowski et al. "Development of large core microstructured polymer optical fiber". In: *Microstructured and Specialty Optical Fibres*. Vol. 8426. SPIE. 2012, pp. 311–317.

[105] D Pysz et al. "Stack and draw fabrication of soft glass microstructured fiber optics". In: *Bulletin of the Polish Academy of Sciences. Technical Sciences* 62.4 (2014), pp. 667–682.

[106] D. Ghosh, S. Roy, M. Pal, et al. "Index-Guided Photonic Crystal Fibers: Study of Fiber Drawing Parameters". In: *Journal of Optics* 37 (2008), pp. 72–77. DOI: 10.1007/BF03354840.

[107] Christian Pflanz and Jens Ketelaer. "Ultrasonic-assisted drilling of preforms for fibre optics". In: *Tenth European Seminar on Precision Optics Manufacturing*. Vol. 12755. SPIE. 2023, pp. 31–34.

[108] John Canning et al. "3D printing optical fibre preforms". In: *Asia communications and photonics conference*. Optica Publishing Group. 2015, ASu4B–2.

[109] Przemysław Gołębiewski et al. "3D soft glass printing of preforms for microstructured optical fibers". In: *Additive Manufacturing* 79 (2024), p. 103899. ISSN: 2214-8604. DOI: https://doi.org/10.1016/j.addma.2023.103899. URL: https://www.sciencedirect.com/science/article/pii/S2214860423005122.

[110] Yitao Wang et al. "3D Laser Engineering of Molten Core Optical Fibers: Toward a New Generation of Harsh Environment Sensing Devices". In: *Advanced Optical Materials* 10.18 (2022), p. 2200379. DOI: https://doi.org/10.1002/adom.202200379. eprint: https://onlinelibrary.wiley.com/doi/pdf/10.1002/adom.202200379. URL: https://onlinelibrary.wiley.com/doi/abs/10.1002/adom.202200379.

[111] S. Morris et al. "Reactive molten core fabrication of silicon optical fiber". In: *Opt. Mater. Express* 1.6 (Oct. 2011), pp. 1141–1149. DOI: 10.1364/OME.1.001141. URL: https://opg.optica.org/ome/abstract.cfm?URI=ome-1-6-1141.

[112] Ali El Sayed et al. "Properties of Yb doped silica fibers with different Al and P co-dopants concentrations produced by the Sol-Gel based granulated silica method". In: *Micro-Structured and Specialty Optical Fibres V*. Vol. 10681. SPIE. 2018, pp. 16–24.

[113] Valerio Romano, Soenke Pilz, and Dereje Etissa. "Sol-gel-based doped granulated silica for the rapid production of optical fibers". In: *International Journal of Modern Physics B* 28.12 (2014), p. 1442010. DOI: 10.1142/S0217979214420107. URL: https://doi.org/10.1142/S0217979214420107.

[114] Sönke Pilz et al. "Granulated Silica Method for the Fiber Preform Production". In: *Fibers* 5.3 (2017). ISSN: 2079-6439. DOI: 10.3390/fib5030024. URL: https://www.mdpi.com/2079-6439/5/3/24.

[115] K. Susa et al. "New optical fibre fabrication method". In: *Electron. Lett.* 18.12 (1982), p. 499. ISSN: 0013-5194. DOI: 10.1049/el:19820339.

[116] Fengqing Wu et al. "Low-loss rare earth doped single-mode fiber by sol-gel method". In: *Materials Research Bulletin* 28.7 (1993), pp. 637–644. ISSN: 0025-5408. DOI: 10.1016/0025-5408(93)90107-o.

[117] Martin Leich et al. "Highly efficient Yb-doped silica fibers prepared by powder sinter technology". In: *Opt. Lett.* 36.9 (2011), p. 1557. ISSN: 0146-9592. DOI: 10.1364/ol.36.001557.

[118] Yigang Li et al. "Optical Properties and Laser Output of Heavily Yb-Doped Fiber Prepared by Sol-Gel Method and DC-RTA Technique". In: *J. Lightwave Technol.* 26.18 (2008), pp. 3256–3260. ISSN: 0733-8724. DOI: 10.1109/jlt.2008.925038.

[119] Vlastimil Matějec et al. “Sol-Gel fabrication and properties of silica cores of optical fibers doped with Yb3+, Er3+, Al2 O3 or TiO2”. In: *Journal of sol-gel science and technology* 13 (1998), pp. 617–621.

[120] Martin Neff, Valerio Romano, and Willy Lüthy. “Metal-doped fibres for broadband emission: Fabrication with granulated oxides”. In: *Optical materials* 31.2 (2008), pp. 247–251.

[121] G. Granger et al. “Nanostructured optical fibers in the SiO2/SnO2 system by the sol-gel method”. In: *Materials Letters* 120 (2014), pp. 292–294. ISSN: 0167-577X. DOI: 10.1016/j.matlet.2014.01.104.

[122] R. Paschotta et al. “Ytterbium-doped fiber amplifiers”. In: *IEEE J. Quantum Electron.* 33 (1997), pp. 1049–1056. ISSN: 0018-9197. DOI: 10.1109/3.594865.

[123] Ping Yan et al. “High-power 1018 nm ytterbium-doped fiber laser with output of 805 W”. In: *Opt. Lett.* 42.7 (Apr. 2017), pp. 1193–1196. DOI: 10.1364/OL.42.001193. URL: https://opg.optica.org/ol/abstract.cfm?URI=ol-42-7-1193.

[124] Liu Xiaojuan et al. “Narrow linewidth Yb-doped fiber laser at 1120 nm”. In: *Appl. Opt.* 52.9 (Mar. 2013), pp. 1829–1831. DOI: 10.1364/AO.52.001829. URL: https://opg.optica.org/ao/abstract.cfm?URI=ao-52-9-1829.

[125] F. Ö. Ilday et al. “Generation of 36-femtosecond pulses from a ytterbium fiber laser”. In: *Opt. Express* 11.26 (Dec. 2003), pp. 3550–3554. DOI: 10.1364/OE.11.003550. URL: https://opg.optica.org/oe/abstract.cfm?URI=oe-11-26-3550.

[126] T. Sun et al. “Ytterbium-based fluorescence decay time fiber optic temperature sensor systems”. In: *Review of Scientific Instruments* 69.12 (Dec. 1998), pp. 4179–4185. ISSN: 0034-6748. DOI: 10.1063/1.1149267. eprint: https://pubs.aip.org/aip/rsi/article-pdf/69/12/4179/19019776/4179_1_online.pdf. URL: https://doi.org/10.1063/1.1149267.

[127] M.R.A. Moghaddam et al. “Experimental and theoretical studies on ytterbium sensitized erbium-doped fiber amplifier”. In: *Optik* 122.20 (2011), pp. 1783–1786. ISSN: 0030-4026. DOI: https://doi.org/10.1016/j.ijleo.2010.10.038. URL: https://www.sciencedirect.com/science/article/pii/S0030402610005267.

[128] J Kirchhof et al. “The influence of Yb2+ ions on optical properties and power stability of ytterbium-doped laser fibers”. In: *Optical Components and Materials VII*. Vol. 7598. SPIE. 2010, pp. 99–109.

[129] S Wang et al. “Influence of Al 3+ and P 5+ ion contents on the valence state of Yb 3+ ions and the dispersion effect of Al 3+ and P 5+ ions on Yb 3+ ions in silica glass”. In: *Journal of Materials Chemistry C* 2.22 (2014), pp. 4406–4414.

[130] K. Lyytikäinen et al. “Dopant diffusion during optical fibre drawing”. In: *Opt. Express* 12.6 (Mar. 2004), pp. 972–977. DOI: 10.1364/OPEX.12.000972. URL: https://opg.optica.org/oe/abstract.cfm?URI=oe-12-6-972.

[131] Sonja Unger et al. "Codoped materials for high power fiber lasers: diffusion behaviour and optical properties". In: *Optical Components and Materials IV*. Ed. by Shibin Jiang and Michel J. F. Digonnet. Vol. 6469. International Society for Optics and Photonics. SPIE, 2007, p. 646913. DOI: 10.1117/12.700161. URL: https://doi.org/10.1117/12.700161.

[132] Coherent. *YSF-HI-HP Product Datasheet*. https://coherentinc.my.site.com/Coherent/specialty-optical-fibers/PM-YSF-HI-HP, accessed 2024-08-21.

[133] Anka Schwuchow et al. "Advanced attenuation and fluorescence measurement methods in the investigation of photodarkening and related properties of ytterbium-doped fibers". In: *Appl. Optics* 53.7 (2014), p. 1466. ISSN: 1559-128X. DOI: 10.1364/ao.53.001466.

[134] R. Paschotta et al. "Efficient superfluorescent light sources with broad bandwidth". In: *IEEE Journal of Selected Topics in Quantum Electronics* 3.4 (1997), pp. 1097–1099. ISSN: 1077-260X. DOI: 10.1109/2944.649547.

[135] Brett E. Bouma. "Optical Coherence Tomographic Imaging of Human Tissue at 1.55 μm and 1.81 μm Using Er- and Tm-Doped Fiber Sources". In: *Journal of Biomedical Optics* 3.1 (1998), p. 76. ISSN: 1083-3668. DOI: 10.1117/1.429898.

[136] Zhihong Li et al. "Thulium-doped fiber amplifier for optical communications at 2 μm". In: *Optics Express* 21.8 (2013), pp. 9289–9297.

[137] Cristian Manzoni et al. "Coherent pulse synthesis: towards sub-cycle optical waveforms". In: *Laser & Photonics Reviews* 9.2 (2015), pp. 129–171.

[138] Yuta Kobayashi et al. "Effect of P-to-Rare Earth Atomic Ratio on Energy Transfer in Er-Yb-Doped Optical Fiber". In: *Journal of Lightwave Technology* 38.16 (2020), pp. 4504–4512. ISSN: 0733-8724. DOI: 10.1109/jlt.2020.2989774.

[139] Jonathan H.V. Price et al. "Supercontinuum generation in non-silica fibers". In: *Opt. Fiber Technol.* 18.5 (2012), pp. 327–344. ISSN: 1068-5200. DOI: 10.1016/j.yofte.2012.07.013. URL: http://www.sciencedirect.com/science/article/pii/S1068520012000843.

[140] Yu-xi Zhang and Yu-hua Wang. "Nonlinear optical properties of metal nanoparticles: a review". In: *RSC Advances* 7.71 (2017), pp. 45129–45144. ISSN: 2046-2069. DOI: 10.1039/c7ra07551k.

[141] Mansoor Sheik-Bahae et al. "Optical nonlinearities in diamond". In: *Proc. SPIE* 2428 (1995), pp. 605–609. ISSN: 0277-786X. DOI: 10.1117/12.213706.

[142] F. Trojánek et al. "Nonlinear optical properties of nanocrystalline diamond". In: *Optics Express* 18.2 (2010), p. 1349. ISSN: 1094-4087. DOI: 10.1364/oe.18.001349.

[143] Yinlan Ruan et al. "Tellurite microspheres for nanoparticle sensing and novel light sources". In: *Optics express* 22.10 (2014), pp. 11995–12006.

[144] Adam Filipkowski et al. "Volumetric incorporation of NV diamond emitters in nanostructured F2 glass magneto-optical fiber probes". In: *Carbon* 196 (2022), pp. 10–19.

[145] Alexander M. Heidt, Alexander Hartung, and Hartmut Bartelt. "The Supercontinuum Laser Source: The Ultimate White Light". In: New York, NY: Springer New York, 2016. Chap. Generation of Ultrashort and Coherent Supercontinuum Light Pulses in All-Normal Dispersion Fibers, pp. 247–280. ISBN: 978-1-4939-3326-6. DOI: 10.1007/978-1-4939-3326-6_6. URL: http://dx.doi.org/10.1007/978-1-4939-3326-6_6.

[146] Dirk Spangenberg et al. "Time-domain ptychography". In: *Phys. Rev. A* 91 (2 Feb. 2015), p. 021803. DOI: 10.1103/PhysRevA.91.021803. URL: http://link.aps.org/doi/10.1103/PhysRevA.91.021803.

[147] David Castelló-Lurbe et al. "Nonlinearity measurement undergoing dispersion and loss". In: *Opt. Lett.* 48.2 (Jan. 2023), pp. 493–496. DOI: 10.1364/OL.481445. URL: https://opg.optica.org/ol/abstract.cfm?URI=ol-48-2-493.

[148] Valerio Romano, Soenke Pilz, and Dereje Etissa. "Sol-gel-based doped granulated silica for the rapid production of optical fibers". In: *International Journal of Modern Physics B* 28.12 (2014), p. 1442010.

[149] Matthew R Majewski, Robert I Woodward, and Stuart D Jackson. "Dysprosium-doped ZBLAN fiber laser tunable from 2.8 μm to 3.4 μm, pumped at 1.7 μm". In: *Optics letters* 43.5 (2018), pp. 971–974.

[150] Junxiang Zhang et al. "Erbium-doped ZBLAN fiber laser pumped at 1.7 μm for emission at 2.8 μm". In: *Optics Letters* 47.15 (2022), pp. 3684–3687.

[151] Matthew R Majewski et al. "Emission beyond 4 μm and mid-infrared lasing in a dysprosium-doped indium fluoride (InF 3) fiber". In: *Optics letters* 43.8 (2018), pp. 1926–1929.

[152] Mario Christian Falconi et al. "Design of an Er3+: InF3 fiber laser pumped with red light". In: *Fiber Lasers and Glass Photonics: Materials through Applications III*. Vol. 12142. SPIE. 2022, pp. 233–237.

[153] P Dragic et al. "Sapphire-derived all-glass optical fibres". In: *Nature Photonics* 6.9 (2012), pp. 627–633.

[154] Kazuo Arai et al. "Aluminum or phosphorus coâ€doping effects on the fluorescence and structural properties of neodymiumâ€doped silica glass". In: *Journal of Applied Physics* 59.10 (May 1986), pp. 3430–3436. ISSN: 0021-8979. DOI: 10.1063/1.336810. eprint: https://pubs.aip.org/aip/jap/article-pdf/59/10/3430/18604634/3430_1_online.pdf. URL: https://doi.org/10.1063/1.336810.

[155] Robert A Blomquist, JK Fink, and Leonard Leibowitz. *Viscosity of molten alumina*. Argonne National Laboratory Lemont, IL, USA, 1978.

[156] F. Lindner et al. "Optical properties of Yb-doped fibers prepared by gas phase doping". In: *Optical Components and Materials XI*. Ed. by Michel J. F. Digonnet and Shibin Jiang. Vol. 8982. International Society for Optics and Photonics. SPIE, 2014, 89820R. DOI: 10.1117/12.2036928. URL: https://doi.org/10.1117/12.2036928.

[157] Peter D. Dragic et al. "YAG-derived fiber for high-power narrow-linewidth fiber lasers". In: *Fiber Lasers IX: Technology, Systems, and Applications*. Ed. by Eric C. Honea and Sami T. Hendow. Vol. 8237. International Society for Optics and Photonics. SPIE, 2012, 82371E. DOI: 10.1117/12.907478. URL: https://doi.org/10.1117/12.907478.

[158] Peter Dragic, Maxime Cavillon, and John Ballato. "The linear and nonlinear refractive index of amorphous Al2O3 deduced from aluminosilicate optical fibers". In: *International Journal of Applied Glass Science* 9.3 (2018), pp. 421–427.

[159] L.D. DeLoach et al. "Evaluation of absorption and emission properties of Yb/sup 3+/ doped crystals for laser applications". In: *IEEE Journal of Quantum Electronics* 29.4 (1993), pp. 1179–1191. DOI: 10.1109/3.214504.

[160] P. R. Berman. "Optical Faraday rotation". In: *American Journal of Physics* 78.3 (Mar. 2010), pp. 270–276. ISSN: 0002-9505. DOI: 10.1119/1.3266970. eprint: https://pubs.aip.org/aapt/ajp/article-pdf/78/3/270/13104609/270_1_online.pdf. URL: https://doi.org/10.1119/1.3266970.

[161] Yan Li et al. "Measurement system of the fibers' verdet constant including a Faraday rotator mirror". In: *2013 Third International Conference on Instrumentation, Measurement, Computer, Communication and Control*. IEEE. 2013, pp. 53–56.

[162] Klaus Bohnert et al. "Highly accurate fiber-optic DC current sensor for the electrowinning industry". In: *IEEE Transactions on industry applications* 43.1 (2007), pp. 180–187.

[163] John Minelly and Adam Ellison. "Applications of antimony–silicate glasses for fiber optic amplifiers". In: *Optical Fiber Technology* 8.2 (2002), pp. 123–138.

[164] *UT-CS09D Flex Clamp Sensor*. https://meters.uni-trend.com/product/ut-cs09d/. Accessed: 2024-08-04. UNI-TREND TECHNOLOGY (CHINA) CO., LTD., 2024.

[165] Thorlabs. *SM400 Single Mode Fiber*. Accessed: 2024-08-02. 2023. URL: https://www.thorlabs.com/newgrouppage9.cfm?objectgroup_id=949&pn=SM400.

[166] Fiber Optics For Sale. *Faraday Effect*. Accessed: 2024-08-02. 2023. URL: https://www.fiberoptics4sale.com/blogs/wave-optics/faraday-effect.

[167] Moh Yasin, Sulaiman Wadi Harun, and Hamzah Arof. "Recent progress in optical fiber research". In: *Recent Progress in Optical Fiber Research*. BoD–Books on Demand, 2012. Chap. 7, p. 132.

[168] Richard I Laming and David N Payne. "Electric current sensors employing spun highly birefringent optical fibers". In: *Journal of Lightwave Technology* 7.12 (1989), pp. 2084–2094.

[169] Penghui Yao et al. "Introduction and measurement of the effective Verdet constant of spun optical fibers". In: *Optics Express* 29.15 (2021), pp. 23315–23330.

[170] Christian Pflitsch et al. "Sol–gel deposition of chromium doped aluminium oxide films (ruby) for surface temperature sensor application". In: *Chemistry of Materials* 20.8 (2008), pp. 2773–2778.

[171] Dominik Wildanger et al. “STED microscopy with a supercontinuum laser source”. In: *Optics express* 16.13 (2008), pp. 9614–9621.

[172] Manoj K. Dasa et al. “All-fibre supercontinuum laser for in vivo multispectral photoacoustic microscopy of lipids in the extended near-infrared region”. In: *Photoacoustics* 18 (2020), p. 100163. ISSN: 2213-5979. DOI: https://doi.org/10.1016/j.pacs.2020.100163. URL: https://www.sciencedirect.com/science/article/pii/S2213597920300033.

[173] Sucbei Moon and Dug Young Kim. “Ultra-high-speed optical coherence tomography with a stretched pulse supercontinuum source”. In: *Opt. Express* 14.24 (2006), pp. 11575–11584.

[174] Christopher J Ostaszewski et al. “Effects of coadsorbed water on the heterogeneous photochemistry of nitrates adsorbed on TiO_2”. In: *The Journal of Physical Chemistry A* 122.31 (2018), pp. 6360–6371.

[175] Krupa Ramasesha et al. “Water vibrations have strongly mixed intra-and intermolecular character”. In: *Nature Chemistry* 5.11 (2013), pp. 935–940.

[176] John M. Dudley, Go?ry Genty, and St?phane Coen. “Supercontinuum generation in photonic crystal fiber”. In: *Rev. Mod. Phys.* 78.4 (2006), pp. 1135–1184.

[177] K. L. Corwin et al. “Fundamental Noise Limitations to Supercontinuum Generation in Microstructure Fiber”. In: *Phys. Rev. Lett.* 90.11 (Mar. 2003), p. 113904. DOI: 10.1103/PhysRevLett.90.113904.

[178] U Møller and Ole Bang. “Intensity noise in normal-pumped picosecond supercontinuum generation, where higher-order Raman lines cross into anomalous dispersion regime”. In: *Electron. Lett.* 49.1 (2013), pp. 63–65.

[179] Stefan Wabnitz. “Modulational polarization instability of light in a nonlinear birefringent dispersive medium”. In: *Phys Rev A* 38.4 (1988), p. 2018.

[180] Iván Bravo Gonzalo et al. “Polarization noise places severe constraints on coherence of all-normal dispersion femtosecond supercontinuum generation”. In: *Sci. Rep.* 8.1 (2018), p. 6579.

[181] Chia-Ming Chen and Paul L. Kelley. “Nonlinear pulse compression in optical fibers: scaling laws and numerical analysis”. In: *J. Opt. Soc. Am. B* 19.9 (Sept. 2002), pp. 1961–1967. DOI: 10.1364/JOSAB.19.001961. URL: http://josab.osa.org/abstract.cfm?URI=josab-19-9-1961.

[182] Pedram Abdolghader et al. “All normal dispersion nonlinear fibre supercontinuum source characterization and application in hyperspectral stimulated Raman scattering microscopy”. In: *Opt. Express* 28.24 (2020), pp. 35997–36008.

[183] Korbinian J. Kaltenecker et al. “Near-infrared nanospectroscopy using a low-noise supercontinuum source”. In: *APL Photonics* 6.6 (2021), p. 066106. ISSN: 2378-0967. DOI: 10.1063/5.0050446.

[184] Shreesha Rao D.S. et al. “Shot-noise limited, supercontinuum-based optical coherence tomography”. In: *Light: Science & Applications* 10.1 (2021), p. 133. DOI: 10.1038/s41377-021-00574-x. eprint: 2010.05226 (physics.optics).

[185] Haohua Tu et al. "Stain-free histopathology by programmable supercontinuum pulses". In: *Nat. Photonics* 10.8 (2016), p. 534. DOI: https://doi.org/10.1038/nphoton.2016.94.

[186] Krzysztof P Herdzik et al. "Multimodal spectral focusing CARS and SFG microscopy with a tailored coherent continuum from a microstructured fiber". In: *Appl. Phys. B* 126 (2020), p. 84.

[187] Alexander M Heidt et al. "Low noise all-fiber amplification of a coherent supercontinuum at 2 μm and its limits imposed by polarization noise". In: *Sci. Rep.* 10.1 (2020), p. 16734.

[188] Anupamaa Rampur et al. "Temporal fine structure of all-normal dispersion fiber supercontinuum pulses caused by non-ideal pump pulse shapes". In: *Opt. Express* 28.11 (2020), pp. 16579–16593.

[189] Anupamaa Rampur et al. "Ultra low-noise coherent supercontinuum amplification and compression below 100 fs in an all-fiber polarization-maintaining thulium fiber amplifier". In: *Opt. Express* 27.24 (2019), pp. 35041–35051.

[190] Goëry Genty, Stéphane Coen, and John M. Dudley. "Fiber supercontinuum sources (Invited)". In: *J. Opt. Soc. Am. B* 24.8 (2007), pp. 1771–1785. URL: http://josab.osa.org/abstract.cfm?URI=josab-24-8-1771.

[191] Takashi Hori et al. "Flatly broadened, wideband and low noise supercontinuum generation in highly nonlinear hybrid fiber". In: *Opt. Express* 12.2 (Jan. 2004), pp. 317–324. DOI: 10.1364/OPEX.12.000317. URL: http://www.opticsexpress.org/abstract.cfm?URI=oe-12-2-317.

[192] N. Bloembergen and Y. R. Shen. "Coupling Between Vibrations and Light Waves in Raman Laser Media". In: *Phys. Rev. Lett.* 12 (18 May 1964), pp. 504–507. DOI: 10.1103/PhysRevLett.12.504. URL: https://link.aps.org/doi/10.1103/PhysRevLett.12.504.

[193] Mariusz Klimczak et al. "Coherent supercontinuum generation in soft glass photonic crystal fibers". In: *Photonics Res.* 5.6 (2017), pp. 710–727.

[194] Christophe Finot et al. "Beneficial impact of wave-breaking for coherent continuum formation in normally dispersive nonlinear fibers". In: *J. Opt. Soc. Am. B* 25.11 (2008), pp. 1938–1948. URL: http://josab.osa.org/abstract.cfm?URI=josab-25-11-1938.

[195] Stéphane Coen et al. "Supercontinuum generation by stimulated Raman scattering and parametric four-wave mixing in photonic crystal fibers". In: *JOSA B* 19.4 (2002), pp. 753–764.

[196] Karol Tarnowski et al. "Polarized all-normal dispersion supercontinuum reaching 2.5 μm generated in a birefringent microstructured silica fiber". In: *Opt Express* 25.22 (2017), pp. 27452–27463.

[197] Alexander Hartung et al. "Design and fabrication of all-normal dispersion nanohole suspended-core fibers". In: *J. Opt. Soc. Am. B* 36.12 (2019), pp. 3404–3410.

[198] Yuan Liu et al. "Suppressing short-term polarization noise and related spectral decoherence in all-normal dispersion fiber supercontinuum generation". In: *J. Lightwave Technol.* 33.9 (2015), pp. 1814–1820.

[199] Govind P. Agrawal, P. L. Baldeck, and R. R. Alfano. "Modulation instability induced by cross-phase modulation in optical fibers". In: *Phys. Rev. A* 39 (7 Apr. 1989), pp. 3406–3413. DOI: 10.1103/PhysRevA.39.3406. URL: https://link.aps.org/doi/10.1103/PhysRevA.39.3406.

[200] Etienne Genier et al. "Cross-phase modulation instability in PM ANDi fiber-based supercontinuum generation". In: *Opt. Lett.* 45.13 (July 2020), pp. 3545–3548. DOI: 10.1364/OL.397106. URL: http://ol.osa.org/abstract.cfm?URI=ol-45-13-3545.

[201] James S. Feehan and Jonathan H. V. Price. "Decoherence due to XPM-assisted Raman amplification for polarization or wavelength offset pulses in all-normal dispersion supercontinuum generation". In: *J. Opt. Soc. Am. B* 37.3 (Mar. 2020), pp. 635–644. DOI: 10.1364/JOSAB.379563. URL: http://josab.osa.org/abstract.cfm?URI=josab-37-3-635.

[202] James S. Feehan et al. "Noise-related polarization dynamics for femto and picosecond pulses in normal dispersion fibers". In: *Opt. Express* 28.15 (July 2020), pp. 21447–21463. DOI: 10.1364/OE.396404. URL: http://www.opticsexpress.org/abstract.cfm?URI=oe-28-15-21447.

[203] Florian Adler and Scott A Diddams. "High-power, hybrid Er:fiber/Tm:fiber frequency comb source in the 2 μm wavelength region". In: *Opt Lett* 37.9 (2012), pp. 1400–1402.

[204] Norihiko Nishizawa et al. "Octave Spanning Coherent Supercontinuum Comb Generation Based on Er-Doped Fiber Lasers and Their Characterization". In: *IEEE Journal of Selected Topics in Quantum Electronics* 24.3 (2018), pp. 1–9.

[205] Daniel MB Lesko et al. "A six-octave optical frequency comb from a scalable few-cycle erbium fibre laser". In: *Nat. Photonics* 15 (2021), pp. 281–286.

[206] Nan Zhang et al. "Ultrabroadband and coherent mid-infrared supercontinuum generation in Te-based chalcogenide tapered fiber with all-normal dispersion". In: *Opt Express* 27.7 (2019), pp. 10311–10319.

[207] Rafal P Sopalla et al. "Generation of broadband circularly polarized supercontinuum light in twisted photonic crystal fibers". In: *Opt Lett* 44.16 (2019), pp. 3964–3967.

[208] H Hoogland et al. "All-PM coherent 2.05 μm Thulium/Holmium fiber frequency comb source at 100 MHz with up to 0.5 W average power and pulse duration down to 135 fs". In: *Opt Express* 21.25 (2013), pp. 31390–31394.

[209] C. Gaida et al. "High-power frequency comb at 2μm wavelength emitted by a Tm-doped fiber laser system". In: *Opt. Lett.* 43.21 (Nov. 2018), pp. 5178–5181. DOI: 10.1364/OL.43.005178. URL: http://ol.osa.org/abstract.cfm?URI=ol-43-21-5178.

[210] Masataka Nakazawa et al. "Coherence Degradation in the Process of Supercontinuum Generation in an Optical Fiber". In: *Optical Fiber Technology* 4.2 (1998), pp. 215–223. ISSN: 1068-5200. DOI: https://doi.org/10.1006/ofte.1998.0253. URL: https://www.sciencedirect.com/science/article/pii/S106852009890253X.

[211] Piotr Ciąćka et al. "Dispersion measurement of ultra-high numerical aperture fibers covering thulium, holmium, and erbium emission wavelengths". In: *J. Opt. Soc. Am. B* 35.6 (June 2018), pp. 1301–1307. DOI: 10.1364/JOSAB.35.001301. URL: http://josab.osa.org/abstract.cfm?URI=josab-35-6-1301.

[212] Stefan Preble. *Nufern Application Note NuApp-3: UHNA Fiber – Efficient Coupling to Silicon Waveguides*. 2016. URL: https://www.coherent.com/content/dam/coherent/site/en/resources/application-note/components-and-accessories/specialty-optical-fibers/uhna-fiber-efficient-coupling-to-silicon-waveguides.pdf.

[213] Alexander M Heidt et al. "Improved retrieval of complex supercontinuum pulses from XFROG traces using a ptychographic algorithm". In: *Opt Lett* 41.21 (2016), pp. 4903–4906.

[214] Ryan P Scott, Carsten Langrock, and Brian H Kolner. "High-dynamic-range laser amplitude and phase noise measurement techniques". In: *IEEE J. Sel. Top. Quantum Electron.* 7.4 (2001), pp. 641–655.

[215] Jungwon Kim and Youjian Song. "Ultralow-noise mode-locked fiber lasers and frequency combs: principles, status, and applications". In: *Advances in Optics and Photonics* 8.3 (Aug. 2016), p. 465. DOI: 10.1364/aop.8.000465.

[216] A. A. Rieznik et al. "Optimum Integration Procedures for Supercontinuum Simulation". In: *IEEE Photonics J.* 4.2 (Apr. 2012), pp. 552–560. ISSN: 1943-0655. DOI: 10.1109/JPHOT.2012.2188281.

[217] Q. Lin and Govind P. Agrawal. "Raman response function for silica fibers". In: *Opt. Lett.* 31.21 (2006), pp. 3086–3088. URL: http://ol.osa.org/abstract.cfm?URI=ol-31-21-3086.

[218] Jesper Laegsgaard. "Mode profile dispersion in the generalised nonlinear Schrödinger equation". In: *Opt. Express* 15.24 (2007), pp. 16110–16123. URL: http://www.opticsexpress.org/abstract.cfm?URI=oe-15-24-16110.

[219] D Marcuse. "Gaussian approximation of the fundamental modes of graded-index fibers". In: *JOSA* 68.1 (1978), pp. 103–109.

[220] Andrew Klose et al. "Tunable, stable source of femtosecond pulses near 2 m via supercontinuum of an Erbium mode-locked laser". In: *Optics Express* 22.23 (Nov. 2014), p. 28400. DOI: 10.1364/oe.22.028400.

[221] Mariusz Klimczak et al. "Direct comparison of shot-to-shot noise performance of all normal dispersion and anomalous dispersion supercontinuum pumped with sub-picosecond pulse fiber-based laser". In: *Sci. Rep.* 6.1 (2016), p. 19284.

[222] Benoıt Sierro and Alexander M Heidt. "Noise amplification in all-normal dispersion fiber supercontinuum generation and its impact on ultrafast photonics applications". In: *OSA Continuum* 3.9 (2020), pp. 2347–2361.

[223] R. G. Smith. "Optical Power Handling Capacity of Low Loss Optical Fibers as Determined by Stimulated Raman and Brillouin Scattering". In: *Appl. Opt.* 11.11 (Nov. 1972), pp. 2489–2494. DOI: 10.1364/AO.11.002489. URL: http://ao.osa.org/abstract.cfm?URI=ao-11-11-2489.

[224] Etienne Genier et al. "An ultra-flat, low-noise and linearly polarized fiber supercontinuum source covering 670 nm-1390 nm". In: *Opt. Lett.* 46.8 (2021), pp. 1820–1823.

[225] Bojan Resan et al. "1% rms amplitude noise from a 30 fs continuum based source tunable from 800 to 1250 nm". In: *Opt. Express* 24.13 (June 2016), p. 14960. DOI: 10.1364/oe.24.014960.

[226] Shreesha Rao D.S. et al. "Ultra-low-noise supercontinuum generation with a flat near-zero normal dispersion fiber". In: *Opt. Lett.* 44.9 (2019), pp. 2216–2219.

[227] Francesco Poletti and Peter Horak. "Description of ultrashort pulse propagation in multimode optical fibers". In: *J. Opt. Soc. Am. B* 25.10 (Oct. 2008), pp. 1645–1654. DOI: 10.1364/JOSAB.25.001645. URL: http://josab.osa.org/abstract.cfm?URI=josab-25-10-1645.

[228] J. W. Nicholson and M. F. Yan. "Cross-coherence measurements of supercontinua generated in highly-nonlinear, dispersion shifted fiber at 1550 nm". In: *Opt. Express* 12.4 (2004), p. 679. DOI: 10.1364/opex.12.000679.

[229] Xun Gu et al. "Experimental studies of the coherence of microstructure-fiber supercontinuum". In: *Opt. Express* 11.21 (2003), pp. 2697–2703. URL: http://www.opticsexpress.org/abstract.cfm?URI=oe-11-21-2697.

[230] D. Türke et al. "Coherence of subsequent supercontinuum pulses generated in tapered fibers in the femtosecond regime". In: *Opt. Express* 15.5 (2007), p. 2732. DOI: 10.1364/oe.15.002732.

[231] Norihiko Nishizawa and Jun Takayanagi. "Octave spanning high-quality supercontinuum generation in all-fiber system". In: *J. Opt. Soc. Am. B* 24.8 (2007), pp. 1786–1792. URL: http://josab.osa.org/abstract.cfm?URI=josab-24-8-1786.

[232] Neetesh Singh et al. "Octave-spanning coherent supercontinuum generation in silicon on insulator from 1.06μm to beyond 2.4μm". In: *Light Sci. Appl.* 7.1 (2018), pp. 17131–17131. DOI: 10.1038/lsa.2017.131.

[233] Anndrea R. Johnson et al. "Octave-spanning coherent supercontinuum generation in a silicon nitride waveguide". In: *Opt. Lett.* 40.21 (Oct. 2015), p. 5117. DOI: 10.1364/ol.40.005117.

[234] Mikko Närhi et al. "Experimental Measurement of the Second-Order Coherence of Supercontinuum". In: *Phys. Rev. Lett.* 116.24 (2016), p. 243901. DOI: 10.1103/physrevlett.116.243901.

[235] Karol Tarnowski et al. "Compact all-fiber source of coherent linearly polarized octave-spanning supercontinuum based on normal dispersion silica fiber". In: *Sci Rep* 9.1 (2019), p. 12313.

[236] J. W. Nicholson et al. "Coherence of supercontinua generated by ultrashort pulses compressed in optical fibers". In: *Opt. Lett.* 33.18 (2008), pp. 2038–2040. URL: http://ol.osa.org/abstract.cfm?URI=ol-33-18-2038.

[237] Dirk-Mathys Spangenberg et al. "Noise Fingerprints of Fiber Supercontinuum Sources". In: *2021 Conference on Lasers and Electro-Optics Europe and European Quantum Electronics Conference*. Optica Publishing Group, 2021, cd_5_3. URL: https://opg.optica.org/abstract.cfm?URI=CLEO_Europe-2021-cd_5_3.

[238] Daniele Brida et al. "Ultrabroadband Er: fiber lasers". In: *Laser & Photonics Reviews* 8.3 (2014), pp. 409–428.

[239] Alexander M. Heidt et al. "Coherent octave spanning near-infrared and visible supercontinuum generation in all-normal dispersion photonic crystal fibers". In: *Opt. Express* 19.4 (Feb. 2011), pp. 3775–3787. DOI: 10.1364/OE.19.003775. URL: http://www.opticsexpress.org/abstract.cfm?URI=oe-19-4-3775.

[240] Alexander M. Heidt et al. "The Supercontinuum Laser Source". In: Springer, 2022. Chap. All-Normal Dispersion Fiber Supercontinuum: Principles, Design, and Applications of a Unique White Light Source, pp. 299–341.

Acknowledgements

Most importantly, I want to thank my two supervisors, Alex and Valerio, for creating this unique PhD position that I have held for the last four years. The position was shared between the IAP, focused on pure research, and the BFH, where the work is more oriented towards industry. I had the opportunity to work on a wide variety of vastly different and interesting projects, a diversity I greatly appreciated. My supervisors were always supportive, even from halfway around the globe or during the pandemic.
I had the privilege of working with many great people throughout my PhD journey. Sönke was instrumental in showing me the ins and outs of fiber drawing. Benoît, my office mate, was truly a nice and helpful person. It was a pleasure to work alongside him every day.
Anupamaa, Dunia, Dirk and Yves were wonderful coworkers, and I enjoyed every moment spent working with them in the lab. Not to forget our guest researcher, Shreesha, with whom I had many interesting discussions.

A key part of every day is lunch, which I am grateful to have often shared with Hansi, Elnaz, and Vivek. These moments were a welcome break in the daily routine, as were the coffee breaks with Dominic, filled with discussions about optics and life.
I would also like to extend my gratitude to the electronic workshop team and the secretary. Their support was invaluable in handling electronic challenges and bureaucratic necessities.
Special thanks also go to Warsaw. Without Mariusz Klimczak and all the people involved in the fiber drawing operation there, my fibers would have been drawn only two years later, as we were struggling to accommodate my preforms in our own drawing tower. They also introduced me to the very promising and exciting field of nanodiamond doping of fibers.
I was also incredibly happy to share my last year at IAP with my long-time friend Philipp, who started his PhD a year ago in the microwave group and with whom I already shared military service, bachelor studies, and many adventures in the mountains. May you stay free of injury.
The key people who enabled me to pursue such a challenging, intensive, and interesting education in the first place are my parents. They never put any pressure on me to achieve anything but supported every step in my life.
Finally, I want to thank my partner, Sereina, who has been with me every step of the way. Her support and understanding have been invaluable, especially as she begins her own PhD journey. I hope to repay her support, encouragement, and patience as we embark on this new chapter in life together.

Erklärung

gemäss Art. 18 PromR Phil.-nat. 2019

Name/Vorname: Hänzi Pascal Manuel

Matrikelnummer: 14-126-023

Studiengang: Physik

Bachelor ☐ Master ☐ Dissertation ☑

Titel der Arbeit: Laser-assisted Fabrication of Specialty Optical Fibers and Applications in Nonlinear Optics, Light Amplification, and Sensing

LeiterIn der Arbeit: Prof. Dr. Alexander Heidt

Ich erkläre hiermit, dass ich diese Arbeit selbständig verfasst und keine anderen als die angegebenen Quellen benutzt habe. Alle Stellen, die wörtlich oder sinngemäss aus Quellen entnommen wurden, habe ich als solche gekennzeichnet. Mir ist bekannt, dass andernfalls der Senat gemäss Artikel 36 Absatz 1 Buchstabe r des Gesetzes über die Universität vom 5. September 1996 und Artikel 69 des Universitätsstatuts vom 7. Juni 2011 zum Entzug des Doktortitels berechtigt ist. Für die Zwecke der Begutachtung und der Überprüfung der Einhaltung der Selbständigkeitserklärung bzw. der Reglemente betreffend Plagiate erteile ich der Universität Bern das Recht, die dazu erforderlichen Personendaten zu bearbeiten und Nutzungshandlungen vorzunehmen, insbesondere die Doktorarbeit zu vervielfältigen und dauerhaft in einer Datenbank zu speichern sowie diese zur Überprüfung von Arbeiten Dritter zu verwenden oder hierzu zur Verfügung zu stellen.

Ort/Datum

Unterschrift